A Measurement of Strange Baryon Production and Correlations in Hadronic Z^0 Decays

by

James Robert Letts

A Dissertation submitted in partial satisfaction
of the requirements for the degree of

DOCTOR OF PHILOSOPHY
IN
PHYSICS

UNIVERSITY OF CALIFORNIA, RIVERSIDE
DECEMBER 1993

UNIVERSITY OF CALIFORNIA
RIVERSIDE

A Measurement of Strange Baryon Production and Correlations in Hadronic Z^0 Decays

A Dissertation submitted in partial satisfaction
of the requirements for the degree of

Doctor of Philosophy

in

Physics

by

James Robert Letts

December 1993

Dissertation Committee:

Professor Benjamin C. Shen, Chairperson

Professor John G. Layter

Professor J. William Gary

Acknowledgements

Working on the OPAL experiment at CERN has been an enjoyable and rewarding experience. My thanks go to the many people who were responsible for building and operating the OPAL detector and the LEP machine.

I would especially like to thank my advisor Dr. Benjamin C. Shen for providing the opportunity for me to work on the OPAL experiment. During my years at CERN, I worked most closely with Dr. Michael Dittmar. His guidance and enthusiasm for research were very helpful to me. From Dr. William Gorn, I learned the hardware aspects of experimental physics.

Many thanks must also go to the other physicists from Riverside who have helped me along the way, including Dr. Gordon J. Van Dalen, Dr. John G. Layter, Dr. J. William Gary, and Dr. Charles C.H. Jui. I would also like to acknowledge the help of my fellow graduate students, Dr. William J. Larson, Dr. Brendan O'Neill, Dr. Heungmin Oh, who helped me especially in my first year at CERN, and also Shun-Lung Chu. I also would like to thank my family and close friends for their support during these past years.

This work was supported by the United States Department of Energy.

ABSTRACT OF THE DISSERTATION

A Measurement of Strange Baryon Production and Correlations in Hadronic Z^0 Decays

by

James Robert Letts

Doctor of Philosophy, Graduate Program in Physics

University of California, Riverside, December 1993

Professor Benjamin C. Shen, Chairperson

Strange baryon production in hadronic Z^0 decays is studied using 1.24 million multihadron events collected with the OPAL detector at LEP. Accurate measurements of the production rates of Λ, Ξ^-, $\Sigma(1385)^{\pm}$, $\Xi(1530)^0$, and Ω^- are described and the correlations between baryon pairs from the same event are investigated. From these studies, it is concluded that diquark fragmentation models can describe only some of the features of baryon production. Important failures of the models include the descriptions of the fragmentation function, the rates of spin 3/2 baryons, and the rates of baryon pair production. A study of rapidity correlations of baryon pairs shows the general features predicted by chain-like models of baryon production. The rapidity correlations can be described with the JETSET Monte Carlo with a dominant production chain of baryon-meson-antibaryon.

Contents

List of Figures

List of Tables

Chapter 1

Introduction

The Standard Model [1] has been very successful in describing the electromagnetic and weak interactions of quarks and leptons, which are thought to be the fundamental fermions (spin 1/2 particles). This single unified theory describes the electroweak interactions. In addition, there is a theory of the strong interactions of quarks and gluons, called Quantum Chromodynamics, or QCD [2].

QCD is very successful at describing high-q^2 processes, such as the radiation of gluons by quarks. At high-q^2 the QCD coupling constant is small and perturbative calculations are possible. However, at low momentum transfers, the coupling constant becomes large and perturbative expansions in α_S do not converge. Theoretical predictions at low-q^2 essentially do not exist.

The quarks themselves are not observable as free particles, but are confined in hadronic final states, either mesons ($q\overline{q}$ states) or baryons (qqq states). The hadronization of quarks is thought to take place at relatively low q^2, an assumption which is based on the experimental observation from e^+e^- collisions that final state hadrons are seen in relatively narrow jets [3]. QCD is assumed to be the theory which underlies jet hadronization.

The current understanding of jet hadronization does not extend beyond some very general ideas. Some common assumptions are that baryons and mesons are produced in a similar way and that quantum numbers are conserved in a chain-like manner. For meson production one can imagine that quark-antiquark pairs are produced from the sea. The significant number of baryons produced in e^+e^- collisions at lower center-of-mass energies was more difficult to explain. To produce a baryon, one must make three quarks, and for an antibaryon, three antiquarks.

Progress was made in understanding baryon production at previous experiments at PETRA and PEP, and at CLEO and ARGUS, where measurements of the cross sections of different baryons and mesons and of correlations between baryon-antibaryon pairs were performed [4, 5, 6]. The observed ratio of $K^\pm/\pi^\pm \approx 0.15$ showed that there is suppression of strange quark production from the sea. However, measurements such as the ratio of $\Xi^-/\Lambda \approx 0.08$ indicated that there may be extra suppression for strange quarks within baryons.

Despite the progress which has been made, there are still many open questions about jet hadronization:

- How do quarks (and gluons) transform themselves into observable hadrons?

- How are baryons formed?
- What determines their flavor and spin?
- How are quantum numbers (such as baryon number, strangeness, etc.) conserved?
- How are the quantum numbers of the original $q\bar{q}$ pair expressed in the properties of jets and final state hadrons?

With the larger statistics available at $\sqrt{s} = m_{\mathrm{Z}^0}$, one can try to answer some of these questions in more detail. By measuring the cross sections of many strange baryons of different spin, isospin, and strangeness, one can provide experimental input to model builders.

Chain-like models of baryon production predict that baryon-antibaryon pairs will be strongly correlated in rapidity[1]. If quantum numbers such as baryon number and strangeness are conserved locally, one would expect to see that baryon-antibaryon pairs are also strongly correlated in rapidity.

In addition to short-range correlations within a jet, long-range correlations are expected if high momentum baryons contain the primary quarks of the Z^0 decay, or are decay daughters of particles which contained the primary quarks. If this assumption is correct, then baryons will present an interesting way to investigate not only the process of jet hadronization, but can also act as probes of the primary quarks themselves.

---

[1] The rapidity of a particle relative to a particular axis is defined as $y = \frac{1}{2}\log\left(\frac{E+p_{\parallel}}{E-p_{\parallel}}\right)$.

In the following chapter, a general overview of the Standard Model is presented, followed by a summary of what is currently known about jet hadronization. In the third chapter, the experimental apparatus is described. The measurements themselves are presented in the following chapters: inclusive strange baryon production in chapter four, correlations between baryon-antibaryon pairs in chapter five, and finally in chapter six, a measurement of the forward-backward asymmetry of $\Lambda(\overline{\Lambda})$.

The measurements are based on experimental data collected from 1990 to 1992 with the OPAL experiment at LEP. The measurements of inclusive strange baryon production and correlations of strange baryon pairs have been the subject of two recent OPAL papers [7, 8], which were based on the 1990 and 1991 data samples. There has also been a publication from the DELPHI Collaboration on inclusive strange particle production [9]. This thesis includes the analysis of the 1992 OPAL data to improve and expand upon the results of the published OPAL papers.

Chapter 2

The Standard Model and Models of Hadronization

2.1 The Standard Model

The fundamental fermions (spin 1/2 particles) are thought to be quarks and leptons. Quarks are organized into weak-isospin SU(2) doublets as follows:

$$\begin{pmatrix} u \\ d \end{pmatrix}_L \begin{pmatrix} c \\ s \end{pmatrix}_L \begin{pmatrix} t \\ b \end{pmatrix}_L .$$

The up-type quarks have a charge of $+\frac{2}{3}$, and the down-type quarks have a charge of $-\frac{1}{3}$. The leptons are similarly organized into doublets,

$$\begin{pmatrix} e^- \\ \nu_e \end{pmatrix}_L \begin{pmatrix} \mu^- \\ \nu_\mu \end{pmatrix}_L \begin{pmatrix} \tau^- \\ \nu_\tau \end{pmatrix}_L .$$

The right handed components are organized into singlets, except for the ν_R, which do not exist in the Standard Model. All have been directly observed except for the top quark and the tau neutrino. The top quark has been the subject of intensive searches at colliders in recent years. The most recently published lower limit on the top mass from the CDF collaboration is at present 91 GeV, assuming that only standard decays are allowed [10].

In total there are three known families of fermions, the main difference being that each sucessive family has a higher mass. Although only three families have been observed so far, the existence of still heavier familes is not ruled out by the Standard Model. The combined measurements of the number of light neutrinos from the four LEP experiments at $\sqrt{s} = m_{Z^0}$ of $N_\nu = 3.00 \pm 0.05$ gives the best limit on the number of light generations [11].

In addition to the fermions, there are several types of bosons (integer spin particles) which mediate interactions in the Standard Model. The electroweak interactions are mediated by the heavy $W^\pm$ and Z^0, and the massless photon. The two weak bosons, $W^\pm$ and Z^0, were first observed at CERN in 1983 [12]. The fermions couple to the different bosons with a strength dependant on the coupling constant, which in general depends on the momentum transfer between the fermions, q^2. In this way the fermions can interact with one another through the gauge bosons. The Standard Model allows several different types of interactions. All charged particles couple to the photon and can interact electromagnetically. All fermions couple to the $W^\pm$ and the Z^0 and can undergo weak interactions. The Standard Model combines the electromagnetic and weak interactions in a single Lagrangian, giving the electroweak interactions a unified structure.

Since explicit mass terms in the Lagrangian of the Standard Model would not be locally gauge invariant, it is necessary to introduce fermion masses via a method called spontaneous symmetry breaking. In the minimal Standard Model, this can be achieved by the introduction of a doublet of Higgs bosons, one of which has a non-zero vacuum expectation value and can couple to the fermions with a strength proportional to the fermion mass. The Higgs boson has not been discovered yet. A mass limit of $m_{H^0} >$58.4 GeV [13] at the 95% confidence level has been obtained at LEP for the Standard Model Higgs boson.

The quarks and gluons are the only particles which have been found to be affected by the strong force of QCD. The quarks carry a quantum number called color (red, green, or blue) so that each quark is in a color triplet state. The strong force is mediated by gauge bosons, called gluons. The gluons also carry the color quantum number, each gluon having one color and one anti-color. There are eight gluons in all, corresponding to the eight possible generators of SU(3). Evidence for the existence of the gluon was first seen in 1979 at PETRA [14].

Although there is convincing experimental evidence for the existence of quarks and gluons, all free particles which are observed in nature have been color singlets. In other words, the quarks seem to be confined in hadrons and can not themselves exist as free states. This confinement is thought to be a consequence of the q^2 dependence of the QCD coupling constant. Experimentally α_S has been found to decrease with q^2. The running of the coupling constant means that as quarks are pulled away from each other to large distances (or equivalently low q^2), they interact more strongly, in a similar way that a spring will exert more force as it is stretched. For this reason, quarks will couple strongly to one another and will always be bound in colorless states. Since there are three colors, the two simplest colorless states which can be made are $q\overline{q}$, which are called mesons, and qqq, which are called baryons.

At e^+e^- colliders like LEP, circulating beams of electrons and positrons are made to collide to form Z^0 bosons. This is an entirely electroweak process. The Z^0 decays into a number of known final states: e^+e^-, $\mu^+\mu^-$, $\tau^+\tau^-$, $\nu\overline{\nu}$, or $q\overline{q}$. Almost 70% of Z^0 decays are into the $q\overline{q}$ final state [15]. The transition of the quarks into hadronic final states is not understood and is the subject of this thesis. A graphical representation of the process $Z^0 \to q\bar{q}$ and the subsequent fragmentation into observable hadrons is shown in figure 2.1.

2.2 Baryons and the Quark Model

The SU(3) color symmetry of QCD was suggested by observed regularities in the baryon spectrum in the 1960's. The baryons were organized into multiplets of the same spin and parity, as shown in figures 2.2 and 2.3. It was noticed that the members of the same isospin multiplets had very similar masses. For example, the Σ^0 has a mass of 1192.5 MeV, Σ^- a mass of 1197.4 MeV and Σ^+ a mass of 1189.4 MeV [15], which are all within a range of ±8 MeV. Baryons with the same strangeness but different isospin were observed to have similar masses. With each increment in strangeness, the masses of the baryons increased by roughly 150 MeV. Although the reason behind this approximate symmetry was not known at the time, it was on

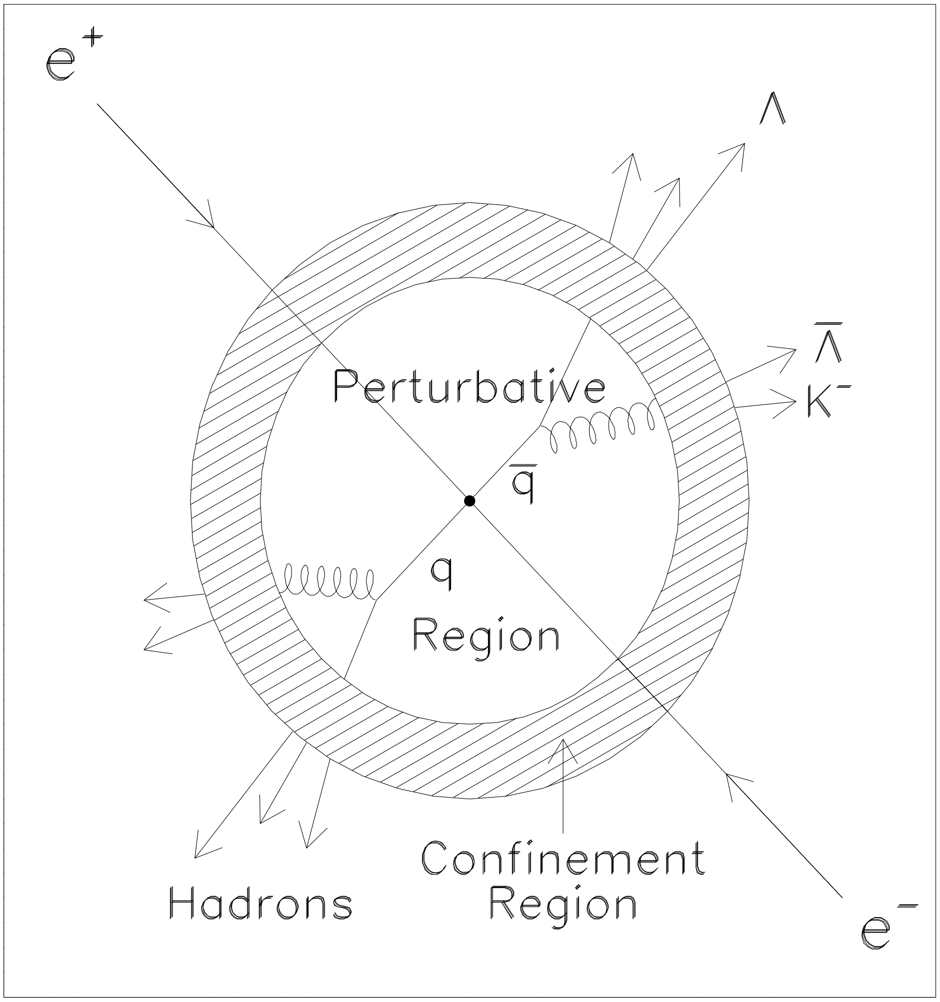

Figure 2.1: A diagram showing the various stages of jet fragmentation and hadronization. First is the perturbative region, in which QCD calculations are possible. Then follows the stage at which quarks are confined in the observable final state hadrons, which are finally observed in jets.

this basis that the Ω^- baryon was predicted [16] and later discovered [17].

The hypothesis that the underlying symmetry was due to the quark content of the baryons was first made in 1964 by Gell-Mann [18] and Zweig [19]. The observed regularities in the baryon spectrum can be accounted for by proposing that each baryon is made up of three quarks. Quarks, being fermions, must obey the Pauli exclusion principle, which states that no two fermions may occupy the same quantum state. The existence of spin 3/2 baryons such as Δ^- (ddd), Δ^{++} (uuu), and Ω^- (sss) would violate this principle if there were not an internal degree of freedom, since all three quarks would have their spins aligned and have the same flavor. Therefore it is necessary that each quark has a quantum number called color, and that there be at least three different colors.

Experimentally, the ratio of $\sigma_{e^+e^-\to\mathrm{hadrons}}/\sigma_{e^+e^-\to\mu^+\mu^-}$ is found be be equal to approximately 3.7 for center-of-mass energies above 10 GeV [20]. This is the predicted value to lowest order if the quarks are primary particles which become observable hadrons:

$$R = \frac{N_C \sum q_i^2}{q_\mu^2} = 11/3,$$

where $N_C = 3$ is the number of colors.

2.3 Models of Jet Hadronization

Since the process of hadronization is thought to take place at low-q^2, perturbative QCD calculations are not possible. The general approach is

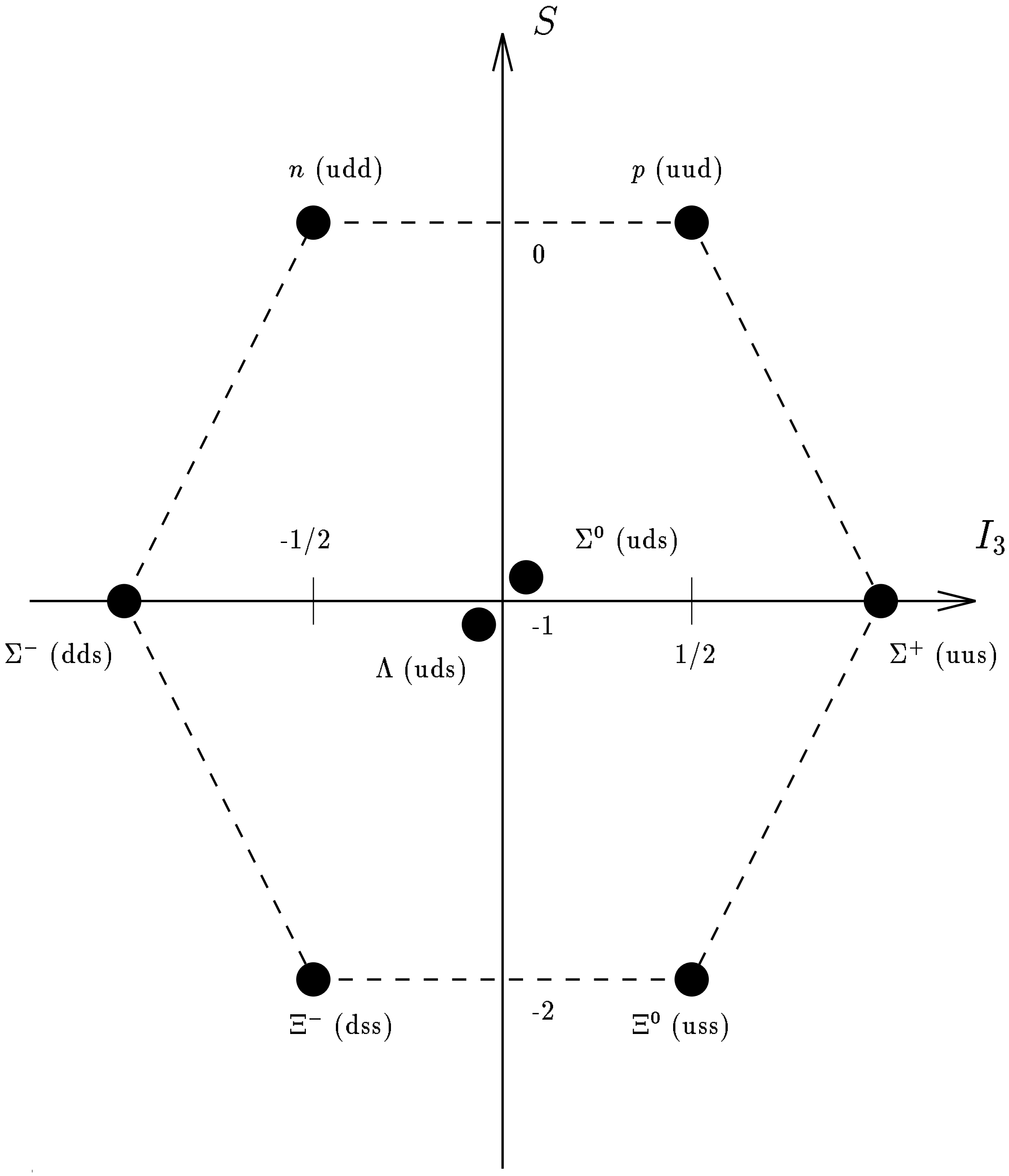

Figure 2.2: The octet of baryon states with $J^P = \frac{1}{2}^+$. The quark assignments are also given.

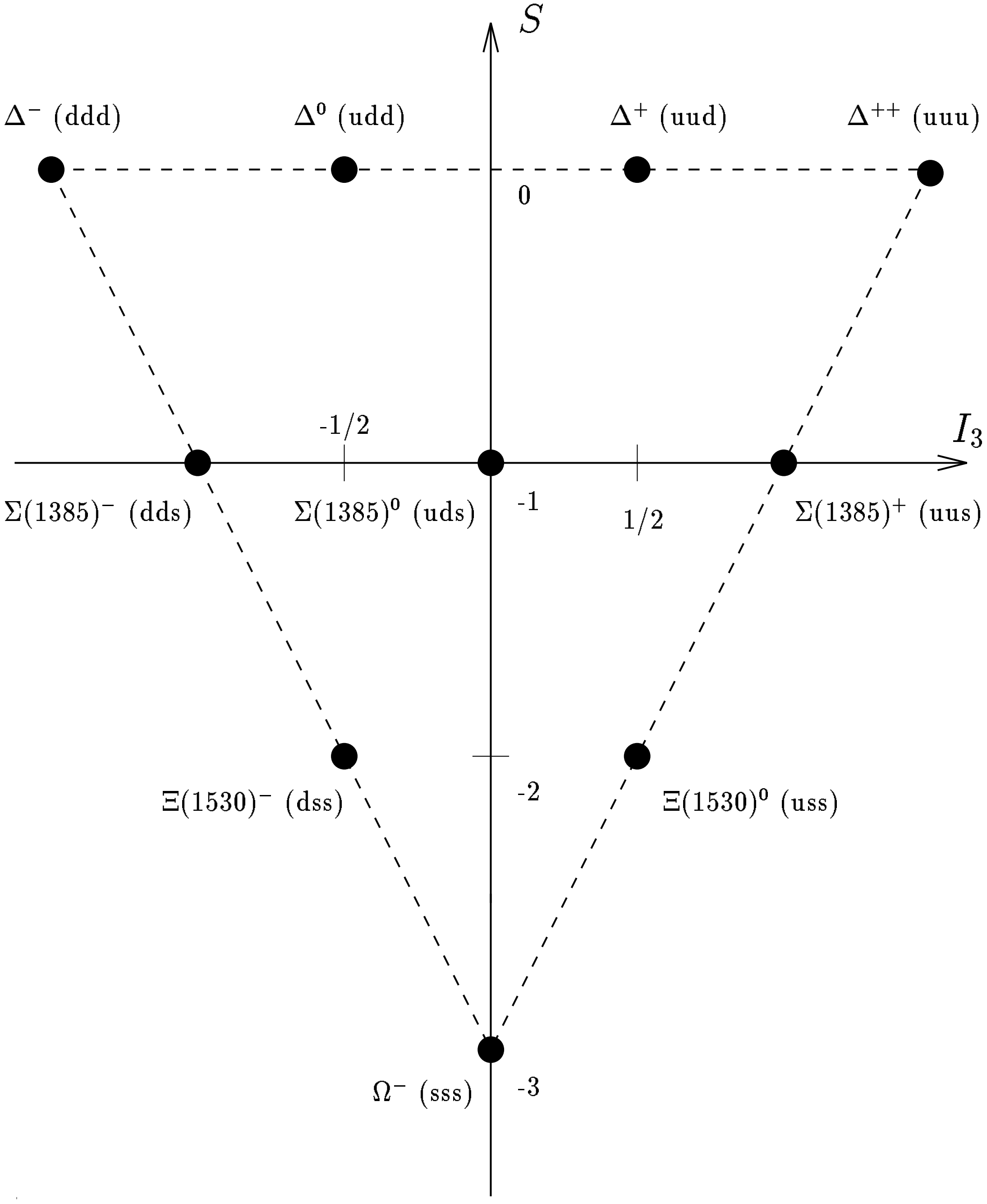

Figure 2.3: The decuplet of baryon states with $J^P = \frac{3}{2}^+$. The quark assignments are also given.

to use models of hadronization. There are many Monte Carlo models in existence which try to describe the fragmentation of quarks and gluons.

All Monte Carlo models use perturbative QCD calculations to describe the high-q^2 processes involving quarks and gluons. In general two methods are used: parton shower calculations and matrix element calculations. The parton shower approach is based on a leading logarithmic approximation of QCD. The evolution of a time-like parton shower from an initial virtual $q\overline{q}$ pair is governed by the various branching ratios $q \rightarrow qg$, $g \rightarrow gg$, and $g \rightarrow q\overline{q}$. For each process, the probability that the quark or gluon branches is given by a function of the invariant mass of the parton $Q^2 = m^2 = E^2 - \vec{p}^{\,2}$, and of the energy sharing between the two daughters. The daughters may then branch themselves and so on until a limit Q_0^2 (usually about 1 GeV) is reached, and the process is concluded [21]. The matrix element approach is different in that it uses exact matrix elements calculated from QCD, but only to a finite (second) order to determine the various branchings into 2-, 3-, and 4-jet event types [21].

Below momentum transfers of a few GeV, the coupling constant α_S increases to the point where perturbative calculations are not possible. It is for this reason that the process of the confinement of quarks into hadrons has not been described yet by a QCD-based theory. The common approach is to build a model of the subsequent fragmentation of the partons into observable final state hadrons. There are three main types of models: string fragmentation models (as used in JETSET [22]), cluster fragmentation models (as used in HERWIG [23]), and independent fragmentation models [24]. The first two types of models are briefly described below.

2.3.1 String Fragmentation Models

String models of hadronization are based on a picture of how quark-antiquark pairs evolve in time [25]. Since gluons have a color quantum number, they can couple to one another via the triple-gluon vertex. The gluons which couple to the initial quark-antiquark pair will themselves interact to form a narrow "color flux tube" between the quark and antiquark, with transverse dimensions on the order of 1 fm, the size of a typical hadron. The starting assumption of such models is that the color flux tube, or "string", will increase in potential energy linearly as it grows in length. When the energy of the string becomes sufficiently large, the string can fragment by the production of a $q\bar{q}$ pair from the sea. This process can continue so long as the invariant mass of the string is large enough to produce new $q\bar{q}$ pairs.

If a hard gluon is radiated in the final state, the picture is somewhat different. The string stretched between the quark and antiquark is also connected to the gluon, which forms a "kink" in the string. One prediction of this model is a higher particle multiplicity in the regions between quark and gluon jets, which was first observed by the JADE collaboration in 1981 [26].

Mesons are formed by grouping $q\bar{q}$ pairs. In JETSET, the spin and strangeness of the mesons are chosen according to adjustable probabilities, since the string model does not predict what these quantum numbers should be. The production of heavy flavors from the sea is greatly suppressed in JETSET [24].

To produce baryons, a somewhat more complicated model is necessary. The diquark model, as implemented in the JETSET Monte Carlo, is one approach, in which a string can break by the creation of a pair of diquarks in an antitriplet color state. The diquark is then combined with a quark to form a baryon. Parameters in the model set the probability for the strangeness and spin of diquarks.

The "popcorn" mechanism [27] is a modification of the diquark model, in which a meson is inserted in the chain between each baryon-antibaryon pair. The relative probability for the different types of chain is controlled by adjusting a single parameter within JETSET. The production of baryons using the popcorn chain results in weaker correlations in rapidity space between baryon-antibaryon pairs, because they are farther apart in the chain. A diagram of baryon production in the diquark model is shown in figure 2.4.

The UCLA Monte Carlo [28] is based on JETSET, and tries to reduce the number of parameters by proposing a single function which governs the relative production of the different hadrons. In this model, an average of 1.7 popcorn mesons are inserted in the chain between each baryon-antibaryon pair, resulting in even weaker rapidity correlations than in JETSET, which has at most one popcorn meson per baryon-antibaryon pair.

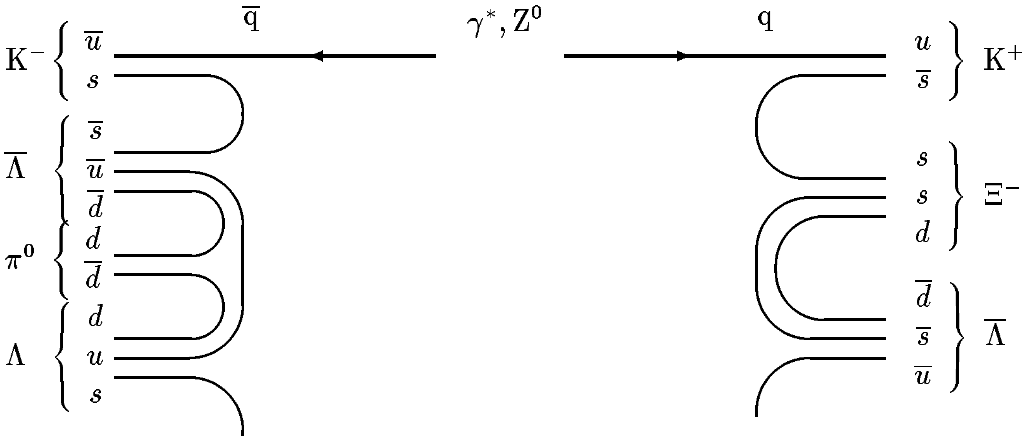

Figure 2.4: Schematic diagrams which show the chain-like production of baryon pairs. On the right is a baryon-antibaryon chain, while on the left is an example of the "popcorn" mechanism, in which a meson is inserted in the chain between the baryon-antibaryon pair.

2.3.2 Cluster Fragmentation Models

Cluster fragmentation models [29], such as employed in the HERWIG Monte Carlo [23], take a different approach to confinement. In these models, quark-antiquark pairs undergo "pre-confinement" in colorless clusters. Each cluster then decays isotropically into a two hadron final state, either a meson-antimeson pair, or a baryon-antibaryon pair.

The only parameters in HERWIG to which baryon production is sensitive are the maximum cluster mass, `CLMAX`, and `CLPOW`. For version 5.4 of HERWIG, these parameters were tuned so that the Λ rate agreed with the published rate from OPAL. Since the mass of clusters is low, the baryon-antibaryon pairs will have stronger rapidity correlations than in models with string fragmentation.

Chapter 3

The OPAL Detector at LEP

3.1 LEP

The LEP accelerator [30] is situated at CERN, the European Laboratory for Particle Physics, in Geneva. It has a circumference of 26.6 km and is designed to accelerate electron and positron beams to energies of up to 100 GeV. At the end of 1992, the four LEP experiments, ALEPH, DELPHI, L3, and OPAL, had each recorded more than one million hadronic Z^0 decays.

The first events were recorded at the LEP experiments in the summer of 1989. Since then time, LEP has been accumulating data at center-of-mass energies near the Z^0 mass. The introduction of superconducting RF cavities during 1993 and 1994 should allow an increase in the center-of-mass energy to levels sufficient to produce W^+W^- pairs (LEP200).

The LEP accelerator utilizes previously existing CERN accelerators for the injection chain [31]. Initially electrons are produced with a low-intensity electron gun. Positrons are produced using a 200 MeV LINAC which collides electrons with a fixed tungsten target. Both beams are then fed into a 600 MeV LINAC, and subsequently into the 600 MeV EPA (Electron-Positron Accumulator Ring). Once a sufficient number of particles have been accumulated, bunches of electrons and positrons are injected into the CERN Proton Synchrotron (PS) in opposite directions. In the PS, the bunches are accelerated to 3.5 GeV before they are in turn injected into the Super Proton Synchrotron (SPS). In the SPS, the bunches are accelerated to energies of 20 GeV and finally delivered to LEP. This injection system typically provides 3 mA of current in both beams.

The LEP ring itself has the shape of a rounded octagon, consisting of eight straight and eight curved sections. The eight experimental halls, four of which hold the large LEP experiments, are located in the centers of the straight sections.

3.2 The OPAL Detector

The OPAL detector [32] is pictured in figures 3.1 and 3.2. OPAL was designed to be able to reconstruct charged tracks and measure electromagnetic and hadronic energy and muons over almost the entire 4π solid angle.

The detector is composed of many sub-systems, including a central tracking system contained inside a solenoid which provides a uniform magnetic field of 0.435 T, a time-of-flight system, a lead glass electromagnetic calorimeter, a hadron calorimeter, a muon tracking system, and a forward detector. The analysis performed for this thesis makes use mainly of the

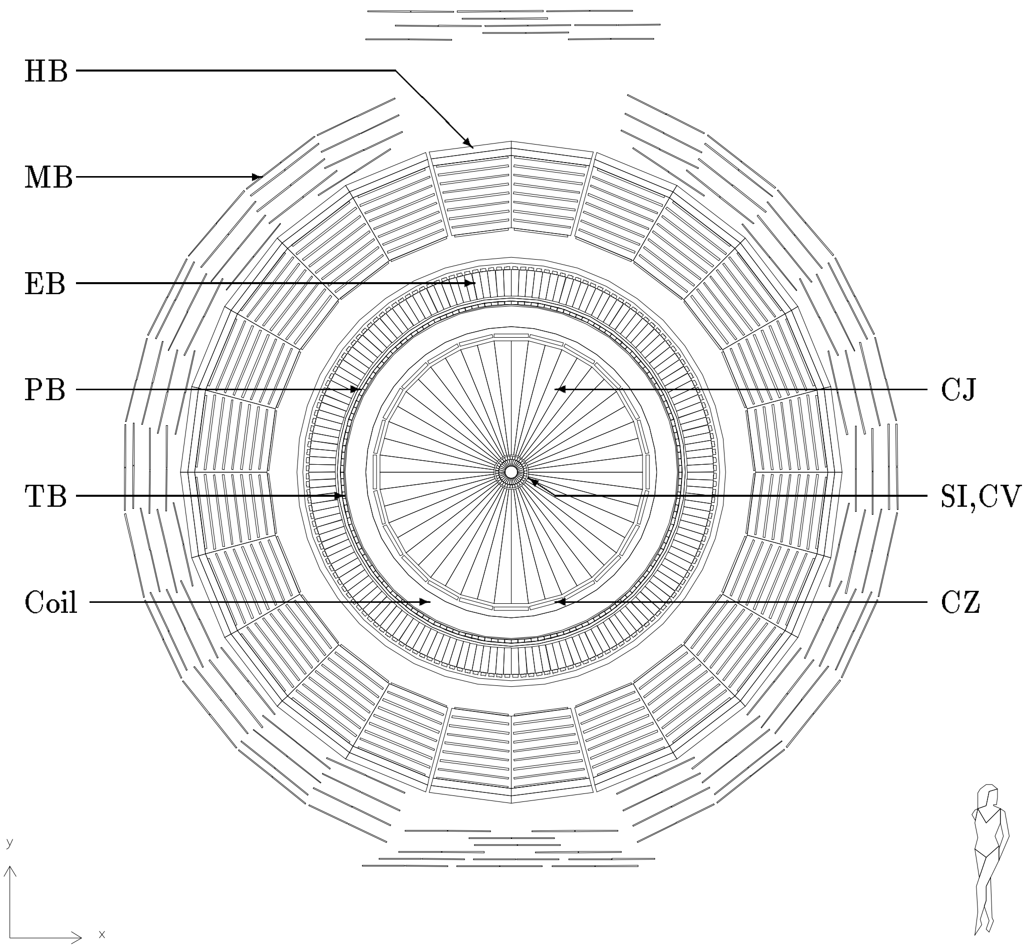

Figure 3.1: The OPAL detector as seen in the plane perpendicular to the beam. The various subdetectors are labelled according to their two-letter codes.

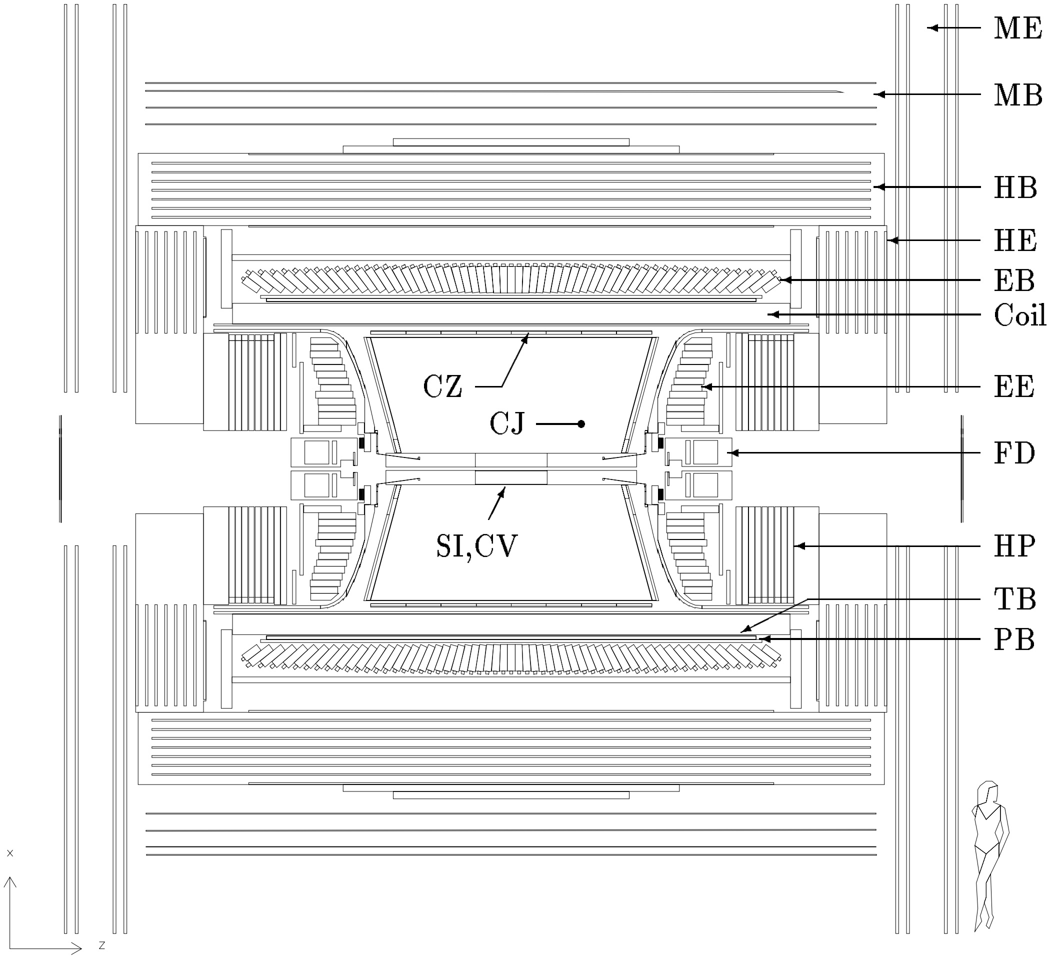

Figure 3.2: The OPAL detector as seen in the plane of the beam. The various subdetectors are labelled according to their two-letter codes.

central tracking chambers of the OPAL detector.

The coordinate system used in OPAL is the one in which the x axis points towards the center of the LEP ring (which is tilted at an angle of 13.9 mrad with respect to the horizontal plane), the y axis points approximately upwards, and the z axis points in the direction of the electron beam and the magnetic field produced by the solenoid. Frequently, quantities are expressed in terms of the cylindrical coordinates r, the radial distance from the center of the detector, ϕ, the azimuthal angle in the x-y plane as measured from the x axis, and θ, the polar angle with respect to the z axis.

3.2.1 The Central Detector

The central tracking system is made up of four components: a silicon micro-vertex detector (SI) installed in 1991, a central vertex chamber (CV), a jet chamber (CJ), and z-chambers (CZ). The central detector is operated in a 0.435 T magnetic field produced by a solenoid. CV, CJ and CZ are contained in a pressure vessel under a total gas pressure of 4 bar. The gas used in the central detector is a mixture of argon (88.2%), methane (9.8%), and isobutane (2.0%).

The innermost element of the central detector is the silicon micro-vertex detector (SI). SI is used mainly for the reconstruction of secondary vertices, for example from τ or b decays. Single-sided silicon microstrip detectors are arranged in two barrels at radii of 6.0 and 7.5 cm, the inner barrel having 11 ladders and the outer barrel having 14. A ladder consists of three detectors and is 18 cm long. The resolution of impact parameters of tracks with hits in SI has been measured to be $\sigma_{d_0} = 22\mu\text{m}$ at 45 GeV [33].

The vertex chamber (CV) is a one meter long cylindrical drift chamber. CV is divided into 36 sectors and two layers, the first layer containing axial wires strung parallel to the beam radially from 10.3 to 16.3 cm with a spacing of 5 mm, and the outer layer containing stereo wires inclined at an angle of 4° relative to the beam from a radius of 18.8 cm to 21.3 cm with a spacing of 5 mm. The vertex chamber allows the reconstruction of secondary vertices as well as an impact parameter resolution of $\sigma_{d_0} = 40\mu\text{m}$ [33].

The central jet chamber (CJ) is the main component of the central tracking system used in this analysis. It is a large drift chamber 4 meters long and is used in conjunction with the vertex chamber and the outer z-chambers to measure the curvature, position, and energy loss of charged particle tracks. CJ is divided into 24 sectors, each sector containing 159 sense wires spaced every centimeter from a radial distance of 25.5 cm to 183.5 cm.

The momentum resolution in the jet chamber is described by the formula $\sigma_{p_t}/p_t = \sqrt{(2\%)^2 + (0.15\% \cdot p_t)^2}$, where the first term is for multiple scattering in the gas and in the beam pipe, and the second, momentum dependent term has been determined from an analysis of muon pairs [33]. The tracking efficiency for single track within a jet was found to be 97.7%, for tracks with $p_t > 100$ MeV and $|\cos\theta| < 0.95$ [33]. Particle identification in the central detector is obtained from the measurement of the energy loss of charged particles in the gas. The details of the particle identification will be discussed in Chapter 4.

The outermost segment of the central detector is formed by the z-chambers (CZ) which measure the z position of central detector tracks. The z-chambers are composed of 24 cylindrical drift chambers 4 m long, 50 cm wide, and 59 mm thick, covering the range of polar angles $|\cos\theta| < 0.72$. There is a plane of anode wires strung in the ϕ direction and with a spacing of 4 mm every 50 cm. The wires are staggered by ± 250 μm to resolve left-right ambiguities. The z-chambers have a measured spatial resolution of 300 μm, with an efficiency of 83% for tracks with a transverse momentum relative to the beam greater than 1 GeV [32].

3.2.2 The Electromagnetic Calorimeter

The electromagnetic calorimeter is a lead glass calorimeter which consists of three overlapping sections. The barrel (EB) consists of 9440 lead glass blocks placed between the magnetic coil and the return yoke of the magnet at a radius of 2.455 m out to a $|\cos\theta| <$0.82. The blocks are angled so that they point roughly in the direction of the interaction region. Each block subtends an angle of approximately 40 mrad by 40 mrad. The two endcaps (EE) consist of 2264 blocks placed parallel to the beam direction and extend the angular coverage through the range $0.81 < |\cos\theta| < 0.984$.

The intrinsic energy resolution of the lead glass is $\sigma_E/E = 6.3\%/\sqrt{E}$. Since there are about two radiation lengths of material in front of the calorimeter, electromagnetic showers often begin to develop before they reach the calorimeter. To improve the energy and position resolution , a presampler was installed in front of the electromagnetic calorimeter. With the material in front, the energy resolution of 45 GeV electrons was measured to be 3.4% in the barrel region.

3.2.3 The Time-of-Flight System

The time-of-flight system (TOF) sits in front of the barrel electromagnetic calorimeter. The TOF system consists of 160 scintillation counters arranged in the barrel region out to a $|\cos\theta| < 0.82$, at a radius of 2.36 m.

By measuring the time of flight of particles from the interaction region, particle identification at low momentum can be achieved. The signals from the TOF system are also used to reject cosmic ray events.

3.2.4 The Hadron Calorimeter

The function of the hadron calorimeter is to measure the energy of hadrons which are not absorbed in the electromagnetic calorimeter and to assist in the measurement of muons. It is composed of three parts: the barrel (HB), the endcaps (HE), and the pole-tip calorimeter (HP).

The barrel HB is composed of the return yoke of the OPAL magnet with nine layers of limited streamer tubes. The return yoke is divided into eight layers, alternating with the active detector regions. In the barrel, HB extends from a radius of 3.39 m to 4.39 m. Signals are read out on either end of the chambers. On the outer side are large pads (50 cm × 50 cm) which are read out as analog pulses, and on the inner side are long 4 mm wide cathode strips which run the length of the chambers. The strips are spaced every 10 mm. Layers of pads are grouped together to form towers, providing an estimate of the energy of hadronic showers. The strip hits can be used in the identification of muon tracks or the measurement of hadronic showers. In a typical multihadron event, there are on average 45 strip hits and 16 GeV of energy measured by the towers.

The energy resolution is limited mainly by the material in front of the calorimeter and the sampling frequency. The intrinsic energy resolution was found to be $\sigma_E/E = 120\%/\sqrt{E}$ [32].

The endcap calorimeter (HE) has a similar configuration (with only 8 layers) and shares data acquisition, high voltage supplies, and gas supplies with the barrel. The endcaps have inner radii of 1.91 m and outer radii of 3.301 m, and are divided into four quadrants.

The pole-tip calorimeter (HP) is composed of ten layers of multiwire chambers operated in a high gain mode, alternating with iron slabs. HP covers the far forward region in the polar angle $0.91 > |\cos\theta| > 0.99$.

3.2.5 Other Subdetectors

The muon tracking chambers are the outermost subdetector of the OPAL experiment. The barrel (MB) consists of drift chambers which cover the range in the polar angle $|\cos\theta| < 0.72$. The endcap (ME) extends the coverage down to $|\cos\theta| < 0.98$. The hadron calorimeter strips can be used in conjunction with the muon chambers to provide measurements of muon tracks.

The measurement of the luminosity is performed by the forward detector. The luminosity is measured by the detection of low angle Bhabha scattering events, a process which is insensitive to the presence of the Z^0 resonance. The forward detector consists of several components, including a calorimeter, proportional tube chambers, drift chambers, the fine luminosity monitor, the gamma catcher, and far forward monitor counters. The luminosity measurement is performed with the calorimeter and tube chamber information [34].

3.3 Triggering and Data Acquisition

The trigger has to make a fast decision about whether to accept or reject an event with high efficiency for real e^+e^- processes, such that the rate of events which are actually read out is low enough for the data acquisition systems and electronics to handle. The LEP beam crossing interval was 11 μs after eight on eight bunch running was introduced in 1992. This represented a factor of two decrease in the interval from previous years.

To meet this new requirement, a two stage triggering system was implemented [35] (see figure 3.3). A hardware pretrigger makes a decision based on certain criteria whether an event is “good”. This pretrigger reduces the 91 kHz bunch crossing frequency down to a 1-2 kHz rate of accepted pretriggers. Still this rate is too high, so a second level trigger, which was the original OPAL hardware trigger, makes further cuts, reducing the accepted event rate to a few events per second. Typical event rates in 1992 were on the order of 3-6 Hz, with dead times of less than 6 μs for each subdetector, the hadron calorimeter strips having the smallest dead time of only 680 ns.

The original trigger system of OPAL, which was the main first level trigger during the 1990 and 1991 runs, makes use of the hardware triggers of several subdetectors. The system is highly redundant and has nearly 100% efficiency for accepting most types of events seen in the detector.

The various subdetectors have hardware triggers which are then combined by the central trigger VME electronics. The track trigger is provided by the axial wires of the vertex chamber and central detector. If there are tracks originating from the interaction region, they will have hits at a constant value of θ. The total energy in the electromagnetic calorimeter is also used as a trigger. Using analog signals, the sums of the energy in the barrel and two endcaps are sent as a trigger if certain energy thresholds are met. Other triggers originate from the time-of-flight scintillators, the hadron calorimeter, muon chambers, and the forward detector calorimeter.

All of these various triggers are fed to the central trigger logic, which combines them all into a single trigger decision. Information from subdetectors which provide trigger information in θ and ϕ (TT, TOF, EB, EE, HB, HE, MB, and ME) is combined and analysed. If one θ-ϕ bin is above a certain threshold, or patterns are seen in the bins (back-to-back hits, coincidences), then the trigger decision is positive [36].

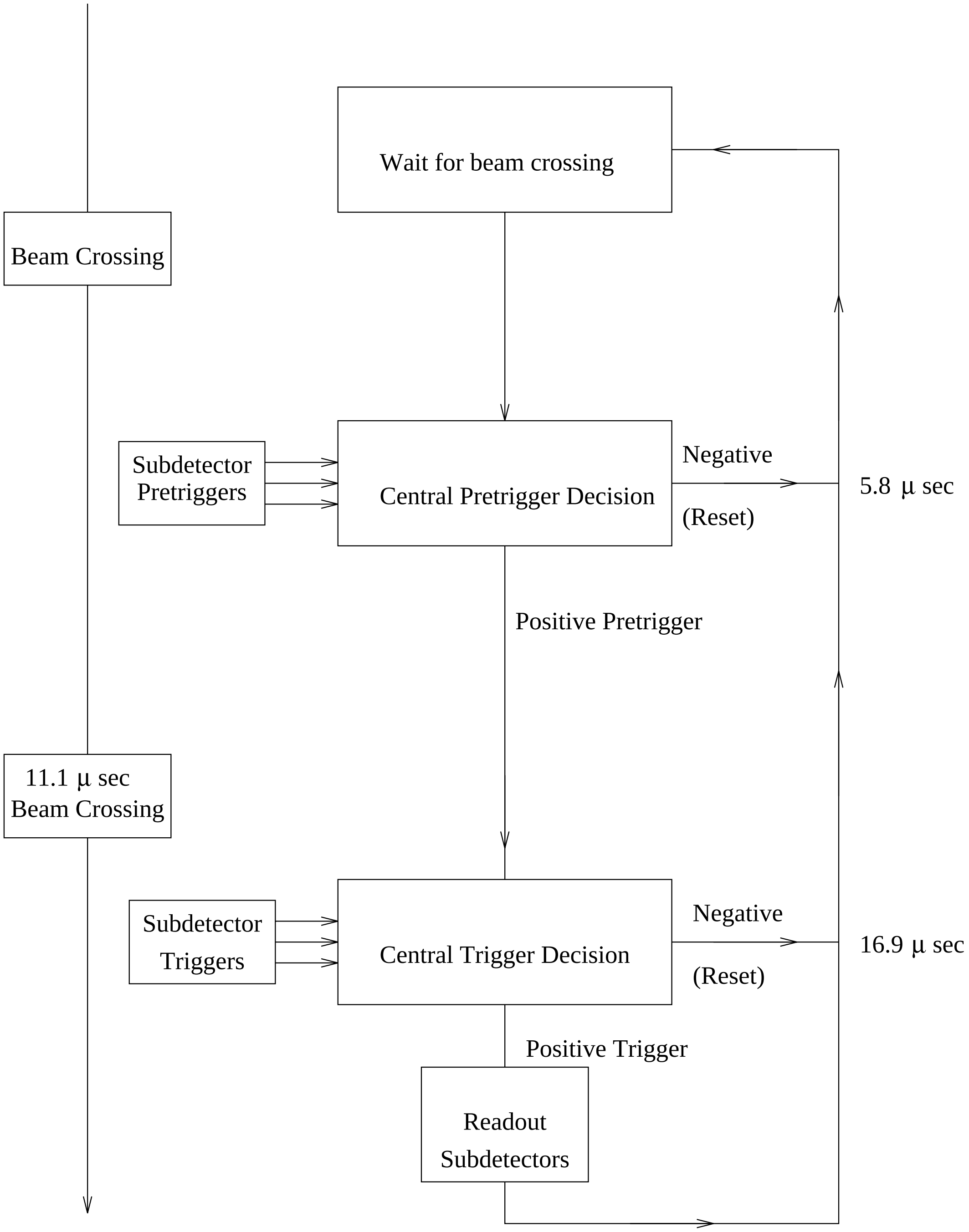

Figure 3.3: An overview of the 1992 triggering setup in OPAL.

This trigger performed well during the 1990 and 1991 runs and continued to do so subsequently. The trigger efficiency for most types of events was almost 100% within the trigger acceptances. For example, within the region $|\cos\theta| < 0.95$, the trigger efficiency for events of the type $e^+e^- \rightarrow \mu^+\mu^-$ was measured to be $99.9 \pm 0.1\%$ [36]. For multihadrons, the efficiency was measured to be 100%.

At the beginning of the 1992 run, the pretrigger began operation. After each beam crossing, the pretriggers from the various subdetectors (CV, CJ, TB, EB, EE, ME, and FD) are fed into the central pretrigger logic. There is a gate of 5.3 μs in which pretrigger signals are accepted. A pretrigger decision is then made based on the ϕ information of the various subdetector pretriggers. This decision takes approximately 200 ns. The pretrigger will reset the detector after 5.8 μs if the decision is negative, well before the next beam crossing [35]. If the decision is positive, the event is saved for a trigger decision.

The data acquisition system of the OPAL experiment is a VME-based system [37]. This system controls the data acquisition, performs monitoring of the subdetectors, reconstructs events, and calibrates the various subdetectors. At the lowest level, each subdetector has its own data acquisition system, which can run independently of the central DAQ. If the trigger decision is positive, the VME trigger crate signals the subdetectors that the event will be read out by the "event builder", a dedicated VME crate which merges all of the separate subdetector output into a complete event. These events are then sent to the filter, after which they can be fully reconstructed.

The event filter in OPAL acts as a secondary software trigger [38]. The filter serves several purposes. Not only does it reject backgrounds which are accepted by the hardware trigger (cosmic rays, beam gas interactions, etc.), but it also makes a preliminary classification of the events according to different types (multihadrons, lepton pairs, luminosity events etc.), and performs some basic on-line monitoring of the data. The event filter further reduces the rate of accepted events by about 30% [35]. The filter is also capable of holding up to 12 hours of data (at current rates) in a buffer, which allows the subsequent processing of the data to be run independently from the data acquisition [37].

3.4 Event Reconstruction and Detector Simulation

Event reconstruction is the process of converting raw detector data into physical quantities such as momentum and energies. The OPAL experiment has a system in which the data are available for monitoring and analysis very soon after the data is taken, allowing the operators to identify and diagnose problems quickly and efficiently [37].

The initial reconstruction takes place on a network of computer workstations at the experimental site. Since the filter can buffer up to 12 hours of data, the reconstruction of events can take place at its own pace, and can have access to the database of calibration information provided by the

DAQ systems. Events are reconstructed using the ROPE suite of programs, named for the **R**econstruction of **OP**AL **E**vents.

Monte Carlo simulations of OPAL data are made using the GOPAL program [39], a set of routines adapting the CERN detector simulation program GEANT [40] for use in OPAL. This program simulates the passage of charged and neutral particles through the active and passive materials of the detector, and stores "hits" for the active areas. The program can also be used in conjunction with ROPE to produce event records in standard OPAL format.

3.5 The Multihadron Event Sample

Multihadronic events are selected according to the criteria detailed in [41]. Events are required to have more than 5 good tracks and 7 good electromagnetic clusters, where a "good track" is defined as having

- more than 20 central detector hits,
- the radius of the first hit less than 60 cm from the event vertex,
- the impact parameter of the tracks with the event vertex in the plane perpendicular to the beam less than 2 cm and in the plane parallel to the beam less than 40 cm,
- the transverse momentum with respect to the beam axis more than 50 MeV,

- $|\cos\theta| < 0.95$,
- and the χ^2 of the fits to the track hits less than 999.

The events are also required to pass the following visible energy and energy balance cuts,

$$R_{\text{visible}} = \frac{\sum E_{\text{raw}}}{2E_{\text{beam}}} \geq 0.10$$

and

$$R_{\text{balance}} = \frac{\sum E_{\text{raw}} \cos\theta}{\sum E_{\text{raw}}} \leq 0.65 \ ,$$

where E_{raw} is the energy of electromagnetic calorimeter clusters before any corrections are applied for the material in front of the calorimeter and before any presampler corrections. The clusters must have more than 1 (2) blocks in the barrel (endcap) and more than 100 MeV (200 MeV) in raw energy.

The efficiency of the selection has been estimated to be 98.4%, with backgrounds at the 0.1% level, mostly from $Z^0 \rightarrow \tau^+\tau^-$ events [41]. With the above criteria, a total of 135,819 multihadron events from the 1990 data sample, 342,603 from 1991, and 762,198 from 1992, were selected, for a total of 1,240,060 multihadronic Z^0 decays.

Chapter 4

Inclusive Strange Baryon Production

Strange baryons can be reconstructed by their decays into charged particles in the central tracking chamber. Geometric signatures and particle identification using dE/dx measurements are combined to reduce backgrounds and optimize signals.

The Λ decays primarily into $p\pi^-$ (see table 4.1) with a distinctive geometric signature. Since the Λ has a decay length of 7.89 cm, Λ candidates

Baryon	Decay Mode	$c\tau$
Λ	$p\pi^-$ (64.1%)	7.89 cm
Ξ^-	$\Lambda\pi^-$ (100%)	4.91 cm
$\Sigma(1385)^\pm$	$\Lambda\pi^\pm$ (88%)	$\Gamma \approx 35$ MeV
$\Xi(1530)^0$	$\Xi^-\pi^+$ (67%)	$\Gamma = 9.1$ MeV
Ω^-	ΛK^- (67.8%)	2.46 cm

Table 4.1: Decay modes and lifetimes of the strange octet baryons (spin 1/2) Λ and Ξ^-, and several decuplet (spin 3/2) strange baryons.

can be selected by identifiying secondary verticies of oppositely charged tracks well displaced from the primary event vertex. An example of such a decay is shown in figure 4.1.

Apart from general requirements that there be a well defined intersection of the two tracks, there are also several kinematic variables which can be used to reduce backgrounds. Most of the charged tracks in a typical multihadron event come from the event vertex. Therefore, one can reduce backgrounds considerably by requiring that the radial position of the track intersection be large and that the impact parameters of the tracks with respect to the event vertex also be large.

Apart from using geometric signatures, particle identification with the dE/dx measurement also can be used to reduce backgrounds. A plot of the energy loss due to ionization of the jet chamber gas is shown in figure 4.2. The energy loss in the central detector gas is a function of only the relativistic velocity $\gamma\beta = p/m$ and the properties of the gas and is described by the Bethe-Bloch formula. There is excellent separation of charged pions, protons, electrons, and kaons over a large momentum range.

The maximum number of hits used in the calculation of the energy loss is 159, for which the dE/dx resolution was measured to be 3.5% for pions in multihadronic events [42]. The resolution decreases if fewer hits are used in the calculation of the energy loss. A larger number of required hits reduces the efficiency whereas a lower number degrades the separation of the different particle types. In an average multihadronic event, more than 30% of the

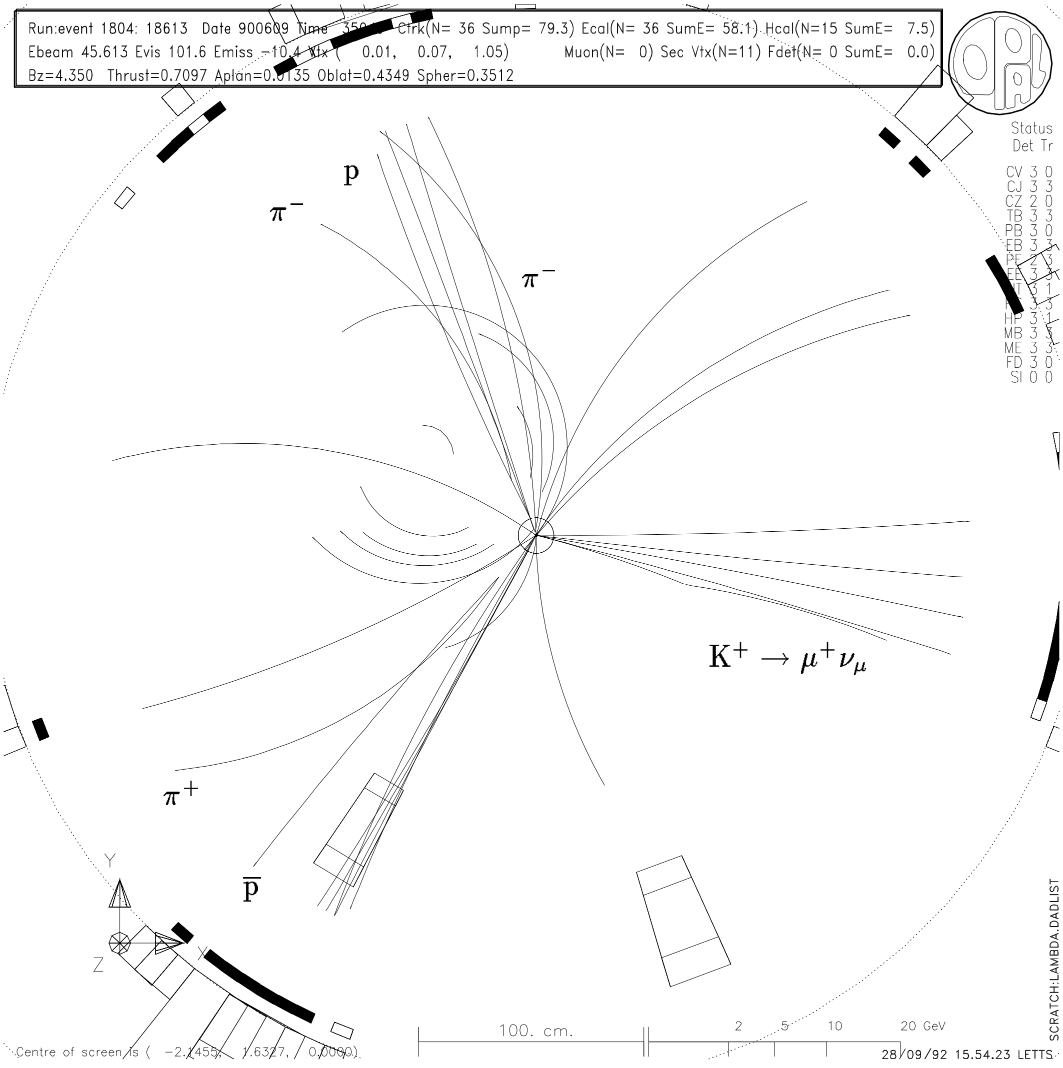

Figure 4.1: A three jet event with a reconstructed $\overline{\Lambda}$ in the lower left jet and a Ξ^- in the upper jet. Also, a decay $K^+ \to \mu^+\nu_\mu$ is evident from the kink in one tracks of the third jet, nicely compensating the strangeness of the two baryons.

hits are unusable for the dE/dx calculation, because tracks overlap or are close to chamber boundaries [42]. As can be seen in figure 4.2, even with a requirement that there be at least 20 dE/dx hits, there is good separation (up to 3σ) of the pion, proton, and kaon bands over large momentum ranges. In the cross-over region between 900 MeV and 1.5 GeV, identification becomes difficult because of the small separation of the bands. For the purposes of this analysis, the dE/dx measurement is considered reliable only if more than 20 hits were used in the calculation.

For the dE/dx measurement, cuts are often made not only on the value of the ionization energy loss, but also on the dE/dx "weight", which is the probability for the particle to be of the identified type, based on a Gaussian distribution around the expected mean energy loss for that type of particle.

Certain quality cuts are also made on the charged tracks themselves to insure that the momentum resolution is good and that low energy tracks and tracks originating from hadronic interactions with the material or the detector are rejected. In the analysis, charged tracks are considered only if they satisfy the following criteria:

- There are more than 40 wire hits in the central jet chamber (CJ).
- The first reconstructed hit on the track has a radius of less than 140 cm.
- More than half of the geometrically possible hits in CJ are found.
- The transverse momentum of the track with respect to the beam axis, p_t, is greater than 100 MeV.

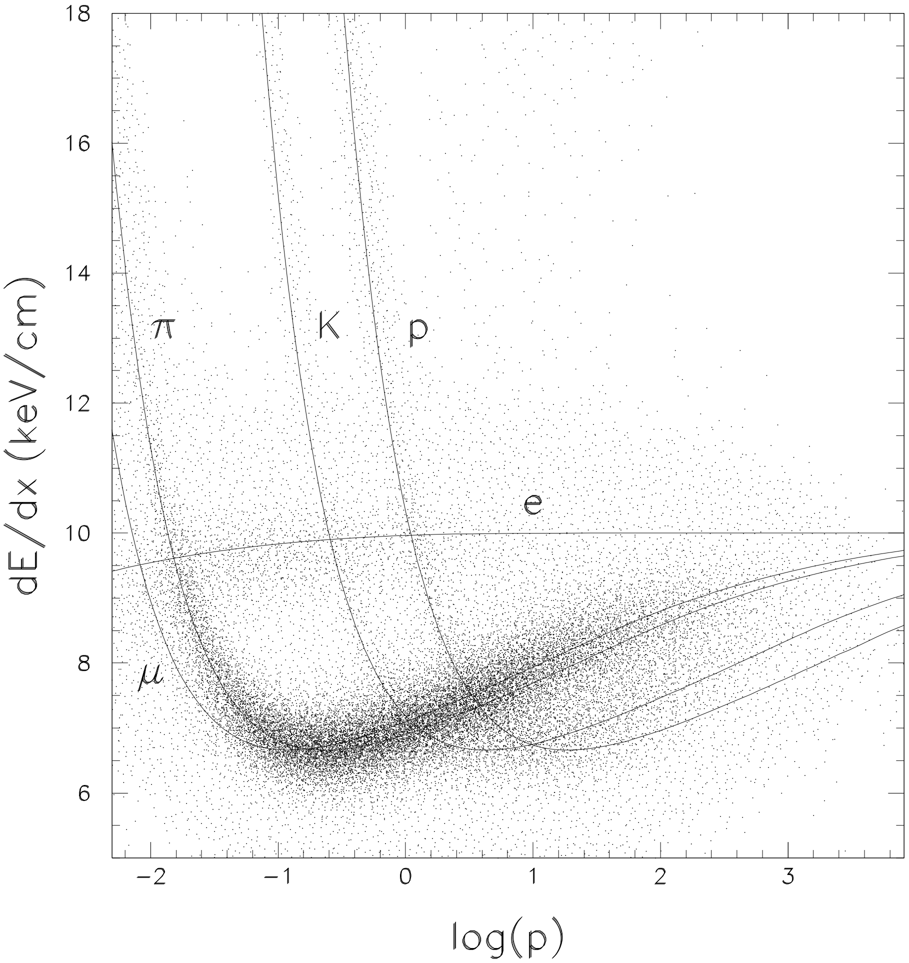

Figure 4.2: The energy loss of charged particles in the gas of the central detector, with a requirement on the minimum number of hits used in the dE/dx calculation $N_{hits} \geq 20$.

- The polar angle of the track satisfies $|\cos\theta| < 0.96$.
- The impact parameter in r-ϕ of the track with the event vertex, $|d_0|$, is less than 100 cm. [1]
- The absolute value of the z coordinate of the point of closest approach of the track with respect to the event vertex, $|z_0|$, is less than 100 cm.

After these cuts, there are typically more than 20 good charged tracks in a multihadronic Z^0 decay event. With a cut on the thrust axis of $|\cos\theta_{thrust}| < 0.7$, insuring that the event is well-contained inside the detector volume, we observe between 24-25 "good" tracks per event, although some of these come from interactions or are badly measured low energy tracks. The average charged track multiplicity in OPAL, corrected for acceptance and backgrounds, is 21.40 ± 0.43 tracks per multihadron event [43].

4.1 Λ Production

Λ baryons can be identified by their decays into $p\pi^-$. The selection has been optimized for a large acceptance over the whole momentum range, since the reconstructed Λ baryons are used to search for the other baryon species. For other studies, in which it might be necessary to optimize the signal to background for good mass resolution or for certain momentum regions, the selection criteria would be different.

---

[1] The OPAL track parameter, d_0, is the *signed* impact parameter, $d_0 = -q_g \times (r - \sqrt{x_c^2 + y_c^2})$, where (x_c, y_c) is the center of curvature and q_g is the geometric charge. The geometric charge is +1(-1) for positive (negative) $d\phi/ds$. The event vertex is calculated on an event-by-event basis.

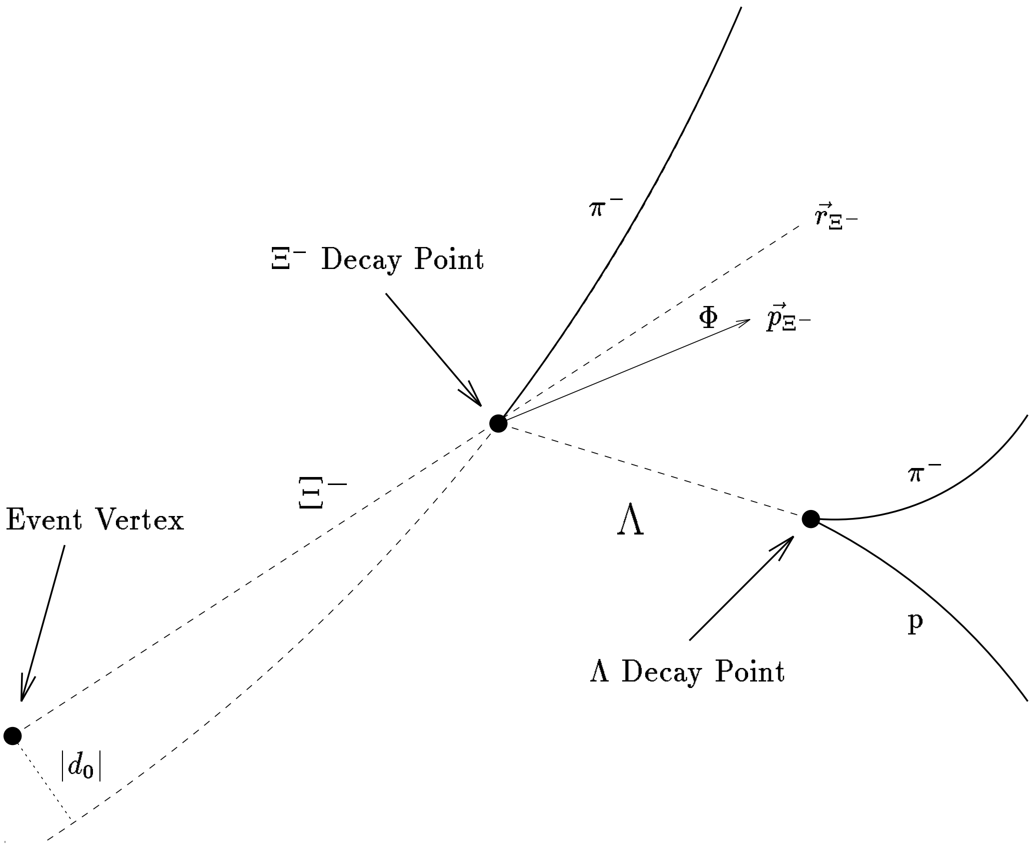

Figure 4.3: Geometric variables which are used in the cuts.

All combinations of oppositely charged tracks are considered. The higher momentum track is assigned to be the proton. The following geometric cuts on the combination are then made (see figure 4.3):

- The impact parameter of the proton track with the event vertex, $|d_0|$, must be greater than 0.5 mm. For the pion track, $|d_0|$ must be greater than 3 mm.

- The two tracks are required to have at least one intersection in the r-ϕ plane on the same side of the interaction point as the combined momentum vector. If there are two intersections, the closer to the primary event vertex is chosen, unless (a) the first reconstructed hits on the two tracks are after the closer intersection, or (b) one track has its first hit after the farther intersection and the other track has its first hit before, and the angle Φ between the reconstructed momentum vector and the vector which points from the event vertex to the assumed decay point is smaller for the farther intersection.

- If there are hits more than 5 cm upstream from the intersection on both tracks, the combination is rejected.
- The decay length, which is the radial distance of the assumed decay point, is required to be between 1 cm and 130 cm.
- The angle Φ, defined above, must be less than 30 mrad and less than $10{+}20/p_t$ mrad.
- The angle θ^* between the proton direction in the Λ rest frame and the Λ direction, must satisfy $|\cos\theta^*| < 0.98$.
- If the decay radius is less than 25 cm, the points of closest approach of the two tracks must be found on opposite sides of the event vertex, i.e. $d_0(\mathrm{p}) \times d_0(\pi^-) < 0$.
- The scaled momentum $x_p = p_\Lambda/E_{beam}$, must be greater than 0.01.
- The polar angle of the reconstructed Λ momentum vector must satisfy $|\cos\theta| < 0.9$.

Some distributions of the cut variables used above for selecting Λ candidates are shown in figure 4.4, compared with the corresponding distributions for the Monte Carlo with full detector simulation. The agreement is generally good although there are some small disagreements, such as in the decay radius (due to the fact that the Λ fragmentation function is too hard in the Monte Carlo, described later in section 4.6) and the number of hits for soft π^- tracks.

If there are 4 or more z-chamber hits on both tracks or the radius of the assumed decay point is greater than 20 cm, the tracks are re-fitted in θ such that they are constrained to the assumed Λ decay point instead of the event vertex. The z position of the Λ decay point is taken to be the average z position of the two tracks. As can be seen in figure 4.5, before the re-fit, charged tracks are constrained to the event vertex. This will cause an error in the measurement of the direction of the z component of the momentum, if the tracks actually originate from a secondary vertex some distance away from the primary event vertex. For high momentum Λ's, for which the mass resolution depends mainly on the accurate reconstruction of the opening angle and which generally decay farther away from the event vertex, the improvement is considerable.

Other cuts are made to reduce backgrounds from photon conversions and random combinations which fake a V^0 signature. If the invariant mass of the track combination, assuming the tracks are electrons, is less than 40 MeV, the combination is rejected as a probable photon conversion. Photon conversions make up a few percent of the original background. With this cut and the

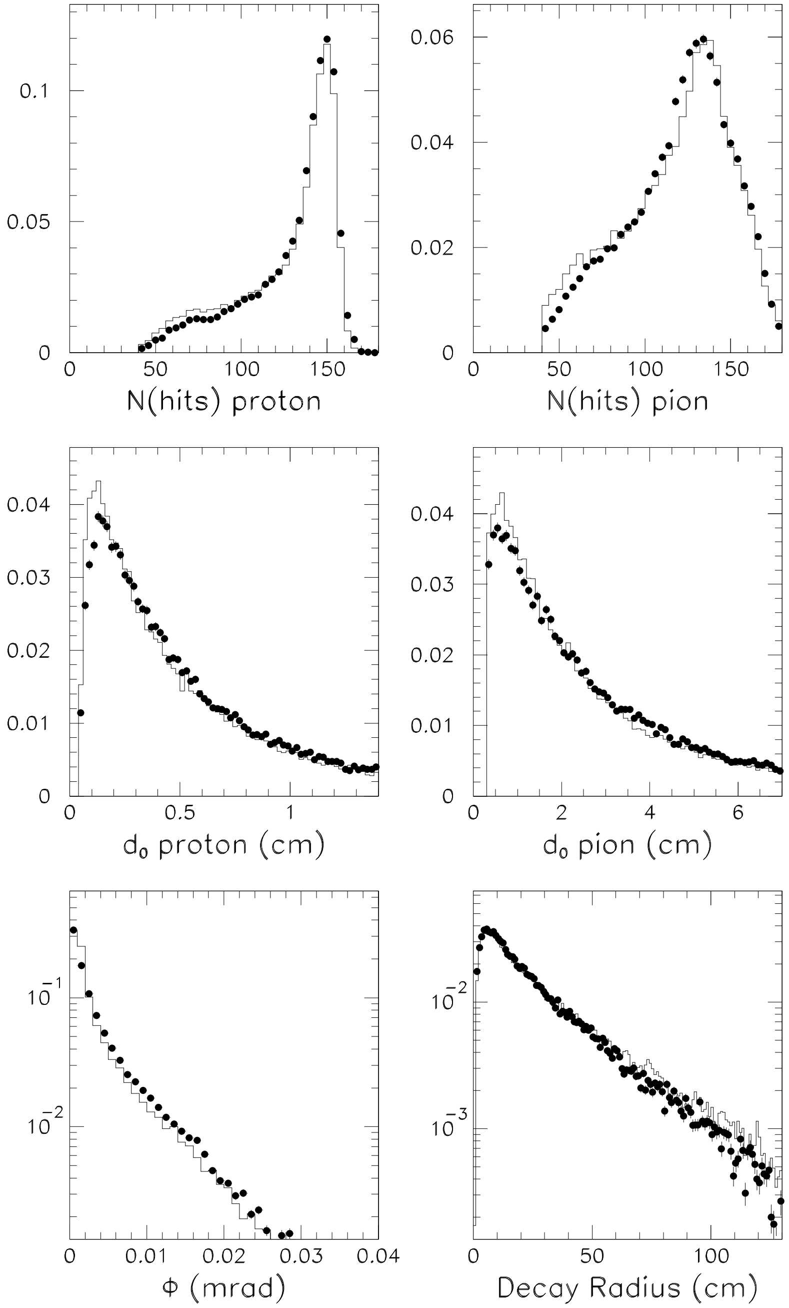

Figure 4.4: Distributions for various cut variables for Λ's in the data (points) and Monte Carlo (histogram). The areas under all of the curves are normalized to 1.

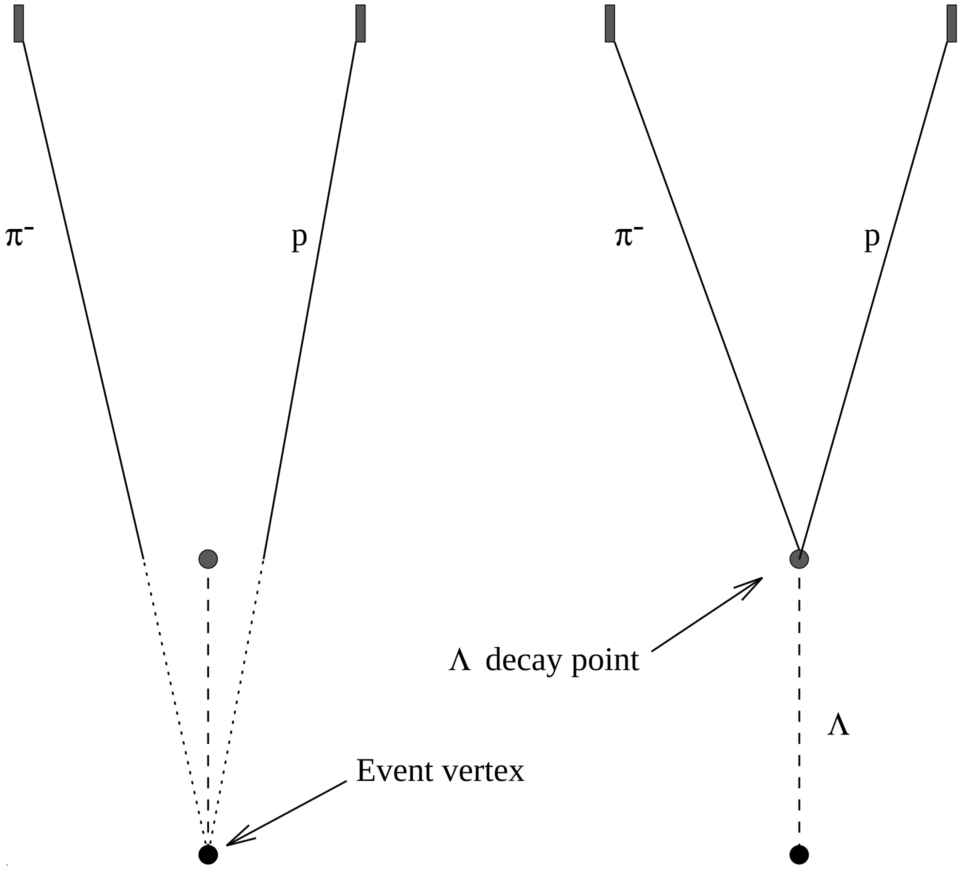

Figure 4.5: Result of re-fitting the tracks in z to the assumed Λ decay point. Before the re-fit (left) the tracks are constrained to the event vertex. After un-constraining the tracks and re-constraining them to the assumed Λ decay point (right), the momentum resolution in z is greatly improved.

dE/dx requirements made on the tracks, nearly all such combinations are removed.

The angle θ^* between the proton direction in the Λ rest frame and the Λ direction, must satisfy $|\cos\theta^*| < 0.98$. Background combinations will have their decay angle in the extreme forward or backward direction.

One major source of background is pions which fake protons in the V^0 decay, such as from the decay $\mathrm{K^0_S} \rightarrow \pi^+\pi^-$. One can reduce this background by cutting on the dE/dx of the proton candidate, thus eliminating proton candidates which are actually pions. Only relatively loose cuts on the dE/dx are made, since the idea is to reduce backgrounds as opposed to positively identifying the proton and π^-, which would lead to a large loss in efficiency and possible systematic effects. Since the curves for the energy loss of different types of particles cross one another (see figure 4.2), momentum dependent cuts are used. If more than 20 dE/dx hits are found for either track, the tracks are required to pass the following momentum dependent cuts on the energy loss and the dE/dx weight:

1. For the proton track:
    - If the momentum is less than 1.5 GeV, the dE/dx must be greater than 8 keV/cm and the proton weight must be greater than 0.5%.
    - If the momentum is greater than 1.5 GeV and less than 2 GeV, the dE/dx must be less than 8.5 keV/cm. In this region, the proton energy loss is about 7.0 keV/cm.

- If the momentum is greater than 2.0 GeV, the proton weight must either be greater than the kaon weight or 5%, whichever is less.

2. For the pion track, the pion weight must be greater than 0.1%.

With these cuts, a narrow, almost Gaussian peak is found in the $p\pi^-$ invariant mass distribution, shown in figures 4.6 and 4.7. The dominant backgrounds are from $K^0_S \to \pi^+\pi^-$ decays and random combinations which fake V^0 decays (see figure 4.8).

The resolution of the signal depends strongly on the number of tracks with z-chamber hits. As can be seen in figure 4.9, the resolution is degraded for combinations without z-chamber hits or cases in which the Λ passed outside the acceptance of the z-chambers. In order to have a large acceptance, all possible combinations are used in this analysis, since reliable signals can be seen with each.

The Λ signal has long, non-Gaussian tails which are difficult to fit. Therefore, in order to have a consistent way of estimating the background, the method chosen to estimate the backgrounds in the present analysis is to utilize the information in the side-bands. The level of the background in mass intervals well outside the Λ signal region should bear a direct relationship to the background under the signal itself, if the regions are suitably chosen on either side of the signal.

Since the mass resolution degrades as momentum increases, by using a momentum dependent definition of the signal region we can be sure of a large acceptance. The signal region is taken to be ±10 MeV about the Λ mass of

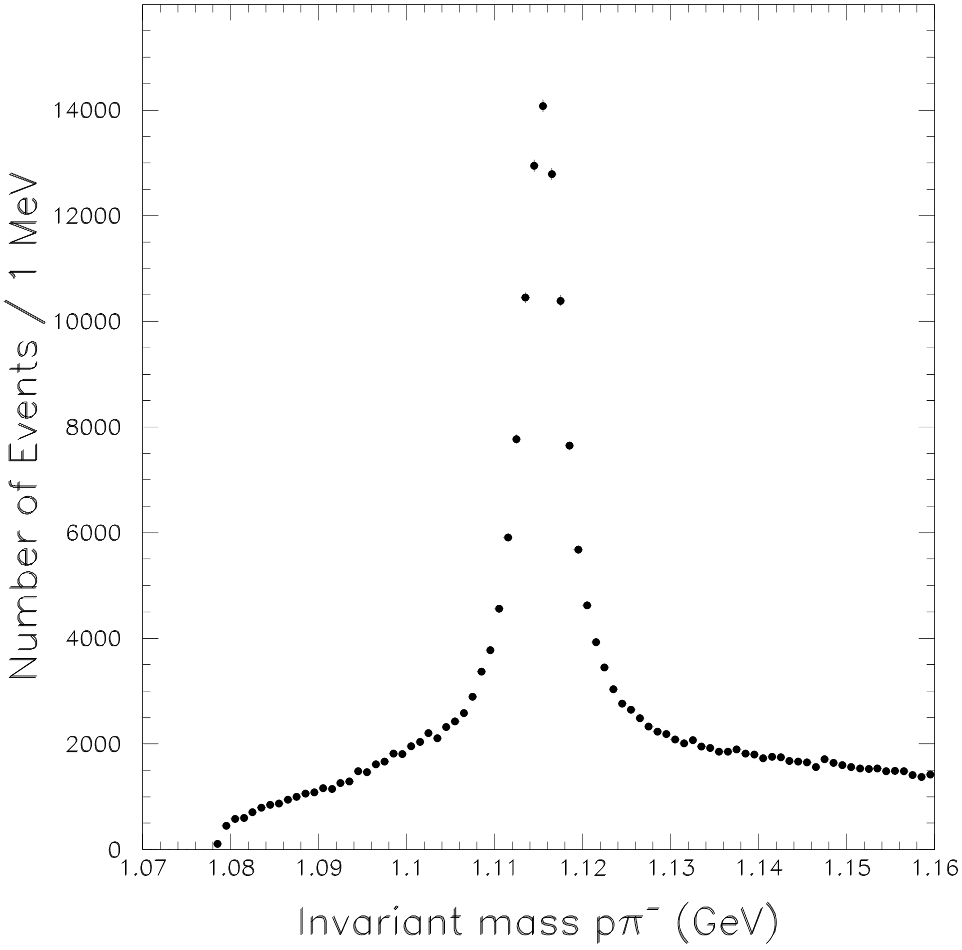

Figure 4.6: Invariant mass $p\pi^-$ for all combinations.

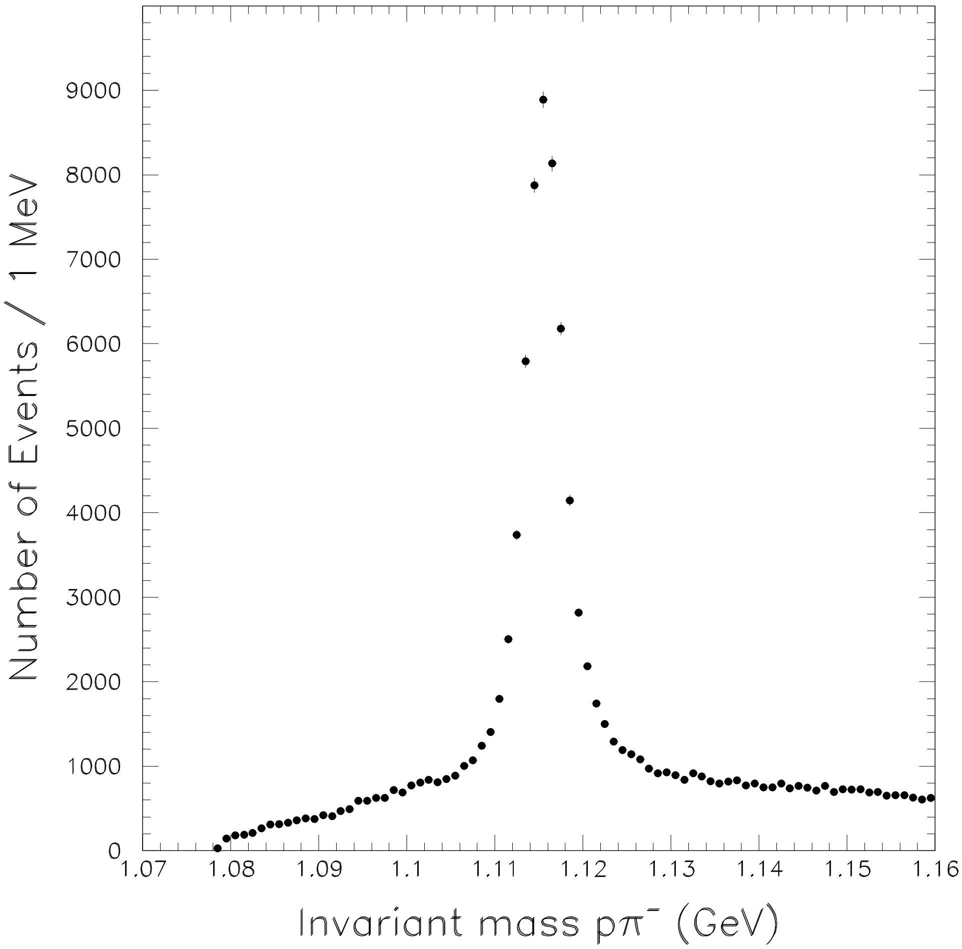

Figure 4.7: Invariant mass pπ^- for combinations in which both tracks have z-chamber hits.

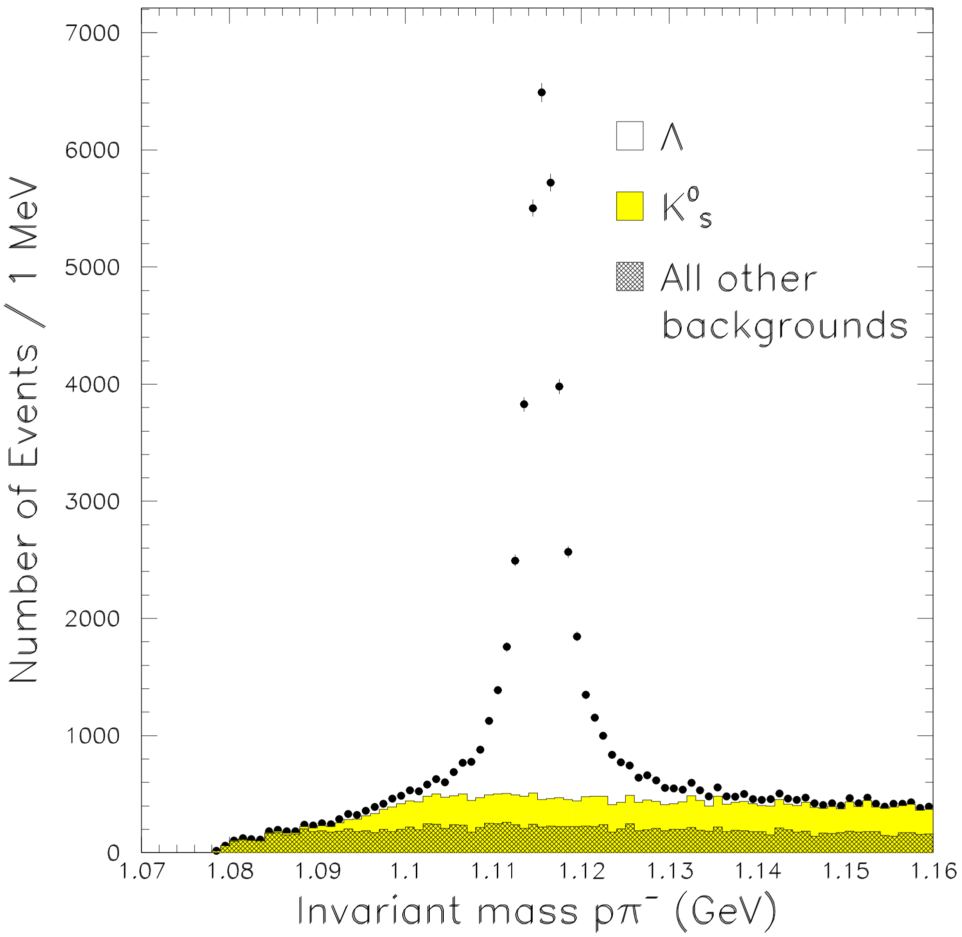

Figure 4.8: Reconstructed Monte Carlo Λ's with backgrounds from K^0_S and all other sources shown.

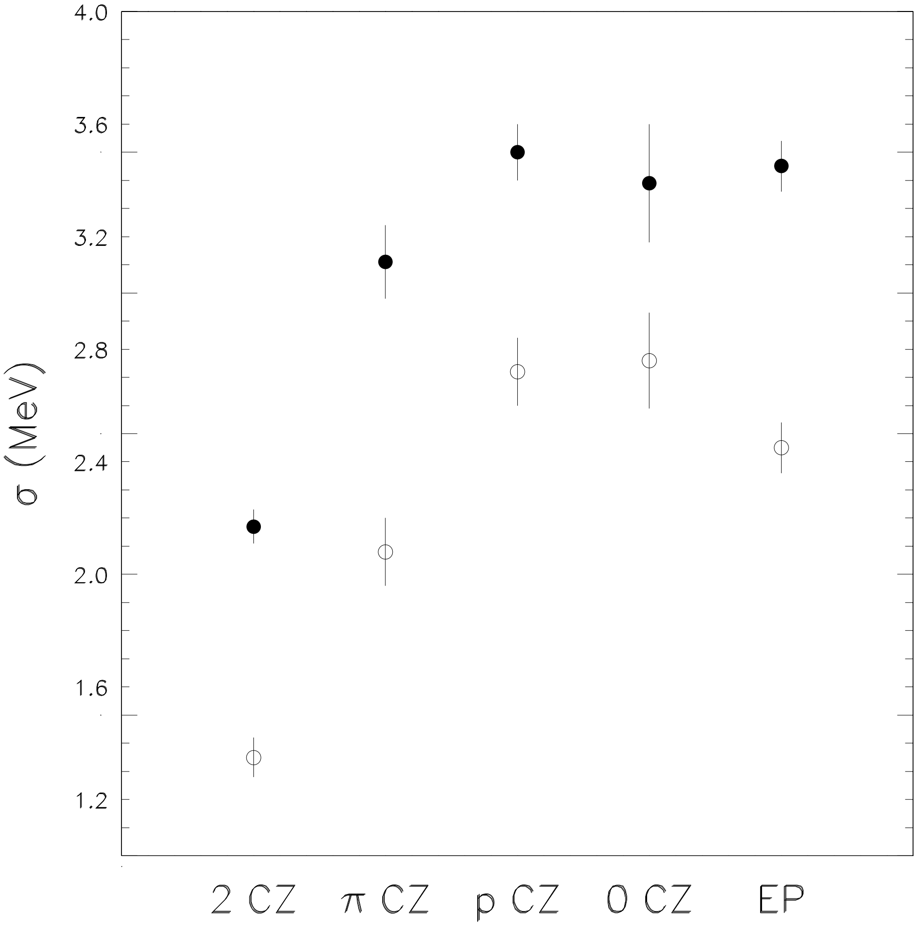

Figure 4.9: The mass resolution in the data (closed circles) and Monte Carlo (open circles) for five different event topologies: (2CZ) both tracks have z-chamber hits, (πCZ) just the π has z-chamber hits, (pCZ) just the proton has z-chamber hits, (0CZ) neither track has z-chamber hits, and (EP) both tracks pass have $|\cos\theta| > 0.72$. In every case, the resolution is about 1.0 MeV worse in the data than in the Monte Carlo.

1115 MeV for $x_p < 0.2$ and ±15 MeV for $x_p \geq 0.2$. (The scaled momentum is defined as $x_p = p_{\mathrm{hadron}}/E_{\mathrm{beam}}$.) The side-bands chosen are the mass intervals from 1090-1110 MeV and 1130-1140 MeV, for all momentum intervals (see figures 4.10-4.12). As can be seen in figure 4.8, the background under the Λ signal is not flat. Therefore, the sideband subtraction method will lead to an underestimate of the background in the signal region. From detailed Monte Carlo studies, it was found that the sideband subtraction method consistently underestimated the background in the signal region by $20 \pm 10\%$ independent of momentum, $\cos\theta$, and the number of z-chamber hits associated with the tracks. Conservatively, a 50% systematic error is assigned to this correction. Using the sideband subtraction method, we find 86383 ± 401 signal events above a background of 40,789 for all accepted combinations, and 49704 ± 284 signal events above a background of 16,782 in the case in which both tracks have at least four associated z-chamber hits.

The detector stability over the three years of data taking was also investigated. In figure 4.13 is plotted the number of $\Lambda(\overline{\Lambda})$ reconstructed per hadronic event as a function of the OPAL running period. The average number reconstructed per event was 0.0696 ± 0.0003 for all years, which agrees quite closely with averages of

- 0.0713 ± 0.0010 for 1990,
- 0.0698 ± 0.0006 for 1991, and
- 0.0692 ± 0.0004 for 1992,

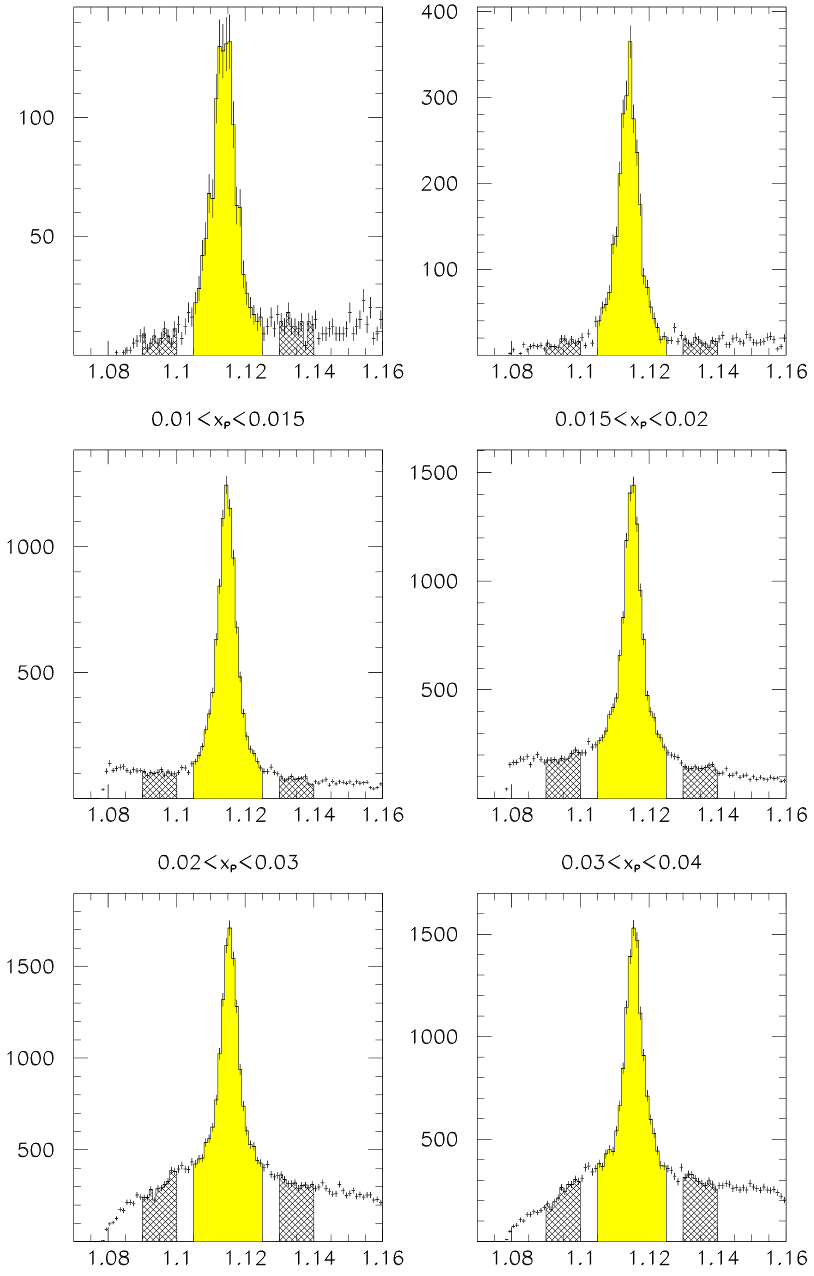

$0.01<x_P<0.015$ $0.015<x_P<0.02$

$0.02<x_P<0.03$ $0.03<x_P<0.04$

$0.04<x_P<0.05$ $0.05<x_P<0.06$

Figure 4.10: Invariant mass $p\pi^-$ for low momentum.

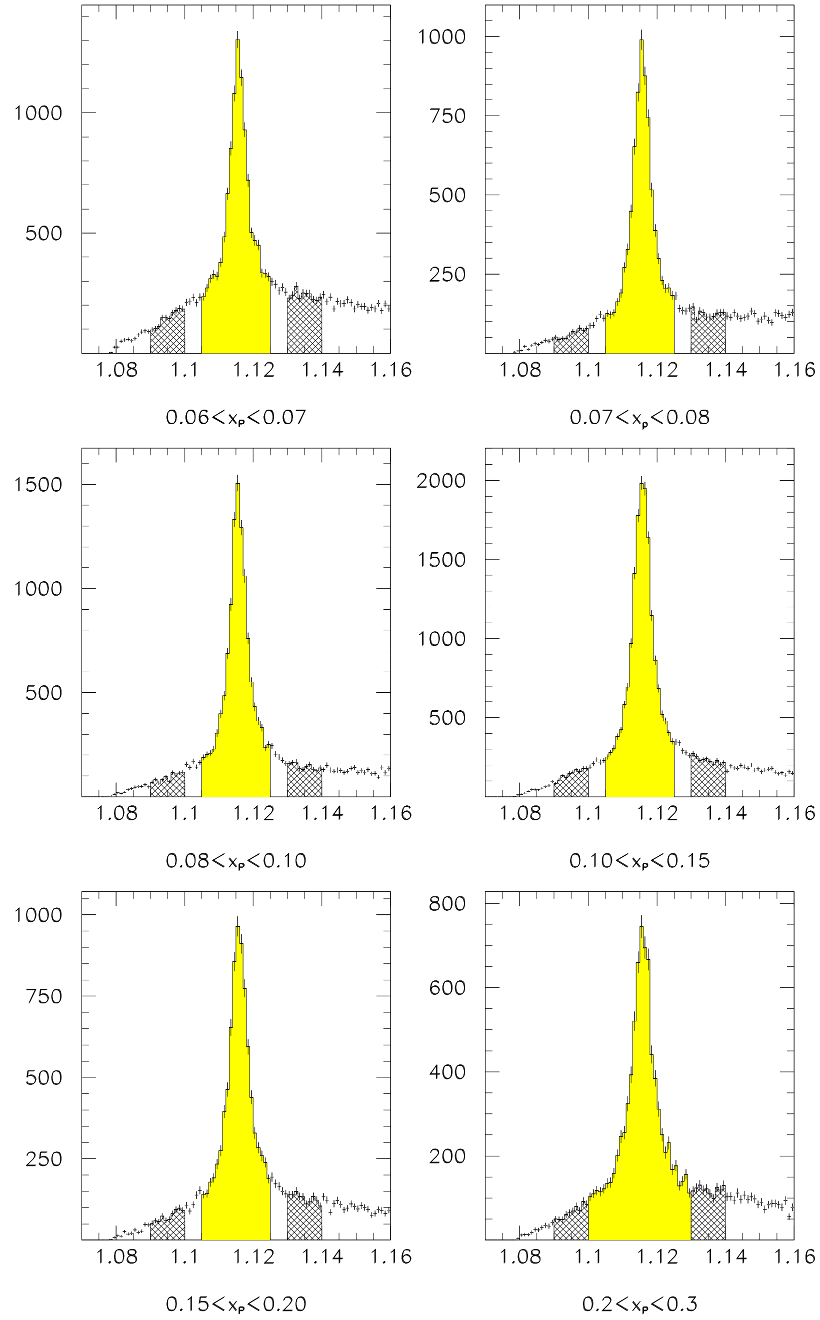

Figure 4.11: Invariant mass $p\pi^-$ for medium momentum.

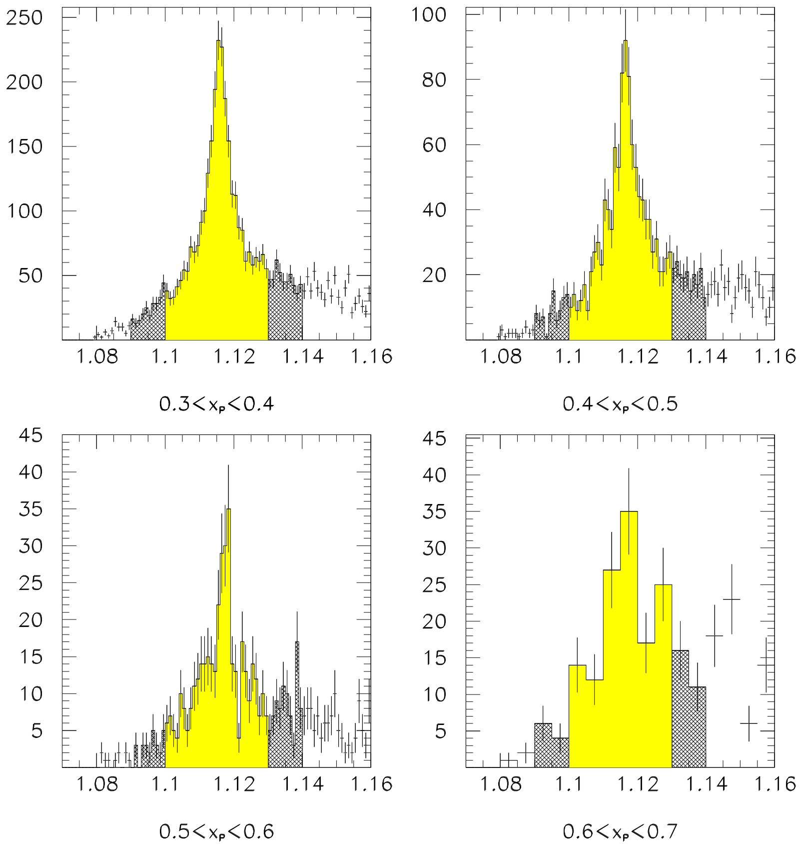

$0.3<x_p<0.4$ $0.4<x_p<0.5$ $0.5<x_p<0.6$ $0.6<x_p<0.7$

Figure 4.12: Invariant mass $p\pi^-$ for high momentum.

where the errors are statistical only.

Signals can be found over a large range of momentum. The signal for different momentum bins for all combinations irrespective of the number of z-chamber hits are shown in figures 4.10 to 4.12. Clear signals are seen up to a scaled momentum of $x_p = 0.7$, which corresponds to an energy of about 32 GeV.

The efficiency is determined from a sample of JETSET Monte Carlo

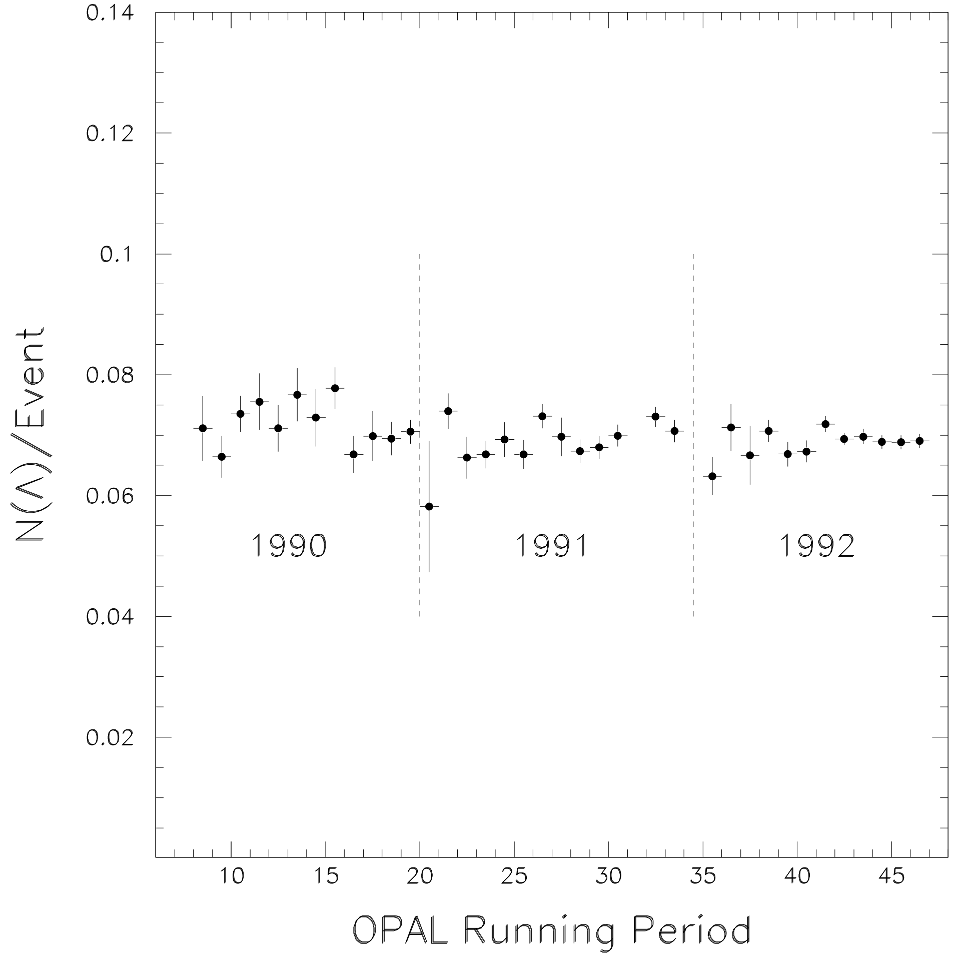

Figure 4.13: Number of $\Lambda(\overline{\Lambda})$ (background subtracted) reconstructed per hadronic event as a function of the OPAL running period.

events with full detector simulation which contain 393,647 $\Lambda(\overline{\Lambda})$ at the generator level. After the full detector simulation of these events, however, the are several systematic differences between the Monte Carlo and the data which affect the calculation of the efficiency.

As shown in figure 4.9, the mass resolution is wider in the data than in the Monte Carlo by about 1.0 MeV, independent of momentum and the number of tracks with 4 or more z-chamber hits. The number of Λ's lost in the tails has been studied with Monte Carlo and has been shown to be proportional to the resolution, and is independent of other factors. For every 1 MeV degradation in the mass resolution, an additional 6.5% of the signal is lost in the tails. A fifty percent systematic error is assigned to this correction, which results in a 3.5% systematic error when one calculates the overall Λ multiplicity.

The z-chamber matching efficiency is also 3-4% lower in the data than in the Monte Carlo (see figure 4.14), independent of $\cos\theta$ but strongly dependent on the transverse momentum of the track at low momentum. This effect increases the disagreement of the mass resolution, so that the efficiency for reconstructing a Λ is reduced by an average additional factor of 0.975 ± 0.025 relative to the Monte Carlo. A conservative systematic error has been assigned to this correction, which results in a systematic error of 3.1% in the multiplicity.

The overall systematic error due to the resolution is therefore 4.7% when all tracks are used to determine the multiplicity, and 3.5% if only those tracks

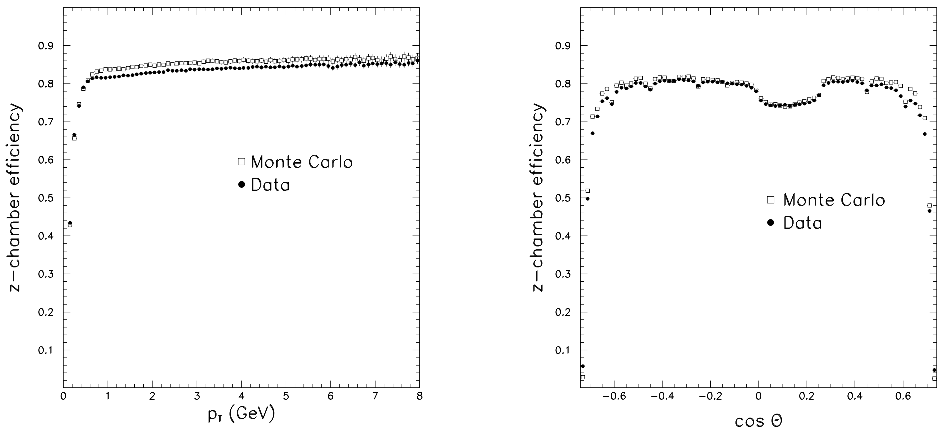

Figure 4.14: z-chamber efficiency as a function of p_t and the $\cos\theta$ of the track.

with more than 4 z-chamber hits are used. For the calculations of the signal as a function of x_p, the corrections for z-chamber matching efficiency differences are carried out for each momentum bin separately, since the efficiency is strongly dependent on momentum at low p_t (see in figure 4.14).

The final corrected efficiency as a function of x_p for reconstructing $\Lambda \rightarrow \mathrm{p}\pi^-$ is shown in figure 4.15 by the solid points. At low momentum the efficiency is reduced by the tracking efficiency, while at high momentum, the efficiency drops off because a larger fraction of Λ's decay outside the central detector volume. The efficiency rises quickly from zero to a maximum of a little over 41% at $x_p = 0.07$, and then slowly drops to about 10% for very high momentum $x_p > 0.6$, for all combinations irrespective of the number of z-chamber hits. If the two tracks are required to have 4 or more z-chamber hits, the efficiency is about a factor of 0.6 lower, as shown by the open points in figure 4.15, although this depends strongly on momentum at very low

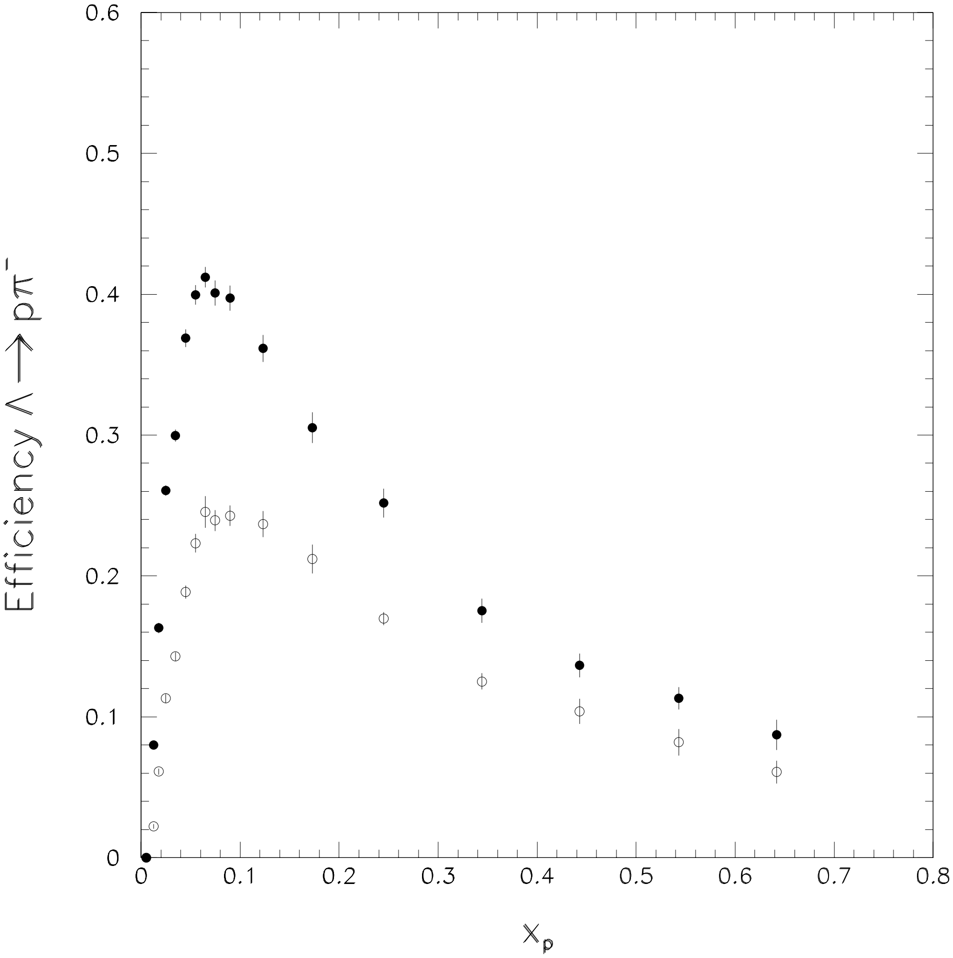

Figure 4.15: The final corrected Λ efficiency for the decay $\Lambda \rightarrow p\pi^-$ as a function of the scaled momentum, x_p, when no requirement is made on the number of z-chamber hits (solid points) and when both tracks are required to have at least 4 z-chamber hits (open points). The errors shown include the Monte Carlo statistical errors and the systematic errors from the z-chamber correction.

values of x_p where the z-chamber efficiency drops off steeply. The factor of 0.6 arises because the maximum of the z-chamber matching efficiency is 81% for a single track in the data, and also from the fact that more Λ signal events are found in the endcap region in the Monte Carlo than in the data.

A summary of the systematic errors is listed in table 4.2. The overall systematic error for the Λ multiplicity is 6.1% when both tracks are required to have more than four z-chamber hits and 7.4% overall.

	Λ (all)	Λ (2CZ)	Ξ^-
Signal Events	86,383	49,704	2464
Background Events	40,789	16,782	1655
Stat. Error	0.5%	0.6%	3.1%
Total Syst. Error	7.4%	6.1%	7.0%
Background Syst.	3.9%	2.8%	2.0%
Cut Simulation	4.0%	4.0%	4.0%
Mass Resolution	4.7%	3.5%	4.0%
Monte Carlo Extrapolation	0.9%	0.9%	2.3%
Monte Carlo Statistical	0.5%	0.7%	2.7%

Table 4.2: Errors in the measurements of the octet baryon multiplicities. Both the statistical errors and the various contributions to the systematic errors are given.

For the subsequent baryon searches, a $p\pi^-$ combination is accepted as a Λ if the reconstructed mass differs from the Λ mass of 1,115.63 MeV (from the Particle Data Group [15]) by less than 10 MeV if $x_E < 0.2$ and 15 MeV otherwise.

4.2 Ξ^- Production

Ξ^- baryons can be identified by their decays into $\Lambda\pi^-$. A third negatively charged track (assumed to be a π^-) is combined with the reconstructed Λ's. The following criteria must hold:

- The $|d_0|$ of the additional pion track must be greater than 150 μm.
- If there are more than 20 dE/dx hits for the additional pion track, the combination is rejected if the pion weight is less than 5% and either the electron or proton weight is greater than 5%.
- An intersection in r-ϕ between the additional track and the Λ must be found on the same side of the event vertex and within a radial range of 1-50 cm.
- The angle Φ for the $\Lambda\pi^-$ combination must be smaller than 30 mrad and $10+20/p_{t(\Xi^-)}$ mrad, where $p_{t(\Xi^-)}$ is the transverse momentum of the Ξ^- candidate.
- The additional track is constrained in θ to come from the assumed Ξ^- decay point. This improves the mass resolution by about 0.5 MeV.

Figure 4.16 shows the Ξ^- signal is observed in the $\Lambda\pi^-$ mass spectrum found with these cuts. The background is determined from the wrong charge combination $\Lambda\pi^+$. Since no "Ξ^+" exists, there should be no peak in the $\Lambda\pi^+$ mass spectrum. Outside of the signal region, this spectrum models the background very well, as can be seen in figure 4.16. This method of

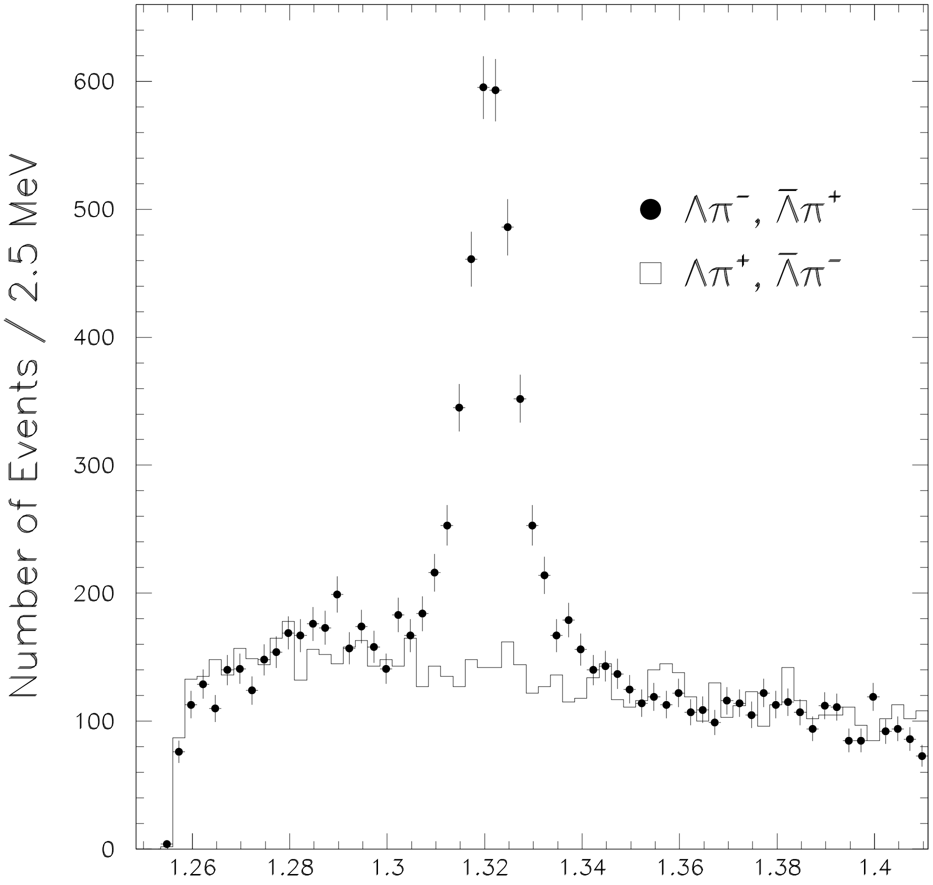

Figure 4.16: Invariant mass $\Lambda\pi^-$.

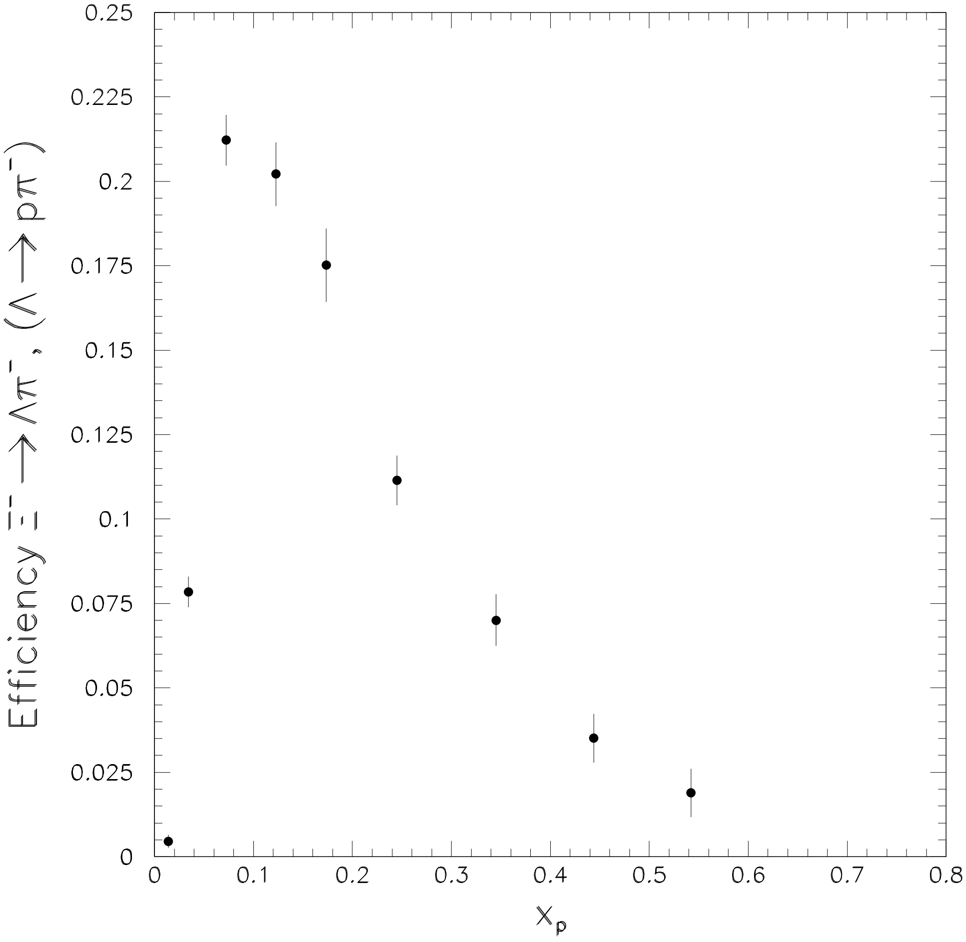

Figure 4.17: The final corrected efficiency for the decay $\Xi^- \rightarrow \Lambda\pi^-$, with $\Lambda \rightarrow p\pi^-$, as a function of the scaled momentum x_p.

estimating the background has been checked with the Monte Carlo and is found give the same answer to within a 2% systematic error.

In the signal region of ±15 MeV around the Ξ^- mass of 1,321.32 MeV, we find 2464 ± 76 signal events above a background of 1655 events. In our previous publication [7], the signal region was taken as ±10 MeV, in contrast to the present analysis. The signal region has been optimized to give a good signal to background ratio as well as a high efficiency. Almost 90% of the signal in Monte Carlo events fall within the signal region, while the rest are spread out in long non-Gaussian tails. The mass resolution is about 4.8 MeV, and is consistent for the data samples from different years.

Approximately equal numbers of baryons and anti-baryons (1207 ± 54 and 1257 ± 54, respectively) are found. An excess in the number of baryons relative to anti-baryons, as reported by other experiments at lower energies, is not confirmed [44].

The efficiency from Monte Carlo must be corrected for both the Λ corrections and the z-chamber matching efficiency. An overall factor of 0.935 ± 0.0375 is assigned for the Λ and Monte Carlo mass resolution corrections. The systematic uncertainties, many of which are common to both the Λ and Ξ^- analyses, are summarized in table 4.2. The efficiency as a function of the scaled momentum is shown in figure 4.17.

4.3 Ω^- Production

The Ω^- decays predominantly into ΛK^- with 67.8% branching ratio. Since this decay is geometrically equivalent to that of Ξ^- decay, the cuts are very similar. However, the cross section for $\Omega^- \rightarrow \Lambda K^-$ is low and the backgrounds are large relative to the signal. Consequently, the cuts have been changed to identify the small number of K^- in the presence of a large π^- background.

The kaon track must have a p_t greater than 200 MeV, whereas the cut for the Ξ^- search is only 100 MeV. This helps eliminate some of the low energy pion background. In addition, the dE/dx cuts are completely different. Since the number of kaon tracks is a small proportion of the total number of tracks, positive particle identification rather than background rejection is necessary. If the kaon track has fewer than 20 dE/dx hits, it is rejected. If the momentum is in the dE/dx cross-over region of the kaon band and the pion band (see figure 4.2) between 900 MeV and 1.5 GeV, the track is rejected. For kaons with a momentum below 900 MeV, the kaon weight must be greater than 5% and the dE/dx greater than 7.5 keV/cm. For kaons with a momentum greater than 1.5 GeV, the kaon weight must be greater than 5% and also greater than the pion weight. Finally, the probability in r-ϕ for the Ω^- to survive without decaying, $e^{-m_\Omega/p_t \cdot r/c\tau}$, must be greater than 5% and smaller than 95%. Here $c\tau$ is the decay length of the Ω^-, which is taken to be 2.46 cm [15].

With these cuts, an Ω^- signal is observed in the ΛK^- mass spectrum (see figure 4.18). As in the case of the Ξ^-, the background is determined from the

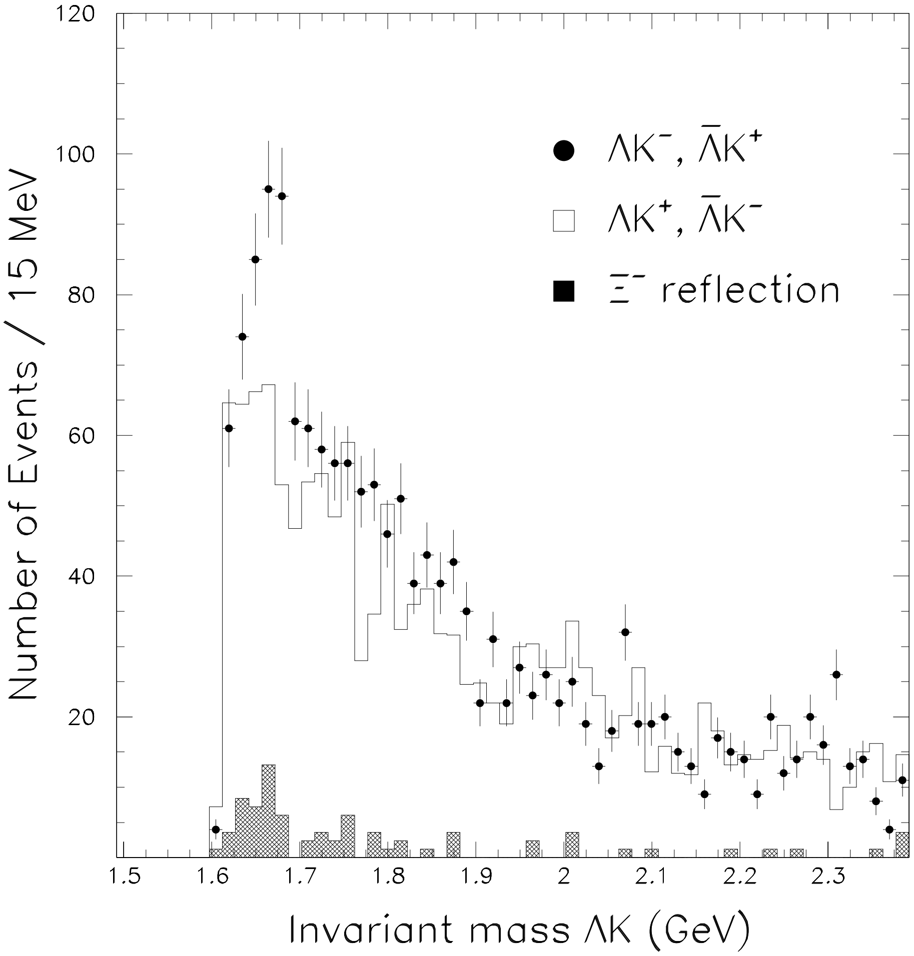

Figure 4.18: Invariant mass ΛK^-. The background is the excess in the Ξ^- mass region of the $\Lambda\pi^-$ mass spectrum (shaded) and the wrong charge combination added to it (histogram).

wrong charge combination ΛK^+. In addition we must take into account the reflection of the Ξ^- signal in the ΛK^- mass spectrum. The ΛK^- mass of the small excess in the Ξ^- signal region is added to the wrong charge combination background. The resulting total background is plotted in figure 4.18. A total of 102 ± 24 signal events are found above a background of 234 events in the four 15 MeV bins around the Ω^- mass of 1672 MeV.

The mass resolution for the Ω^- in the latest re-processed data sample is a factor of two worse than in the data samples from the publication. Although the same data is used for 1990 and 1991, the re-processing with a later version of ROPE appears to have degraded the resolution of Ω^-, while leaving the resolution of Ξ^- unchanged. This motivated the use of a larger signal region compared with our previously published studies, but no reasonable explanation for the difference was found. Studies of the mass resolution in θ, the dE/dx resolution for charged kaons, the z-chamber efficiency, and other searches for a cause of this difference produced no explanation. One can also see that in figure 4.18 the agreement between the two different charge combinations is quite bad, but only near the Ω^- signal region. For the mass region $m_{\Lambda K} >$1900 MeV the agreement is quite good. This leads us to believe that events which are true Ω^-'s are being reconstructed with masses in a long non-Gaussian tail, although the reason for such a problem is unknown. We will assume that we are losing an extra 20% of the events in the tails for some unknown reason, and factor in a correction of 1.2 in the cross section calculation. A 100% systematic error is assigned to this correction, which gives a 25% component to the systematic error for the mass resolution. This is the largest component of the total systematic error (see table 4.3).

To calculate the Ω^- efficiency, a special sample of 3,000 JETSET events with an Ω^- at the tree level was generated with the full detector simulation. The mass resolution of the Ω^- is about 10 MeV in the Monte Carlo (see figure 4.19), which is consistent with the resolution in the earlier data sample from 1990 and 1991 used in the publication [7]. The efficiency integrated over all observable momentum bins is $5.67 \pm 0.41\%$, for the decay sequence $\Omega^- \rightarrow \Lambda K^-$, $\Lambda \rightarrow p\pi^-$. Included is a correction factor of 0.935 ± 0.0375, as in the case of the Ξ^-, which takes into account the corrections necessary for the Λ efficiency.

	Ω^-	$\Sigma(1385)^\pm$	$\Xi(1530)^0$
Signal Events	103	4,745	279
Background Events	233	82,270	630
Stat. Error	23.3%	8.7%	13.9%
Total Syst. Error	27.7%	10.4%	12.3%
Background Syst.	5.0%	5.0%	5.0%
Cut Simulation	5.0%	5.0%	5.0%
Mass Resolution	25.3%	7.4%	4.0%
Monte Carlo Extrapolation	5.0%	1.5%	5.0%
Monte Carlo Statistical	7.2%	1.3%	7.7%

Table 4.3: Errors in the measurements of the decuplet baryon multiplicities. Both the statistical errors and the various contributions to the systematic errors are given.

The small number of events does not allow a more detailed study of the systematics, although small variations in the dE/dx and other cuts resulted in no significant change in the Ω^- signal. The systematic errors are summarized

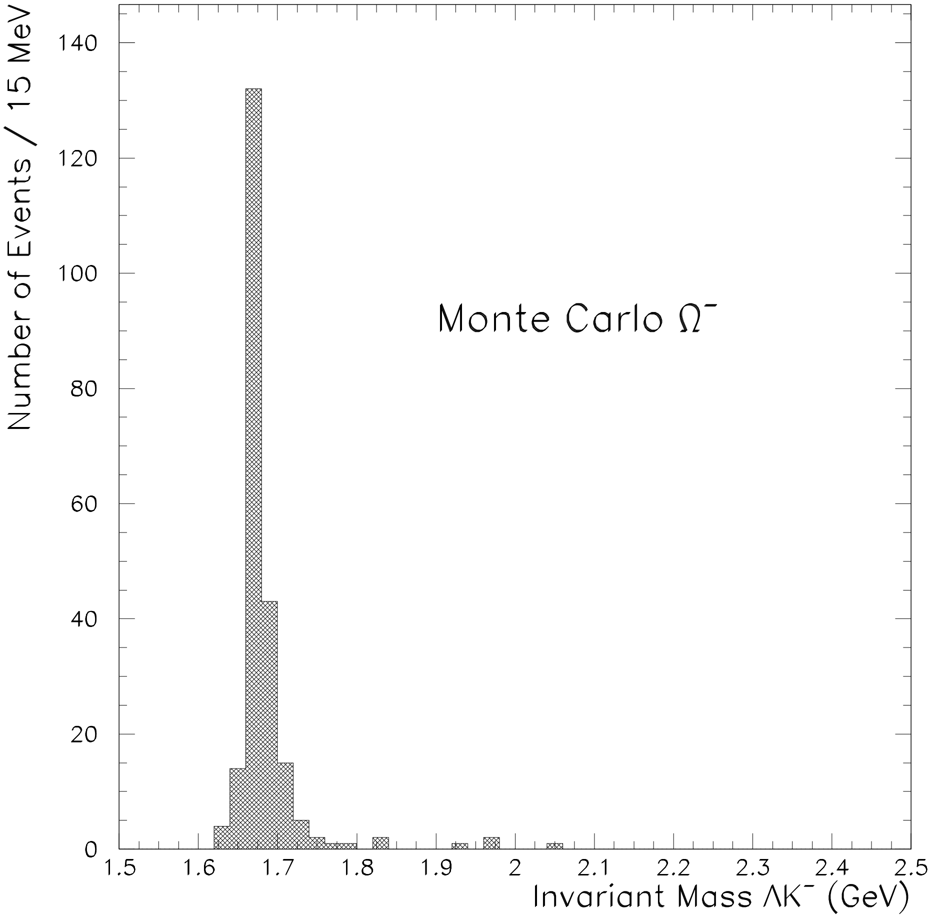

Figure 4.19: Invariant mass ΛK^- from reconstructed Monte Carlo Ω^-.

in table 4.3.

4.4 $\Sigma(1385)^{\pm}$ Production

$\Sigma(1385)^{\pm}$ baryons can be identified by their prompt decays into $\Lambda\pi^{\pm}$. Since this resonance decays at the event vertex, the additional pion track is required to have a small impact parameter with the event vertex, $|d_0| < 2$ mm. The dE/dx cuts used here are the same as for the charged pion in the Ξ^- search. With these two cuts, broad $\Sigma(1385)^{\pm}$ signals are seen in the $\Lambda\pi^{\pm}$ mass spectra (see figures 4.20 and 4.21). In figure 4.21, one can also see the residual Ξ^- peak, while no such mass peak is observed in the other charge combination.

The backgrounds have been determined by a fit to the background shape. We fit the background to a function $(1. - e^{-a(x-1.25)}) \times (bx^2 + cx)$, with a Breit-Wigner resonance for the $\Sigma(1385)^{\pm}$ signal, and a Gaussian for the Ξ^-. The upper range of the fit is set to an invariant mass of 1.8 GeV. The centroids and widths of the peaks are free parameters in the fit, as well as the three parameters of the background function. This method gives the correct number of signal events to within $\pm 5\%$ in Monte Carlo studies.

The result from the fit gives the number of $\Sigma(1385)^{\pm}$ signal events as 4745 ± 411 over a background of 82270 in the signal region of ± 40 MeV around the $\Sigma(1385)^{\pm}$ mass. Fitting over different intervals and with different background functions also yields answers to within $\pm 5\%$ of the mean value.

Another method, in which one determines the background shape by using $p\pi^-$ combinations found outside the Λ signal region, assumed to have the

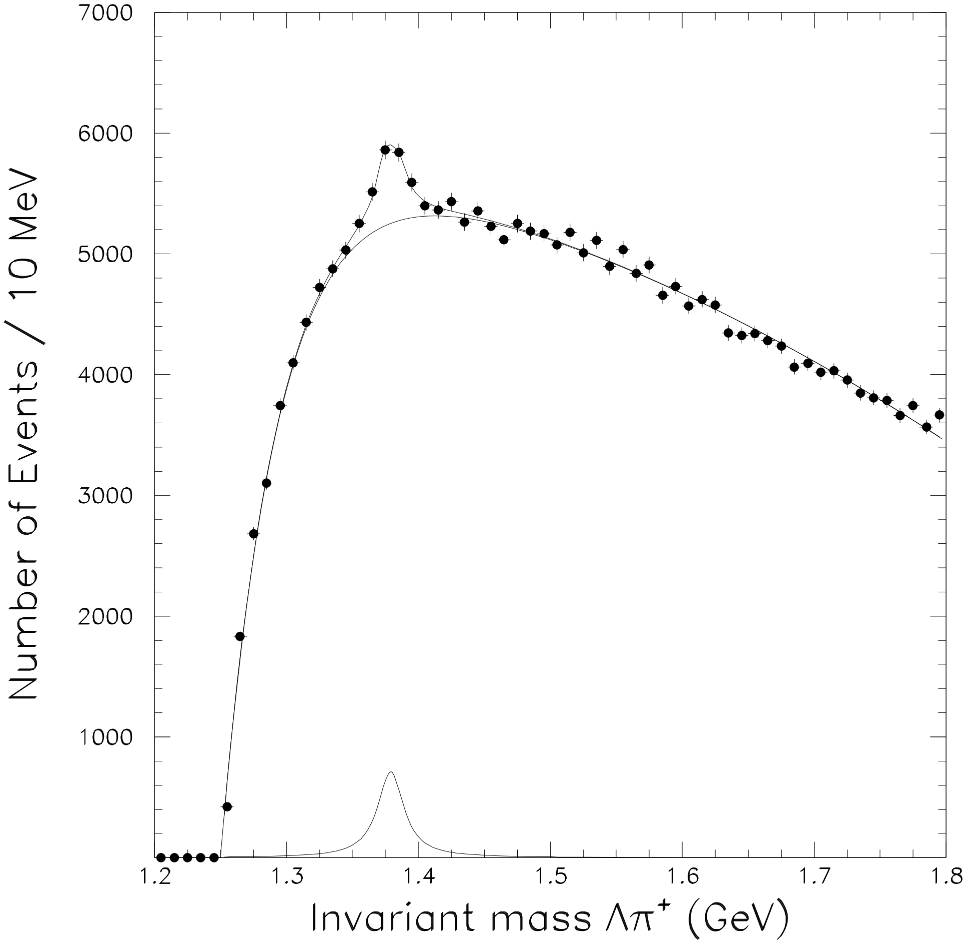

Figure 4.20: Invariant mass $\Lambda\pi^+$.

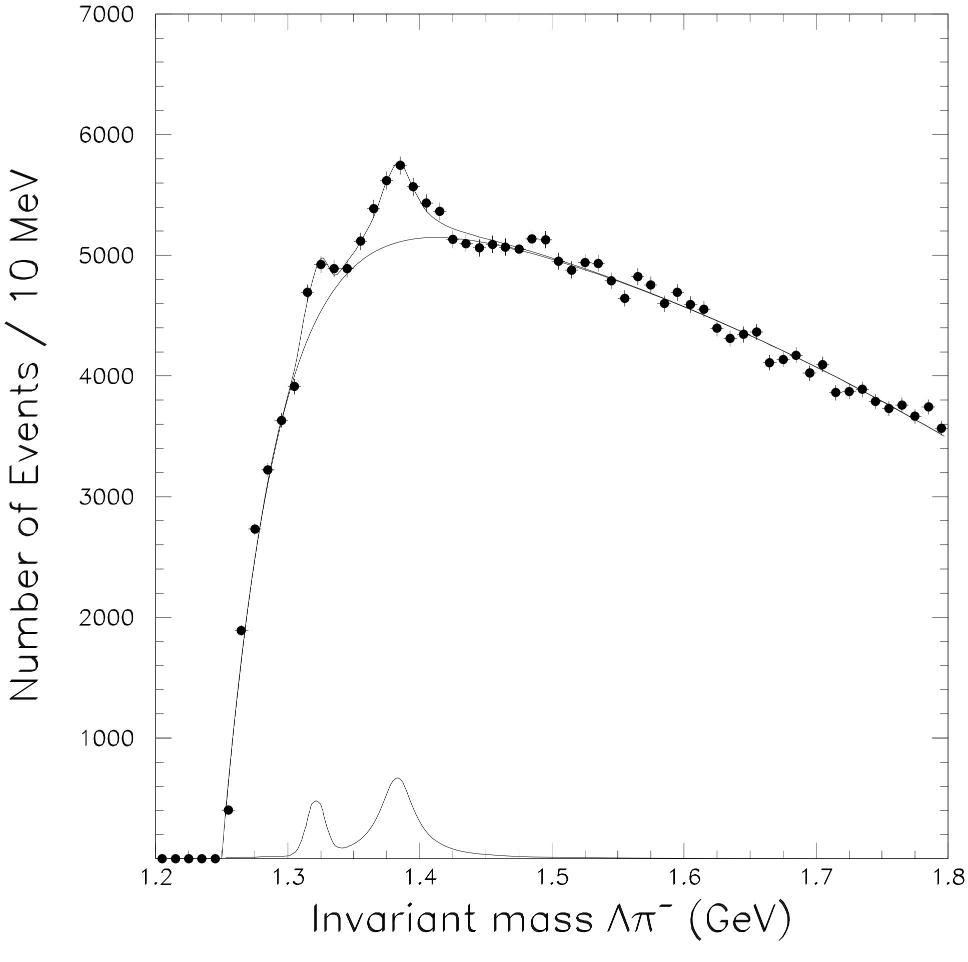

Figure 4.21: Invariant mass $\Lambda\pi^-$.

Λ mass, combined with additional tracks, assumed to be pions, results in a systematically high background and underestimates the signal by about 10%. The fit of background shape is particularly bad in this case.

The signals for $\Sigma(1385)^+$ and $\Sigma(1385)^-$ have been calculated separately, where we find 2171 ± 292 $\Sigma(1385)^+$ and 2574 ± 289 $\Sigma(1385)^-$, over backgrounds of 41680 and 40590, respectively. The excess of $\Sigma(1385)^-$ over $\Sigma(1385)^+$ is 403 ± 410 (stat), which is consistent with zero.

The efficiency for the decay sequence $\Sigma(1385)^\pm \rightarrow \Lambda\pi^\pm$, $\Lambda \rightarrow p\pi^-$, has been calculated and is shown in figure 4.22. Included is a correction for the tails of the Breit-Wigner mass distribution which lie outside the signal region of ± 40 MeV. It is estimated that $20 \pm 5\%$ of the signal is found outside of the signal region in the tails of the Breit-Wigner distribution. This correction can not be calculated directly from Monte Carlo because JETSET has a cutoff at ± 35 MeV in the Breit-Wigner which describes the $\Sigma(1385)^\pm$ [45]. A systematic error of ±5% is assigned to this correction. Furthermore, there is a usual correction factor of 0.935 ± 0.0375 for the Λ mass resolution corrections.

4.5 $\Xi(1530)^0$ Production

$\Xi(1530)^0$ baryons can be identified by their prompt decays into $\Xi^-\pi^+$. Ξ^- candidates found in the Ξ^- signal region as defined above are combined with all other oppositely charged tracks, assumed to be pions. The cuts on the additional pion track are identical to those in the case of the $\Sigma(1385)^\pm$. A $\Xi(1530)^0$ mass peak centered on 1532 MeV is seen in the $\Xi^-\pi^+$ mass spectrum

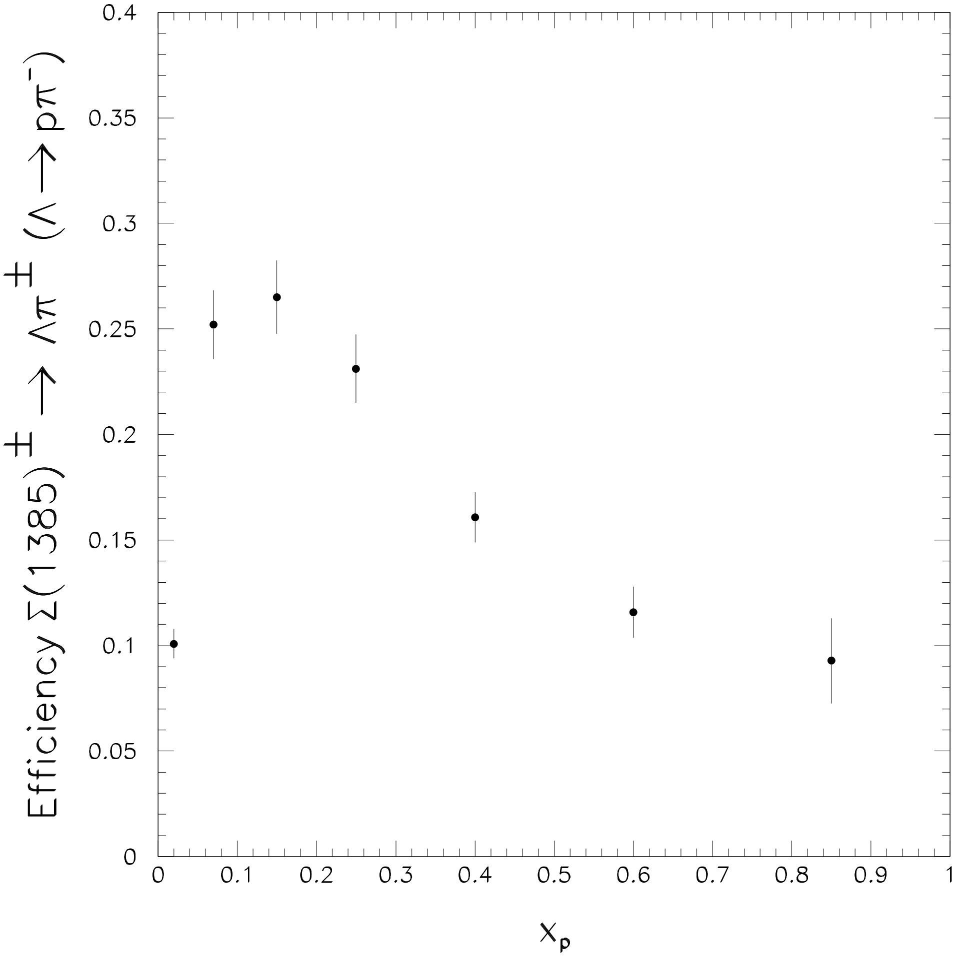

Figure 4.22: Efficiency for reconstructing $\Sigma(1385)^{\pm} \rightarrow \Lambda\pi^{\pm}$, with $\Lambda \rightarrow p\pi^{-}$.

(see figure 4.23).

The background is determined by a fit, in a similar way as the $\Sigma(1385)^{\pm}$ background. The background function chosen was $(1. - e^{-a(x-1.461)}) \times (bx + c)$, with a Gaussian for the $\Xi(1530)^0$ peak. The fit interval was varied and the resulting background level was stable to within 3% (see figure 4.23). This determination of the background gives the correct answer for the number of Monte Carlo signal events to within a ±5% systematic error.

We find 279 ± 39 $\Xi(1530)^0$ signal events above a background of 630, in a signal region from 1510 to 1550 MeV. The background and acceptance are higher than in our previous publication because of the Ξ^- signal region has been increased. The systematic errors are summarized in table 4.3.

The integrated efficiency was calculated to be $7.21 \pm 0.55\%$ from a sample of Monte Carlo events with full detector simulation which contained 5150 $\Xi(1530)^0$ at the generator level. The mass resolution in the data ($\Gamma = 8.7 \pm 0.5$ MeV) was found to be consistent with the world average ($\Gamma = 9.1 \pm 0.5$ MeV) [15] and is also well described by the JETSET Monte Carlo with full detector simulation. The usual correction for the Λ mass resolution corrections has also been applied to calculate the efficiency.

4.6 Cross Sections

The differential cross sections, $1/N_{\text{events}} dn/dx$, have been calculated as a function of the scaled momentum $x_p = p_{\text{hadron}}/E_{\text{beam}}$ and the scaled energy $x_E = E_{\text{hadron}}/E_{\text{beam}}$ for the five baryon types. The Λ cross sections have been

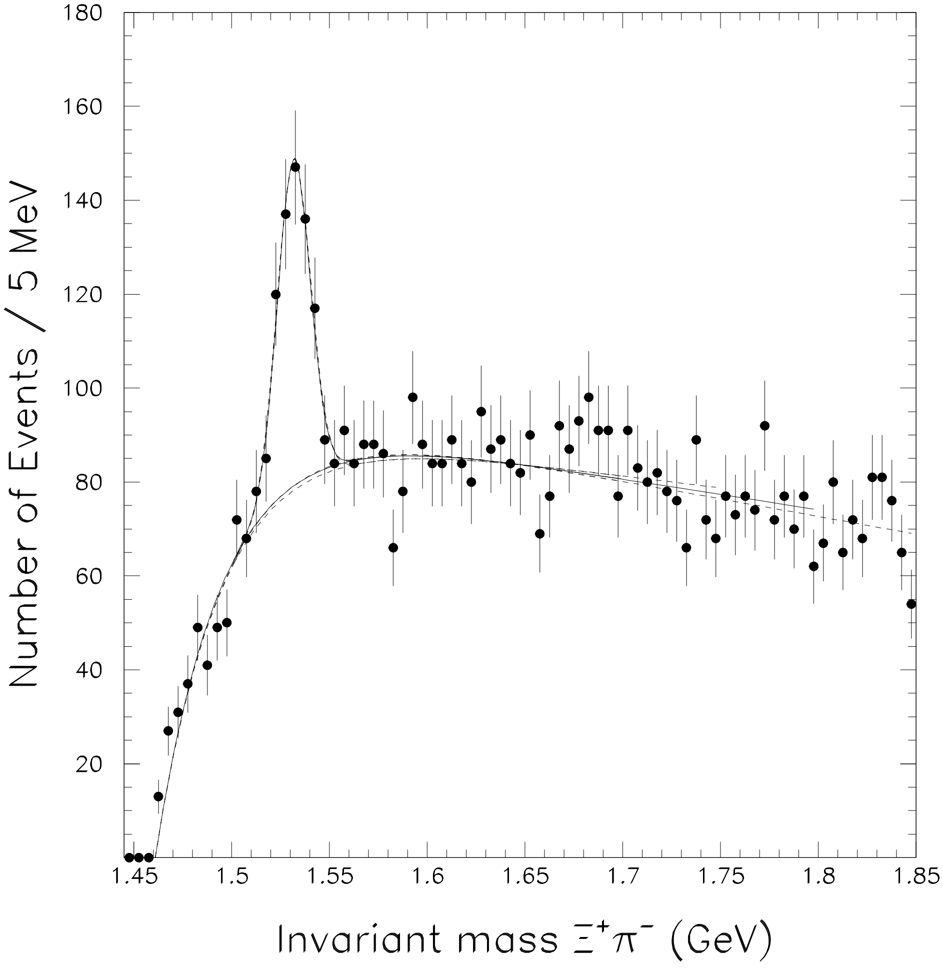

Figure 4.23: Invariant mass $\Xi^-\pi^+$.

calculated separately, using all track combinations and just those with four or more z-chamber hits. As can be seen from tables 4.4 and 4.5, the cross sections agree well over the entire momentum range.

The differential cross sections are plotted in figures 4.24 and 4.25 along with the cross sections from JETSET normalized to the total rate found in the data. Similar and slightly harder fragmentation functions are predicted by the HERWIG Monte Carlo. Above x_E=0.15, the cross sections are up to a factor of two higher in the JETSET Monte Carlo than in the data. This phenomenon has also been reported in the cross sections of the strange mesons $\mathrm{K}^*(892)^0$ and $\phi(1020)$ at a center-of-mass energy $\sqrt{s} = m_{\mathrm{Z}^0}$ [46], and at lower energies [4, 5]. Some indication that the cross sections of $\mathrm{K}^\pm$ and K^0_S are harder than predicted by the Monte Carlos has also been observed, although the results are preliminary [42, 47].

The integrated cross sections for Λ, Ξ^-, and $\Sigma(1385)^\pm$ can be obtained by summing over the observed energy ranges and extrapolating to the unobserved energy ranges using the Monte Carlo. The fraction of baryons found in the unobserved momentum ranges in JETSET is $3.7 \pm 0.9\%$ for the Λ, $9.1 \pm 2.3\%$ for the Ξ^-, and $6.0 \pm 1.5\%$ for the $\Sigma(1385)^\pm$, where the errors are the systematic uncertainties from the shapes of the differential cross sections, which we believe are too hard in JETSET. The following total yields per hadronic Z^0 decay are obtained:

- $\Lambda(\overline{\Lambda})$/event $= 0.363 \pm 0.002$ (stat) ± 0.022 (syst)
- $\Xi^-(\overline{\Xi}^+)$/event $= 0.0240 \pm 0.0007$ (stat) ± 0.0017 (syst)

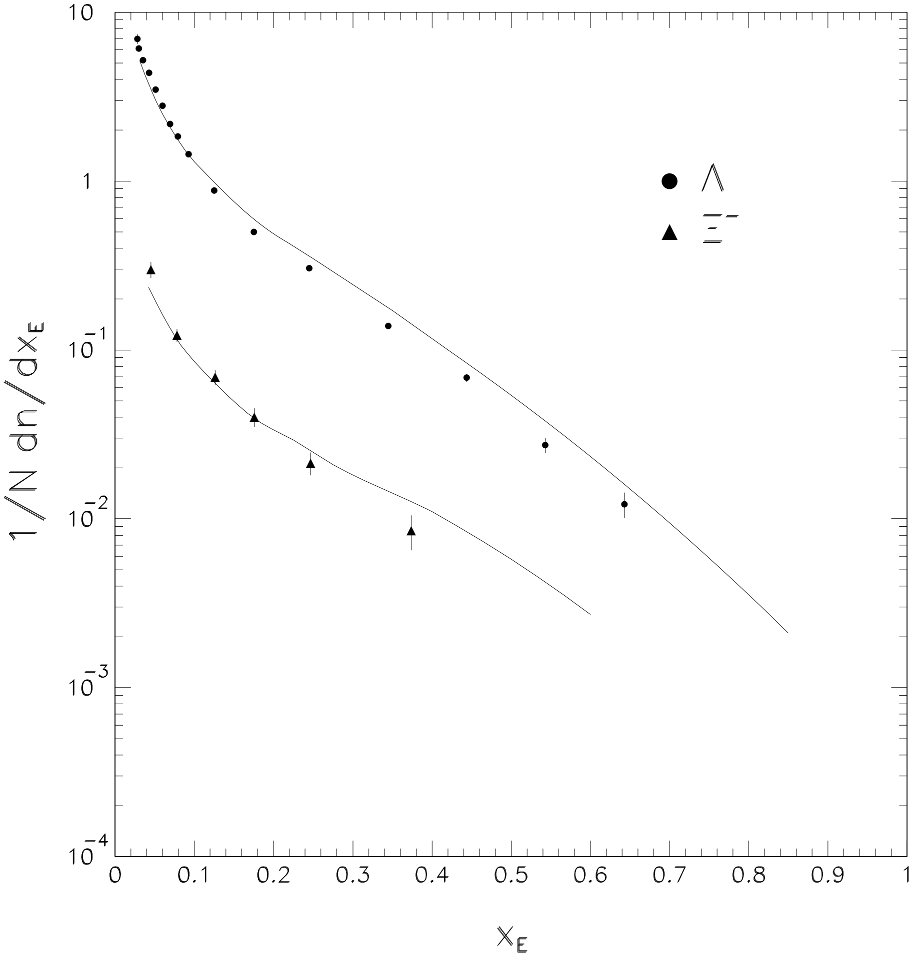

Figure 4.24: Differential cross sections $\frac{1}{N_{\text{had}}}\frac{dn}{dx_E}$ for Λ and Ξ^-. The curves are the cross sections from JETSET, normalized to the observed yield.

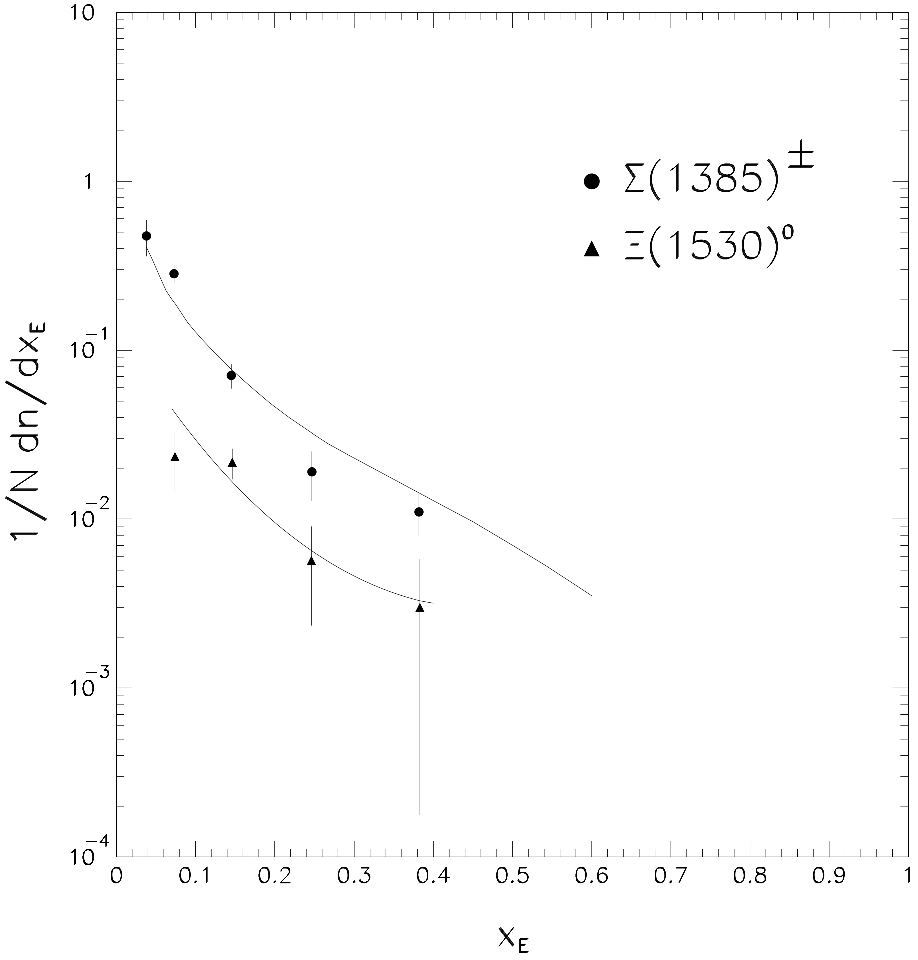

Figure 4.25: Differential cross sections $\frac{1}{N_{had}}\frac{dn}{dx_E}$ for $\Sigma(1385)^{\pm}$ and $\Xi(1530)^0$. The curves are the cross sections from JETSET, normalized to the observed yield.

- $\Sigma(1385)^{\pm}(\overline{\Sigma}(1385)^{\pm})$/event $= 0.0372 \pm 0.0032$ (stat) ± 0.0039 (syst)

These values can be compared with rates from the OPAL publication based on only the 1990 and 1991 data:

- $\Lambda(\overline{\Lambda})$/event $= 0.351 \pm 0.003$ (stat) ± 0.019 (syst)
- $\Xi^{-}(\overline{\Xi}^{+})$/event $= 0.0206 \pm 0.0011$ (stat) ± 0.0019 (syst)
- $\Sigma(1385)^{\pm}(\overline{\Sigma}(1385)^{\pm})$/event $= 0.0380 \pm 0.0038$ (stat) ± 0.0049 (syst)

The total Λ and $\Sigma(1385)^{\pm}$ rates are within one standard deviation of the previously published rates in [7], and the Ξ^{-} rate is about one and a half standard deviations higher. A detailed comparison of the differential cross sections for the Λ from [7] and the present work found excellent agreement over the entire momentum range.

For the other decuplet baryons, due to lower statistics and larger systematic errors on the differential cross sections, the total efficiency integrated over all momentum bins is used to determine the total rate per hadronic event. The systematic error for this method is assigned to be 5%, since one must assume that the shape of the differential cross section is well described by the Monte Carlo, while we know that for the other strange baryons there is some disagreement.

We obtain the following decuplet baryon yields:

- $\Xi(1530)^{0}(\overline{\Xi}(1530)^{0})$/event $= 0.0072 \pm 0.0010$ (stat) ± 0.0009 (syst)

- $\Omega^-(\overline{\Omega}^+)$/event = 0.0033 ± 0.0008 (stat) ±0.0009 (syst)

One can compare these values to the OPAL published rates:

- $\Xi(1530)^0(\overline{\Xi}(1530)^0)$/event = 0.0063 ± 0.0010 (stat) ±0.0010 (syst)
- $\Omega^-(\overline{\Omega}^+)$/event = 0.0050 ± 0.0012 (stat) ±0.0009 (syst)

Both values obtained with the inclusion of the 1992 data sample are within one standard deviation of the previously published values. The results of all of the measured inclusive strange baryon rates are summarized in table 4.9.

Some correlated systematic errors (such as the Λ mass resolution corrections) cancel in ratios of inclusive cross sections. Several ratios, given below, are useful in comparing the data with various Monte Carlo models:

- $\Xi^-/\Lambda = 0.066 \pm 0.005$
- $\Xi(1530)^0/\Sigma(1385)^\pm = 0.194 \pm 0.043$
- $\Omega^-/\Xi(1530)^0 = 0.46 \pm 0.18$

The errors are combinations of both the statistical and systematic errors, correlated errors having been neglected.

4.7 Other Strange Baryon Searches

Several strange baryons undergo decays into final states containing photons, such as $\Sigma^0 \to \Lambda\gamma$, $\Xi^0 \to \Lambda\pi^0$, and $\Sigma^+ \to p\pi^0$, where the $\pi^0 \to \gamma\gamma$. Photons from strange baryon decays, however, have energies that are on the order of a few GeV. An attempt has been made to reconstruct these decays using isolated clusters in the barrel region of the electromagnetic calorimeter.

To reconstruct π^0's, all pairs of electromagnetic clusters with no associated charged track in the central detector are combined. The following cuts are made on the clusters:

- The raw energy of the cluster must be at least 500 MeV.
- The cluster must be in the barrel, where the energy resolution is best, with $|\cos\theta| < 0.72$.
- The cluster must be isolated from all charged tracks by at least 5°.
- The angle θ^* between the photon direction in the π^0 rest frame and the π^0 flight direction must satisfy $|\cos\theta^*| < 0.98$.
- The presampler multiplicity in a $4^\circ \times 4^\circ$ area around the electromagnetic cluster must be less than 10. This requirement that the photon not shower significantly before reaching the calorimeter means that the raw calorimeter energy will be a good measurement of the photon energy.

With these cuts a narrow π^0 peak is seen in the $\gamma\gamma$ mass spectrum, as shown in figure 4.26. The background was fitted to a second order polynomial over the mass interval 30-300 MeV, and the peak was fitted to a Gaussian, where the signal region was taken to be ± 50 MeV around the π^0 mass of 135 MeV [15]. The estimated systematic error in the background determination is $\pm 10\%$.

There are 84008 ± 494 π^0's in the signal region, above a background of about 80000. The efficiency for reconstructing $\pi^0 \rightarrow \gamma\gamma$ has been studied in the Monte Carlo and was found to be $0.75 \pm 0.07\%$. We find the following π^0 yield per hadronic Z^0 decay:

- π^0/event $= 9.9 \pm 0.2$ (stat) ± 1.4 (syst)

The systematic error is made up of ±10% from the background determination and ±10% from the Monte Carlo determination of the efficiency, where we have extrapolated into the unobserved momentum regions. The range of sensitivity of reconstructing π^0's is 1 GeV $< E_{\pi^0} <$ 4 GeV. Above 4 GeV the angular separation of the two photons is too small for the electromagnetic calorimeter to resolve. Included in this rate are π^0 of all energies and π^0 from secondary decays of heavier states. This result agrees with the multiplicity in JETSET of 9.86 π^0 per event and the value determined by the L3 experiment [48].

Searches for $\Xi^0 \rightarrow \Lambda\pi^0$ and $\Sigma^+ \rightarrow p\pi^0$ using the reconstructed π^0's has turned up no positive signals (see figure 4.27), which is consistent with the very low π^0 efficiency. Searches for the $\Sigma^0 \rightarrow \Lambda\gamma$ have also given a null result, because of low efficiency and poor photon energy resolution at low energies (see figure 4.28). Searches which try to reconstruct the decay $\gamma \rightarrow e^+e^-$ also suffer from the same problem of very low efficiency due to the low probability of photons to convert in the OPAL beam pipe.

A search for additional Ξ resonances and the Ξ_C^0 was also carried out. Since the number of known Ξ resonances is relatively small compared with

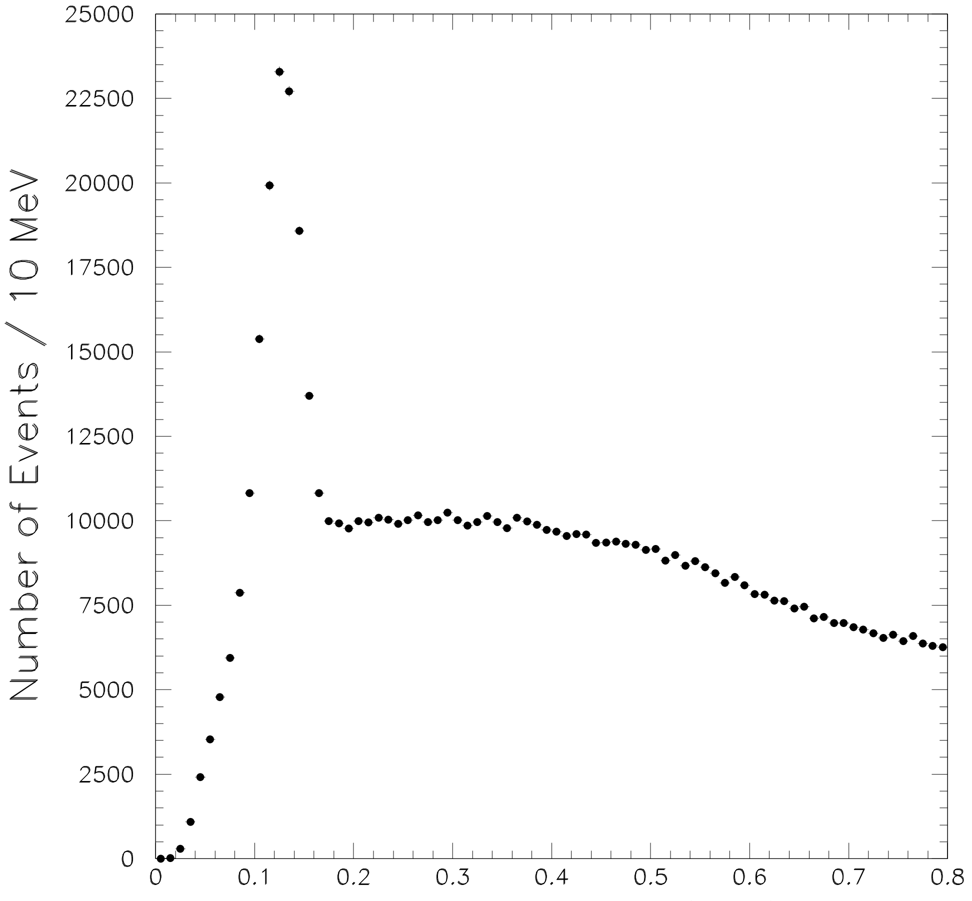

Figure 4.26: Invariant mass of $\gamma\gamma$.

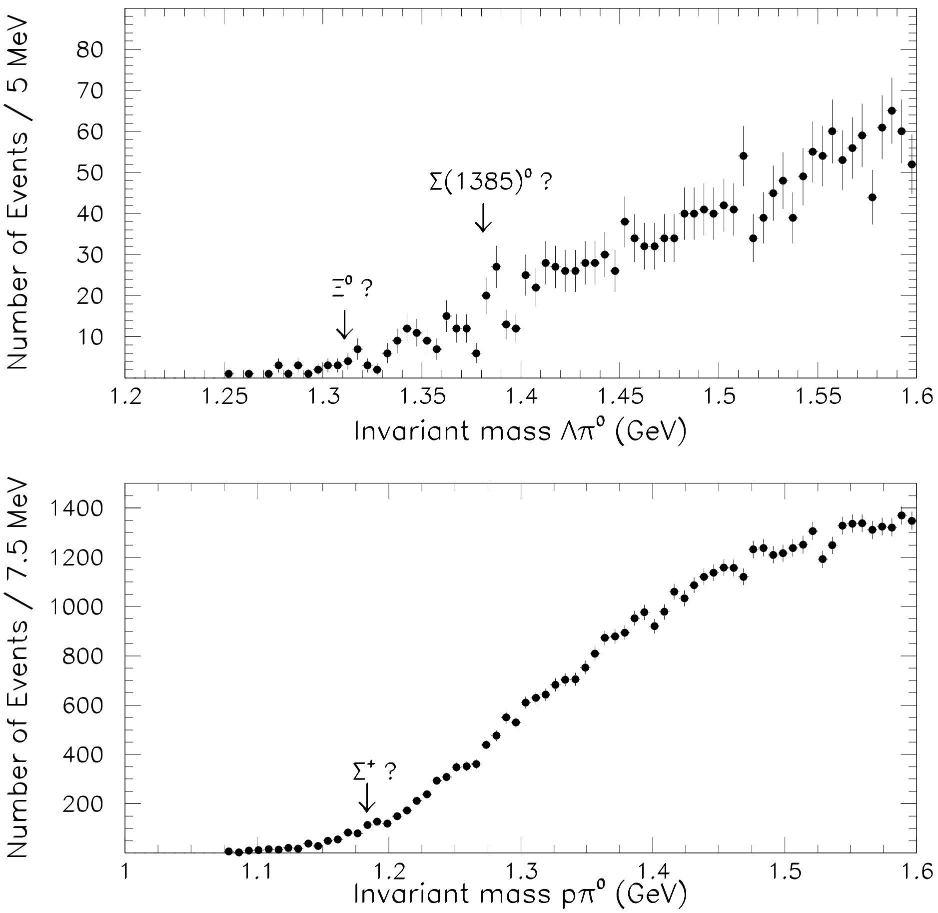

Figure 4.27: Invariant mass of $\Lambda\pi^0$ and $p\pi^0$, where the π^0 has been reconstructed via its decay $\pi^0 \rightarrow \gamma\gamma$.

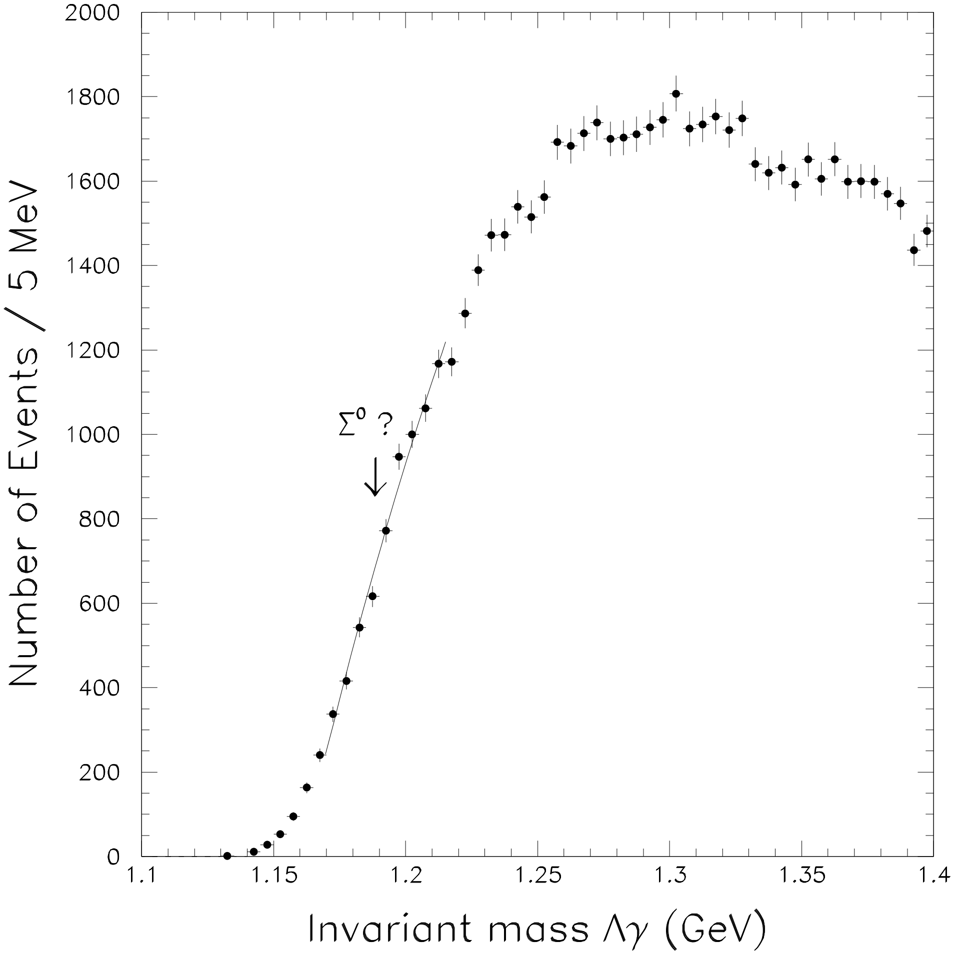

Figure 4.28: Invariant mass of $\Lambda\gamma$, where the γ is measured as a neutral cluster in the electromagnetic calorimeter.

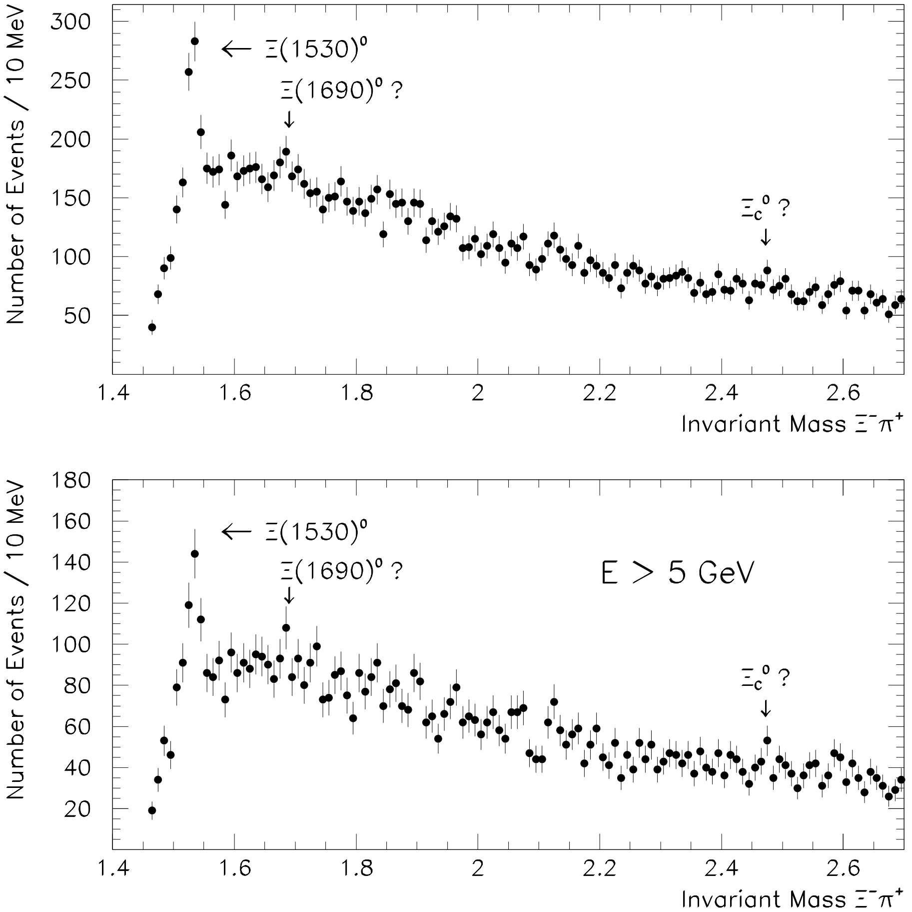

Figure 4.29: Invariant mass of $\Xi^-\pi^+$, for all energies and for $E_{\Xi\pi} > 5$ GeV.

the number of resonances found in the N and Λ systems, it is important to try to search for states heavier than the $\Xi(1530)^0$. We have made a search for additional Ξ resonances in the in the $\Xi^-\pi^+$ decay channel. The invariant mass of all $\Xi^-\pi^+$ combinations is shown in figure 4.29. A small two and a half standard deviation peak is seen near 1690 MeV. This enhancement, which could possibly be the $\Xi(1690)^0$, was also seen in our published paper based on the 1990 and 1991 data only [7]. Its significance is however still small even with the inclusion of the 1992 data, and can be explained as a statistical fluctuation.

The Ξ_C^0 has a mass of 2472.7 ± 1.7 MeV [15] and has only been observed in a few events at ARGUS and CLEO [49]. The mean lifetime is known only with about a 50% error from a sample of 4 events [50]. The measurement of the Ξ_C^0 lifetime would be interesting for the study of heavy flavors. The Ξ_C^0 decays to $\Xi^-\pi^+$ with a branching ratio of less than 30%[15]. The present search has turned up no convincing signal for the Ξ_C^0 (see figure 4.29), although there does appear to be a small enhancement in the appropriate mass region for events in which a cut is made on the minimum energy of $E_{\Xi\pi} > 5$ GeV. A similar search in a sample of events which have a high $p_t > 800$ MeV lepton with respect to a jet (which in Monte Carlo studies has been found to be more than 90% pure heavy flavor events [51]) also resulted in no signal.

4.8 Comparison with Monte Carlo Models

In this section, the results of our measurements on inclusive strange baryon production are compared with several Monte Carlo models (JETSET 7.3, HERWIG 5.6, and the UCLA Monte Carlo). In addition to the strange baryon results, we can use the recent measurements of vector mesons $K^*(892)^0$, $\phi(1020)$ [46], and $K^*(892)^\pm$ [52], and charged hadrons, p, K^+, π^+ [42], which were recently published by OPAL, to further test the models.

The JETSET Monte Carlo has the largest number of free parameters of the three models considered. The version of JETSET used by OPAL has been tuned to describe the global event shapes [53]. The effects of this tuning on meson and baryon production rates is negligible. In table 4.10 are listed some of the parameters relevant to the fragmentation of mesons and baryons. We have tuned these parameters to describe our inclusive particle yields (see table 4.11). A summary of the changes in the parameters is presented below:

- The proton rate is too high in JETSET. Since this rate is the dominant component of the total baryon rate, the diquark production probability (`PARJ(1)`) must be lowered slightly to 0.090 ± 0.005 from its default value of 0.10.

- The strange diquark suppression parameter (`PARJ(3)`) determines the Ξ^-/Λ ratio to a large extent. Since this ratio is too high in the Monte Carlo, this parameter must be lowered to 0.31 ± 0.04 from its default value of 0.40.

- Since the observed production of $\Sigma(1385)^{\pm}$ is a factor of two lower in the data than in the Monte Carlo, one must suppress its production too. The rate of $\Sigma(1385)^{\pm}$ is sensitive to the popcorn probability. Since a diquark which undergoes popcorn splitting loses all information about its spin, the production of spin 3/2 baryons is enhanced. Therefore, the spin 1 to spin 0 diquark probability (`PARJ(4)`) must be lowered by $20-80\%$, depending on the popcorn probability.

- Small changes in the meson spin parameters are necessary to get agreement with the observed production rates of the strange mesons.

Notable successes of this model are that it describes well the octet baryons and the lightest strange mesons. However, no tuning could get further agreement with the measured $\phi(1020)$ rate, or with more than one of the decuplet baryon rates. For the decuplet baryons, this phenomenon is illustrated in figure 4.30. For large variations in all of the diquark parameters, including the popcorn parameter, JETSET stayed within the dark bands in the figure, far away from the observed ratios of decuplet baryons. It seems that JETSET has a general problem describing the rates of the heavier spin 3/2 baryons and vector mesons.

The χ^2 per degree of freedom for each of the tunings for various popcorn parameters are about the same. It is impossible to constrain the popcorn probability by inclusive measurements alone. Since the popcorn parameter affects the rates of baryon pairs, we leave it to the next chapter to discuss the tuning of the popcorn parameter.

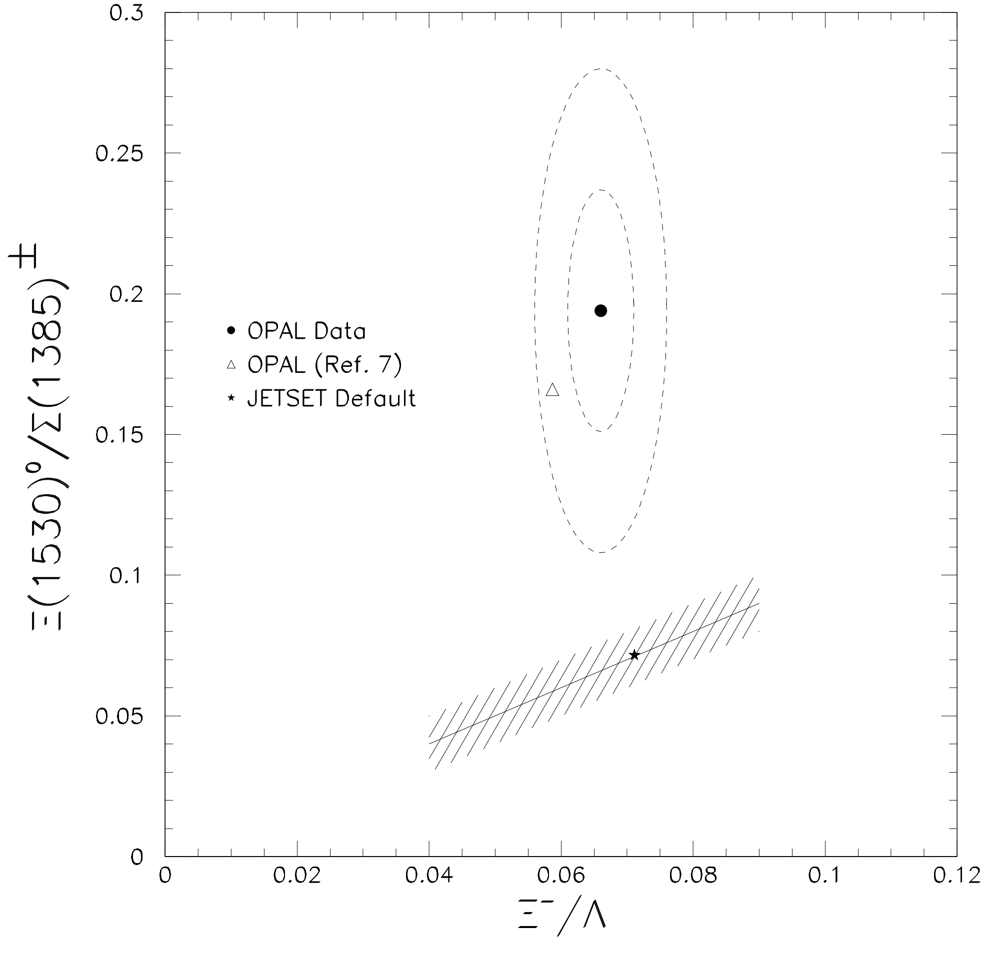

Figure 4.30: The ratio of decuplet baryons $\Xi(1530)^0/\Sigma(1385)^\pm$ versus the ratio of the octet baryons Ξ^-/Λ for data and for JETSET. The one and two sigma error ellipses are also shown. The shaded areas give the ratios obtained even with large variations in all of the diquark parameters in JETSET.

Although the inclusive rates of many baryons are well described by the tuned version of JETSET, the differential cross sections predicted by JETSET (and also HERWIG) are too hard in the models. A possible explanation of this is that more baryons are produced in gluon jets than in quark jets, and that this is not well modelled in the Monte Carlos.

The only parameters in the HERWIG Monte Carlo which affect baryon production rates are the maximum cluster mass parameter, `CLMAX`, and `CLPOW`. For version 5.4, the `CLMAX` parameter was set to a value of 2.80 to provide better agreement with the published OPAL Λ rate. Agreement with the meson and proton rates are also good. However, most of the other strange baryons rates differ by large factors (see table 4.12).

Baryon production rates were also obtained from the authors of the UCLA Monte Carlo (see table 4.12) [55]. In general the agreement with the data is very good. The $\Sigma(1385)^{\pm}$ rate suffers from the problem of being about a factor of two too large, as in the other Monte Carlos we have studied. However, the rates of all of the other strange baryons are in reasonable agreement.

4.9 Observed Regularities in Inclusive Particle Production Rates

It has long been known that the inclusive production rates of hadrons in e^+e^- collisions follow a roughly exponential distribution, $dn/dm \sim a \cdot \exp(-5m)$, where n is the rate of particle production and m is the hadron mass [5]. This relationship is only approximate; however, it is based on the total inclusive production of hadrons, including hadrons produced from secondary decays. If we wish to study baryon production, it is better to subtract the components of the rates which are due to decays of heavier states [5].

Although heavy baryons, such as $\Xi(1530)^0$, $\Sigma(1385)^{\pm}$, and Ω^- will mostly be primary hadrons, the lighter states such as the proton, Λ, and Ξ^- will often be produced in secondary decays. OPAL has measured the production rates of at least one baryon from almost all of the isospin multiplets, with the exception of the Δ and Σ (although these measurements are being carried out). We will assume that the primary production of the unmeasured charge states is the same as the measured states, and calculate the primary fractions. This is justified in part by the fact that the difference between the measured rates of $\Sigma(1385)^+$ and $\Sigma(1385)^-$ is consistent with zero:

$$\frac{N_{\Sigma(1385)^-} - N_{\Sigma(1385)^+}}{N_{\Sigma(1385)^-} + N_{\Sigma(1385)^+}} = 0.085 \pm 0.086$$

For the production rates of baryons for which we have no measurements in any charge state, we will make assumptions about their production rates and include correspondingly large errors.

In summary, the primary baryon rates can be determined as follows:

- Sources of secondary Ω^-, $\Xi(1530)^0$, and $\Sigma(1385)^{\pm}$ are heavy flavor baryons and heavier strange baryon resonances. Since the production of such states is rare, we will assume that these states are 100 ± 5% primary.

- The main source of secondary Ξ^- are the decays $\Xi(1530) \rightarrow \Xi\pi$. Given that the ratio $\Xi(1530)^0/\Xi^-$ has been measured to be 0.30, we can assume that $70 \pm 3.5\%$ of Ξ^- are primary.

- The main sources of secondary Λ are decays of all of the heavier strange baryons with the exception of the Σ^+ and the Σ^-, both of which decay to $N\pi$. This is fortunate since we have not measured the Σ rates. Assuming that the $\Sigma^0 \rightarrow \Lambda\gamma$ rate is 0.036 ± 0.034 (the error here is the magnitude of the disagreement with JETSET), the percentage of Λ which are primary is $63 \pm 3\%$.

- The largest contributors of secondary protons are Λ, Σ^+, and Δ decays to $p\pi$. Since the Δ rates and Σ^+ rate are unknown, this gives us a large systematic uncertainty in the primary proton rate. From the Λ rate alone, we know that at least 25% of the protons are secondary. Assuming 0.036 ± 0.034 for the Σ^+ rate and 0.06 ± 0.03 for the Δ rates, the fraction of primary protons is $61 \pm 8\%$.

The rates of primary baryons are summarized in table 4.13, and are plotted in figure 4.31. One notices the roughly exponential drop in the rates as a function of the baryon mass.

We now make a further assumption: instead of considering each individual charge state (or isospin I_3 state) of a baryon as a separate hadron, we can treat them as the same state. This is in effect assuming that there is no difference between an up quark and a down quark, except for their electric charge. For example, we will consider proton and neutron production

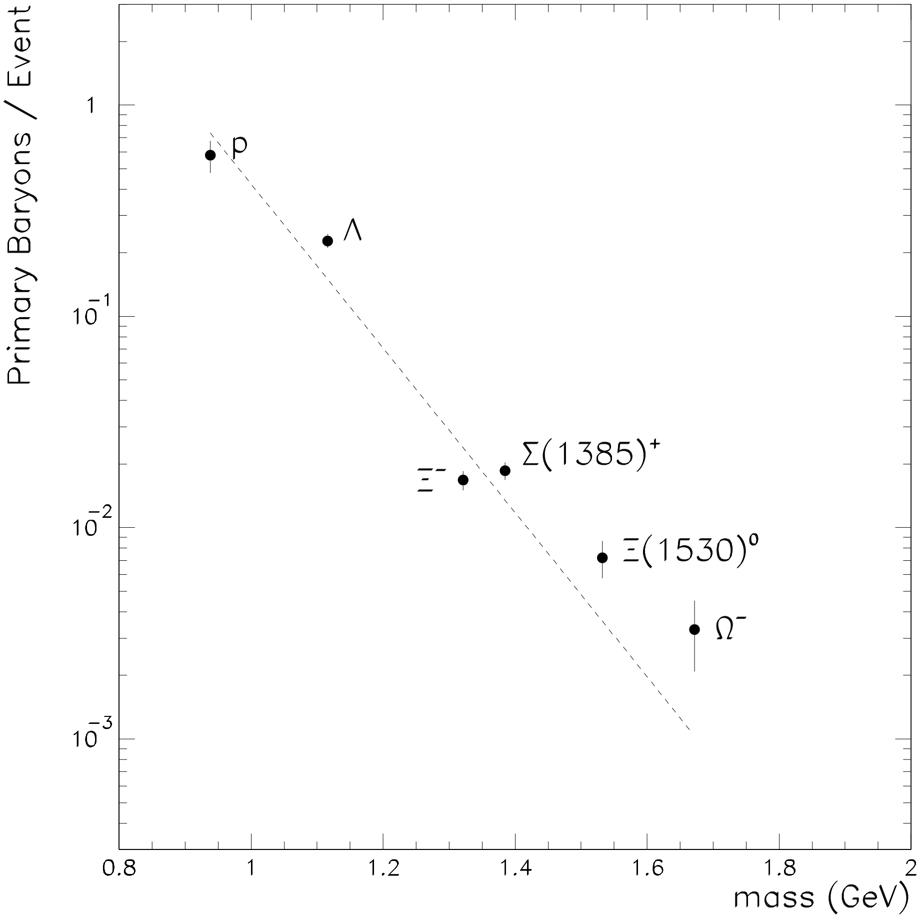

Figure 4.31: Rates of primary baryons (only one charge type considered). The straight line is a fit to the form $dn/dm = a \cdot \exp(-\beta m)$, where $1/\beta = 112 \pm 5$ MeV.

together, and combine Ξ^- and Ξ^0 production, etc. If one multiplies the rates of primary baryons by the number of available isospin (or charge) states, $(2I+1)$, the distribution in figure 4.32 is the result. We have multiplied the proton, Ξ^-, and $\Xi(1530)^0$ rates by two, and the $\Sigma(1385)^\pm$ rate by $\frac{3}{2}$.

A clearly exponential drop is now seen in the production rates as a function of mass. The points were fitted to the form $n_i = e^{\beta\mu} \cdot e^{-\beta m_i}$, with the result that:

- $1/\beta = 108\pm\ 6$ MeV for $J^P = \frac{1}{2}^+$
- $1/\beta = 104\pm\ 7$ MeV for $J^P = \frac{3}{2}^+$.

The slope of the two curves is the same within the fit uncertainty. The decuplet baryons lie on a higher trajectory than the octet baryons, with the fit parameters:

- $\mu = 955 \pm 13$ MeV for $J^P = \frac{1}{2}^+$
- $\mu = 1085 \pm 23$ MeV for $J^P = \frac{3}{2}^+$.

The ratio of the rates of two hypothetical octet and decuplet baryons which have the same mass is:

$$R = \exp(\mu_{J^P=\frac{3}{2}^+}/\mu_{J^P=\frac{1}{2}^+}) = 3.11 \pm 0.08,$$

where the error is the error from the fit.

We can account for the difference between the rates of spin 3/2 and spin 1/2 baryons by noting that there are more available spin states for the

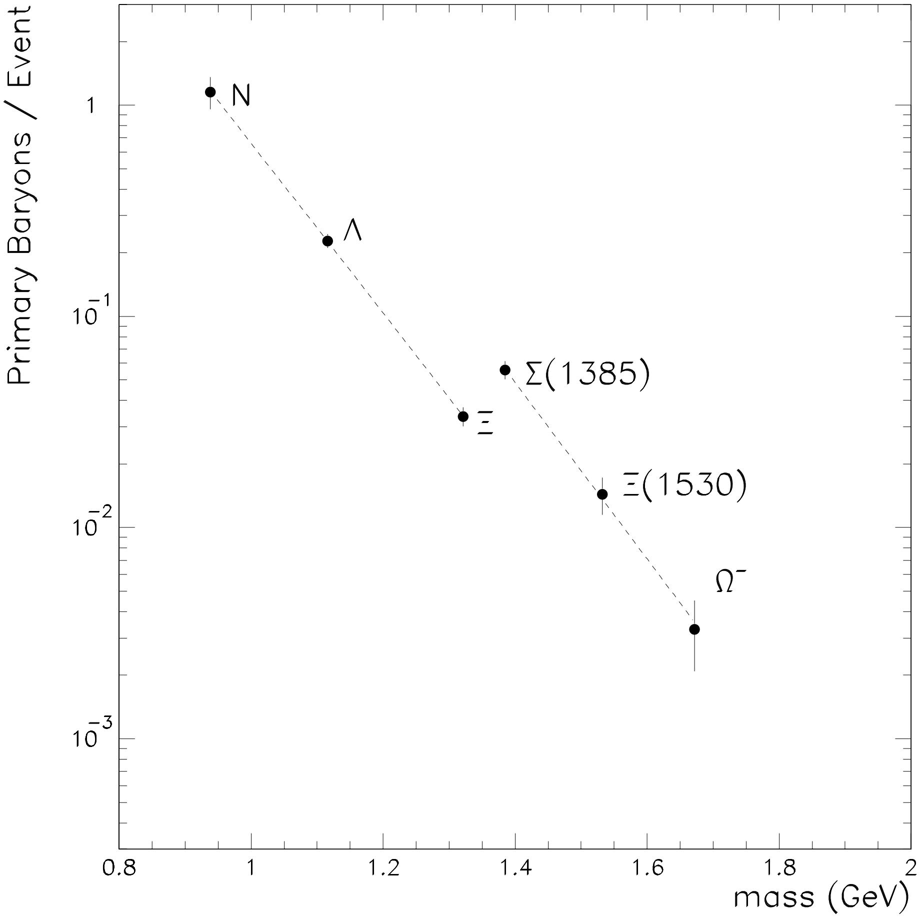

Figure 4.32: Rates of primary baryons in each isospin multiplet.

decuplet baryons. Simple spin counting would give us a factor two, since the ratio of the number of spin states for decuplet baryons and octet baryons is $R = \frac{2(\frac{3}{2})+1}{2(\frac{1}{2})+1} = 2$. However, the imposition of baryon number conservation imposes restrictions on the number of *available* states [56]. If we make the assumption that the objects which produce baryons are spin 1 objects (diquarks? gluons?), and then calculate how many ways we can express a $|1, \pm 1\rangle$ state as the sum of a baryon-antibaryon state, $|J, J_z\rangle + |J', J'_z\rangle$, we find that the ratio of spin 3/2 to spin 1/2 baryons is 24/8=3. If the diquarks or gluons are also allowed to be in a $J_z = 0$ state, then the ratio is 38/12=3.17. Both assumptions are in good agreement with the observed ratio of 3.11±0.08 in the data.

4.9.1 Comparison with Results at Lower Energies

Taking the data on strange baryon production from PEP and PETRA at $\sqrt{s} = 29 - 34$ GeV, and from CLEO and ARGUS at 10 GeV (continuum), and performing the same sort of analysis, one finds the results in figure 4.33. The decuplet baryons have been scaled down by a factor of 12/38 for spin counting in this figure. The results are rather encouraging, in that the slopes are consistent over a wide range of center-of-mass energies (see table 4.14).

The total baryon production rate scales with the center-of-mass energy. Examining the proton and Λ rates at different center-of-mass energies (see figure 4.34 for example), the baryon production rates are found to scale over the range of center-of-mass energies from 10 to 91 GeV as $\log\left(\frac{\sqrt{s}}{\epsilon}\right)$, where the constant $\epsilon = 4.1 \pm 0.5$ GeV,

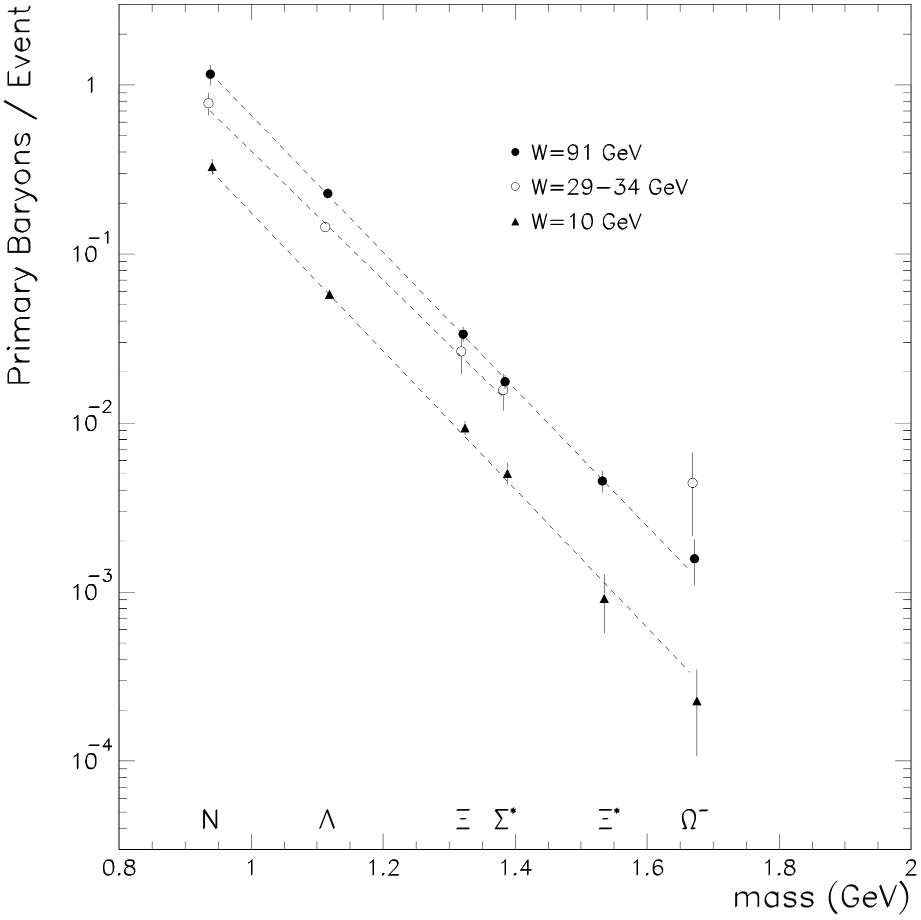

Figure 4.33: Rates of primary baryons multiplied by the number of available isospin states, at different center-of-mass energies. The decuplet baryons have been scaled down by a spin factor of 12/38.

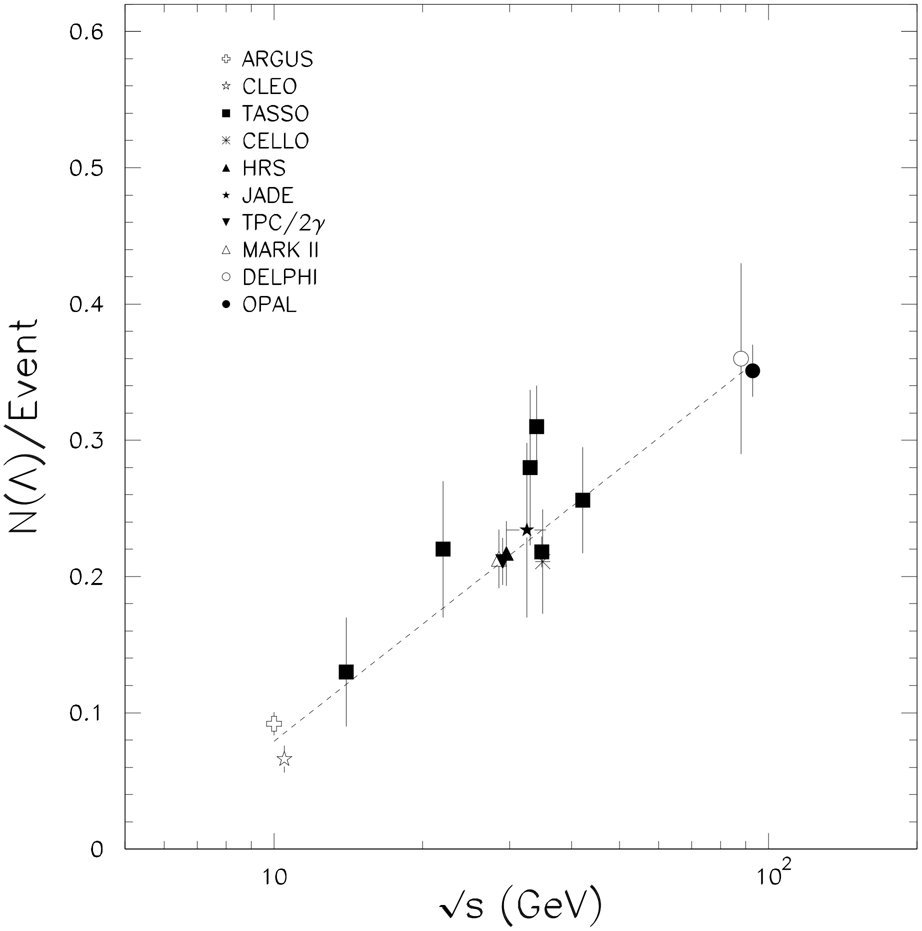

Figure 4.34: The number of $\Lambda(\overline{\Lambda})$ produced per multihadronic event as a function of the center-of-mass energy. The rate is found to scale as $\log(E_{\text{c.m.}}/\epsilon)$ for energies above 10 GeV.

Baryon production rates at a particular center-of-mass energy can be described by the following formula, which depends only of the mass and spin of the baryon and the number of charge (or isospin) states.

$$n = A \cdot \frac{g_s}{(2I+1)} \cdot \log\left(\frac{\sqrt{s}}{\epsilon}\right) \cdot \exp(-\beta m)$$

The parameters have been determined from a global fit to the baryon production rates from ARGUS and CLEO at $\sqrt{s} = 10$ GeV, PEP and PETRA at $29 - 34$ GeV, and OPAL at 91 GeV:

- g_s is a spin factor, equal to 38 for $J^P = \frac{3}{2}^+$ baryons, and equal to 12 for $J^P = \frac{1}{2}^+$ baryons.
- $2I + 1$ is the isospin multiplicity.
- $\epsilon = 4.1 \pm 0.4$ GeV.
- $1/\beta = 110 \pm 2$ MeV.
- $A = 129 \pm 5$, is an overall normalization.

The overall χ^2 per degree of freedom of the fit is approximately one. The value of the factor A, the overall normalization, is strongly correlated to the value of ϵ. One might expect that at center-of-mass energies close to ϵ this formula would need further corrections, since the phase space for baryon production is much smaller. The other two fit parameters are energy scales, one of which determines the scaling to different center-of-mass energies, and one of which is the "temperature" which describes the Boltzmann distribution of baryon production. Several statistical models of hadron production in e^+e^- annihilation[57] and in hadron collisions [56] have been proposed in the past.

The ARGUS collaboration measured the production of Δ^{++} at $\sqrt{s}=$ 10 GeV (continuum) to be 0.040±0.008±0.006 per event [58], which disagrees by about two and a half standard deviations with the prediction of of 0.015 from the above formula. The rate of $\Delta^{++} \rightarrow p\pi^+$ is very difficult to measure because the phase space of $p\pi^+$ pairs has its maximum under the signal, making an estimate of the background difficult. In better agreement is the Σ^0 rate from ARGUS, which is 0.0229±0.0085, only one and a half standard deviations from the prediction of 0.0090 from the above formula [59].

An accurate measurement of either the Δ^{++} or the Σ^0 at $\sqrt{s}=m_{Z^0}$ would be a good test of the formula presented here. The predicted rates for the production of these two states are: $\sqrt{s}=m_{Z^0}$:

- N_{Σ^0}/Event=0.036
- $N_{\Delta^{++}}$/Event=0.062

These rates are for baryons produced from the fragmentation, not from secondary decays of heavier states. Both of these rates are below the predicted JETSET rates of 0.07 primary Σ^0 per event and 0.18 primary Δ^{++} per event.

4.9.2 Meson Production

A similar analysis can be performed on the inclusive meson rates from LEP experiments. For the measured rates (see table 4.11), we have results on pseudoscalar and vector mesons from OPAL for $\pi^{\pm}$ and $\mathrm{K}^{\pm}$ [42], for $\mathrm{K}^{*}(892)$ and $\phi(1020)$ [46], and for K^0_S [54]. Also available are the measurements of the π^0 from L3 [48], the η and η' from ALEPH [60], and the $\rho(770)$ from DELPHI [61]. A preliminary measurement of the $\omega(783)$ has also been carried out at OPAL [62].

The rates of primary mesons are more difficult to calculate due to the large number of states which decay into light mesons. Therefore, we have used the primary fractions of mesons which are produced in JETSET, since with the exception of the $\phi(1020)$, JETSET can be tuned to agree with the measured inclusive meson rates.

The results are shown in figure 4.35 for the rates of primary mesons in each isospin multiplet, along with the primary baryon rates for comparison. The dashed lines are fits to the form $n_i = e^{\beta\mu} \cdot e^{-\beta m_i}$. From the fit we find that for vector mesons $1/\beta = 70 \pm 4$ MeV, and for pseudoscalar mesons $1/\beta = 200 \pm 10$ MeV.

The production of mesons appears to be qualitatively different from that of baryons. However, some regularities are evident. The rates of primary π and $\rho(770)$ are about the same, as are the rates of primary K and $\mathrm{K}^{*}(892)$. Comparing the rates of the other vector and pseudoscalar mesons shows disagreement, but in the quark model the η and η' are mixtures of different

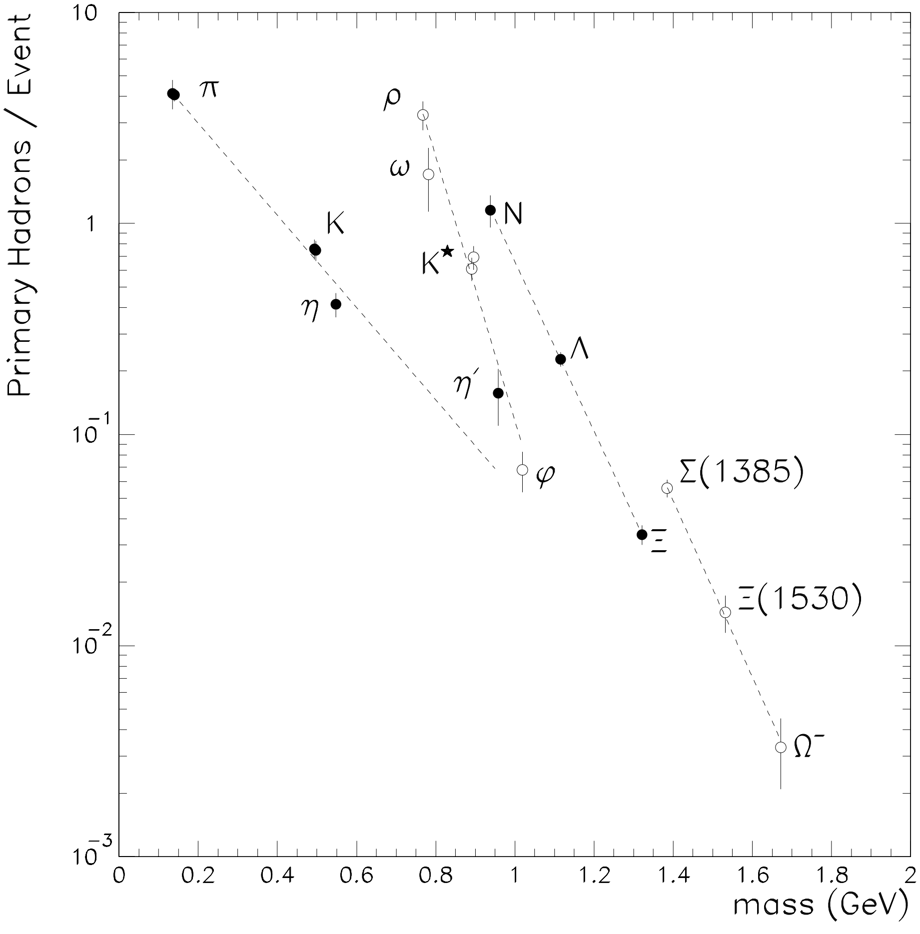

Figure 4.35: Rates of primary baryons and mesons in each isospin multiplet.

flavors, as are the $\omega(783)$ and the $\phi(1020)$. Therefore, the interpretation of the production rates in terms of a simple relation is difficult. If one takes the average slope of the two meson curves, the result is not so different from the baryon case.

The effect of strangeness suppression seems to be the same in both the pseudoscalar and vector mesons, since the ratios of primary K/π and $K^*(892)/\rho(770)$ are both about 0.2. This is consistent with a simple mass suppression of strange quark production from the sea [24].

x_p	n	Efficiency	$\langle x_p \rangle$	$(1/\mathrm{N}_{had})dn/dx_p$	$\langle x_E \rangle$	$(1/\mathrm{N}_{had})dn/dx_E$
.01- .015	284. ± 19.	.022 ± .002	.013	3.152 ± .206 ± .005	.028	6.954 ± .454 ± .012
.015- .02	873. ± 32.	.061 ± .002	.018	3.532 ± .129 ± .008	.030	6.086 ± .222 ± .014
.02- .03	3366. ± 68.	.113 ± .003	.025	3.685 ± .074 ± .012	.035	5.183 ± .105 ± .016
.03- .04	4135. ± 81.	.143 ± .003	.035	3.583 ± .070 ± .012	.043	4.382 ± .086 ± .014
.04- .05	4667. ± 100.	.189 ± .004	.045	3.062 ± .066 ± .014	.051	3.490 ± .075 ± .016
.05- .06	4597. ± 98.	.223 ± .007	.055	2.548 ± .054 ± .017	.060	2.790 ± .059 ± .018
.06- .07	4040. ± 88.	.246 ± .011	.065	2.036 ± .044 ± .023	.069	2.176 ± .047 ± .024
.07- .08	3381. ± 71.	.239 ± .008	.075	1.748 ± .037 ± .013	.079	1.839 ± .039 ± .014
.08- .10	5445. ± 87.	.243 ± .007	.090	1.387 ± .022 ± .010	.093	1.438 ± .023 ± .011
.10- .15	8274. ± 109.	.237 ± .009	.123	.865 ± .011 ± .008	.125	.882 ± .012 ± .008
.15- .20	4254. ± 79.	.212 ± .010	.173	.496 ± .009 ± .005	.175	.501 ± .009 ± .005
.20- .30	4170. ± 79.	.170 ± .005	.245	.304 ± .006 ± .001	.245	.306 ± .006 ± .001
.30- .40	1403. ± 48.	.125 ± .006	.344	.139 ± .005 ± .001	.345	.139 ± .005 ± .001
.40- .50	573. ± 31.	.104 ± .009	.443	.068 ± .004 ± .001	.444	.068 ± .004 ± .001
.50- .60	181. ± 18.	.082 ± .010	.543	.027 ± .003 ± .001	.543	.027 ± .003 ± .001
.60- .70	60. ± 10.	.061 ± .008	.642	.012 ± .002 ± .001	.643	.012 ± .002 ± .001

Table 4.4: Differential cross section for Λ where both tracks are required to have at least 4 associated z-chamber hits. The error in the efficiency includes the Monte Carlo statistical error and the systematic error in the z-chamber correction. Not included in the systematic errors are errors which are due to the overall normalization of the cross section.

x_p	n	Efficiency	$\langle x_p \rangle$	$(1/\mathrm{N}_{had})dn/dx_p$	$\langle x_E \rangle$	$(1/\mathrm{N}_{had})dn/dx_E$
.01- .015	1018. ± 38.	.080 ± .003	.013	3.150 ± .118 ± .009	.028	6.948 ± .260 ± .019
.015- .02	2327. ± 55.	.163 ± .004	.018	3.531 ± .083 ± .013	.030	6.086 ± .143 ± .022
.02- .03	7765. ± 108.	.261 ± .004	.025	3.685 ± .051 ± .013	.035	5.183 ± .072 ± .019
.03- .04	8680. ± 126.	.300 ± .004	.035	3.583 ± .052 ± .016	.043	4.382 ± .064 ± .019
.04- .05	9129. ± 151.	.369 ± .006	.045	3.063 ± .050 ± .019	.051	3.490 ± .058 ± .022
.05- .06	8229. ± 142.	.400 ± .007	.055	2.548 ± .044 ± .018	.060	2.790 ± .048 ± .019
.06- .07	6778. ± 124.	.412 ± .007	.065	2.035 ± .037 ± .015	.069	2.175 ± .040 ± .016
.07- .08	5660. ± 99.	.401 ± .009	.075	1.747 ± .030 ± .016	.079	1.838 ± .032 ± .016
.08- .10	8902. ± 119.	.397 ± .009	.090	1.386 ± .018 ± .012	.093	1.437 ± .019 ± .013
.10- .15	12597. ± 144.	.361 ± .010	.123	.862 ± .010 ± .008	.125	.879 ± .010 ± .008
.15- .20	6084. ± 103.	.305 ± .011	.173	.493 ± .008 ± .005	.175	.498 ± .008 ± .005
.20- .30	6173. ± 101.	.252 ± .010	.245	.303 ± .005 ± .003	.245	.305 ± .005 ± .003
.30- .40	1955. ± 59.	.175 ± .009	.344	.138 ± .004 ± .001	.345	.138 ± .004 ± .001
.40- .50	746. ± 37.	.137 ± .008	.443	.068 ± .003 ± .001	.444	.068 ± .003 ± .001
.50- .60	249. ± 22.	.113 ± .008	.543	.027 ± .002 ± .001	.543	.027 ± .002 ± .001
.60- .70	86. ± 13.	.087 ± .011	.642	.012 ± .002 ± .001	.643	.012 ± .002 ± .001

Table 4.5: Differential cross section for Λ using all accepted track combinations. The error in the efficiency includes the Monte Carlo statistical error and the systematic error in the z-chamber correction. Not included in the systematic errors are errors which are due to the overall normalization of the cross section.

x_p	n	Efficiency	$\langle x_p \rangle$	$(1/\mathrm{N}_{had}) dn/dx_p$	$\langle x_E \rangle$	$(1/\mathrm{N}_{had}) dn/dx_E$
0.02-0.05	421. ± 28.	.078 ± .005	.034	.2250 ± .0149 ± .0190	.045	.2990 ± .0197 ± .0252
0.05-0.10	956. ± 49.	.212 ± .007	.072	.1133 ± .0058 ± .0080	.078	.1223 ± .0063 ± .0086
0.10-0.15	539. ± 35.	.202 ± .009	.123	.0671 ± .0043 ± .0052	.126	.0689 ± .0044 ± .0053
0.15-0.20	275. ± 25.	.175 ± .011	.173	.0395 ± .0036 ± .0034	.176	.0400 ± .0037 ± .0035
0.20-0.30	188. ± 23.	.111 ± .007	.245	.0212 ± .0026 ± .0019	.247	.0214 ± .0026 ± .0019
0.30-0.40	53. ± 13.	.070 ± .008	.345	.0095 ± .0023 ± .0012	.346	.0095 ± .0024 ± .0012
0.40-0.50	21. ± 6.	.035 ± .007	.444	.0075 ± .0022 ± .0016	.445	.0075 ± .0022 ± .0016

Table 4.6: Differential cross section for Ξ^-. The error in the efficiency is the Monte Carlo statistical error.

x_p	n	Efficiency	$\langle x_E \rangle$	$(1/\mathrm{N}_{had}) dn/dx_E$
0.01-0.04	625 ± 147	0.101 ± 0.007	0.038	0.475 ± 0.111 ± 0.031
0.04-0.10	2789 ± 295	0.252 ± 0.016	0.074	0.284 ± 0.030 ± 0.018
0.10-0.20	1302 ± 205	0.265 ± 0.017	0.145	0.071 ± 0.011 ± 0.004
0.20-0.30	316 ± 110	0.231 ± 0.016	0.245	0.019 ± 0.006 ± 0.001
0.30-0.50	245 ± 73	0.160 ± 0.011	0.382	0.011 ± 0.003 ± 0.001

Table 4.7: Differential cross section for $\Sigma(1385)^{\pm}$, where the first error in the cross section is statistical and the second is the systematic error from the efficiency determination.

x_p	n	Efficiency	$\langle x_E \rangle$	$(1/\mathrm{N}_{\mathrm{had}}) dn/dx_E$
0.04-0.10	63 ± 23	0.096 ± 0.011	0.074	0.0235 ± 0.0086 ± 0.0028
0.10-0.20	134 ± 22	0.121 ± 0.015	0.146	0.0217 ± 0.0036 ± 0.0027
0.20-0.30	20 ± 11	0.068 ± 0.016	0.246	0.0057 ± 0.0031 ± 0.0013
0.30-0.50	8 ± 7	0.026 ± 0.010	0.383	0.0030 ± 0.0026 ± 0.0011

Table 4.8: Differential cross section for $\Xi(1530)^0$, where the first error for the cross section is statistical and the second is the systematic error from Monte Carlo statistics.

$\Lambda(\overline{\Lambda})$/event	0.363 ± 0.002 (stat) ± 0.022 (syst)
$\Xi^-(\overline{\Xi}^+)$/event	0.0240 ± 0.0007 (stat) ± 0.0017 (syst)
$\Sigma(1385)^{\pm}(\overline{\Sigma}(1385)^{\pm})$/event	0.0372 ± 0.0032 (stat) ± 0.0039 (syst)
$\Xi(1530)^0(\overline{\Xi}(1530)^0)$/event	0.0072 ± 0.0010 (stat) ± 0.0009 (syst)
$\Omega^-(\overline{\Omega}^+)$/event	0.0033 ± 0.0008 (stat) ± 0.0009 (syst)

Table 4.9: Total inclusive rates for strange baryons.

Parameter	Function	Default Value	Tuned 0%	Tuned 50%	Tuned 80%
`PARJ(1)`	qq/q	0.10	0.085	0.090	0.095
`PARJ(2)`	s/u	0.30	0.30	0.30	0.30
`PARJ(3)`	(us/ud)/(s/d)	0.40	0.28	0.34	0.31
`PARJ(4)`	$1/3\times(\mathrm{ud}_1/\mathrm{ud}_0)$	0.050	0.042	0.015	0.006
`PARJ(5)`	popcorn	0.50	0.00	0.50	2.00
`PARJ(11)`	$\mathrm{M}(\mathrm{ud}_1)$	0.50	0.60	0.60	0.60
`PARJ(12)`	$\mathrm{M}(\mathrm{us}_1)$	0.60	0.40	0.40	0.40
χ^2/DOF		8.78	2.13	1.74	1.85

Table 4.10: JETSET default parameters, and tuned sets of parameters for different values of the popcorn probability.

Particle	OPAL multiplicity	JETSET default	JETSET tuned
all charged	21.40 ± 0.43	21.35	21.35
π^+	17.09 ± 0.44	16.97	17.04
K^0	2.10 ± 0.14	2.15	2.19
K^+	2.38 ± 0.13	2.26	2.29
$K^*(892)^0$	0.76 ± 0.09	1.05	0.75
$K^*(892)^\pm$	0.72 ± 0.08	1.09	0.79
$\phi(1020)$	0.086 ± 0.018	0.185	0.136
p	0.95 ± 0.10	1.15	1.09
Λ	0.363 ± 0.023	0.382	0.365
Ξ^-	0.0240 ± 0.0022	0.0247	0.0265
$\Sigma(1385)^\pm$	0.0372 ± 0.0031	0.0728	0.0369
$\Xi(1530)^0$	0.0072 ± 0.0014	0.0060	0.0033
Ω^-	0.0033 ± 0.0012	0.0002	0.0003

Table 4.11: A comparison with JETSET of results on inclusive particle production using OPAL data. The JETSET Monte Carlo default (third column) has been tuned to fit overall OPAL event shapes and describes well the rates of the spin 1/2 mesons, but overestimates most of the baryon and vector meson production rates. Better agreement is obtained with tuned fragmentation parameters (fourth column). The popcorn probability was left at its default value of 50%.

Particle	OPAL multiplicity	HERWIG default	UCLA [55]
all charged	21.40 ± 0.43	21.43	20.3
π^+	17.09 ± 0.44	16.78	16.66
K^0	2.10 ± 0.14	2.20	2.02
K^+	2.38 ± 0.13	2.46	2.23
$\mathrm{K}^*(892)^0$	0.76 ± 0.09	0.88	0.73
$\mathrm{K}^*(892)^\pm$	0.72 ± 0.08	0.93	0.79
$\phi(1020)$	0.086 ± 0.018	0.135	0.125
p	0.95 ± 0.10	0.83	1.03
Λ	0.363 ± 0.023	0.351	0.330
Ξ^-	0.0240 ± 0.0022	0.037	0.0229
$\Sigma(1385)^\pm$	0.0372 ± 0.0031	0.120	0.0756
$\Xi(1530)^0$	0.0072 ± 0.0014	0.014	0.0088
Ω^-	0.0033 ± 0.0012	0.004	0.0010

Table 4.12: A comparison of results on inclusive particle production using OPAL data with Monte Carlos. The HERWIG Monte Carlo default (third column) has been tuned to agree with the published Λ multiplicity from OPAL. Estimations from the UCLA Monte Carlo are also given.

Baryon	Total Rate	Known / Estimated Sources	(BR)	Rate	Primary Rate
p	0.95±0.10	$\Lambda \to p\pi^-$	64.1%	0.233	0.578±0.102
		$\Sigma^+ \to p\pi^0$	51.6%	0.019 †	
		$\Delta(1232) \to p\pi$	50%	0.120 †	
Λ	0.363±0.023	$\Xi^- \to \Lambda\pi^-$	100%	0.024	0.228±0.018
		$\Xi^0 \to \Lambda\pi^0$	100%	0.024 §	
		$\Omega^- \to \Lambda K^-$	67.8%	0.0022	
		$\Sigma^0 \to \Lambda\gamma$	100%	0.036 †	
		$\Sigma(1385)^\pm \to \Lambda\pi^\pm$	88%	0.033	
		$\Sigma(1385)^0 \to \Lambda\pi^0$	88%	0.016 §	
Ξ^-	0.0240±0.0022	$\Xi(1530)^0 \to \Xi^-\pi^+$	67%	0.0048	0.0168±0.0018
		$\Xi(1530)^- \to \Xi^-\pi^0$	33%	0.0024 §	
		$\Omega^- \to \Xi^-\pi^0$	8.6%	0.0003 ¶	
$\Sigma(1385)^\pm$	0.0372±0.0031	None			0.0372±0.0036
$\Xi(1530)^0$	0.0072±0.0014	None			0.0072±0.0014
Ω^-	0.0033±0.0012	None			0.0033±0.0012

Table 4.13: Primary fraction and rates of baryons. Estimated rates are from isospin invariance (§), or from a measured rate in a different decay mode (¶), or from the formula presented below(†). The decuplet baryons are assumed to be 100 ± 5% primary.

$\sqrt{s}$	Slope $1/\beta$	Intercept μ
91 GeV	109±4 MeV	953±14 MeV
29-34 GeV	115±12 MeV	896±24 MeV
10 GeV	107±4 MeV	813±14 MeV

Table 4.14: Results of the fit to baryon production rates at different center-of-mass energies.

Chapter 5

Correlations Between Baryon Pairs

A general assumption of jet hadronization is that particles are produced in a chain-like way, with local conservation of quantum numbers. A consequence of such an assumption is a small rapidity[1] difference between neighboring particles in the chain.

Different chains have been implemented in Monte Carlo models. Modifications of the chain in which a baryon and antibaryon are produced consecutively (such as in HERWIG), to one in which other chains, such as baron-meson-antibaryon are possible (such as in JETSET), change the strength of the rapidity correlations.

At PEP and PETRA energies ($\sqrt{s} \approx 30$ GeV) it was shown that baryon number is dominantly conserved within the same hemisphere [63]. However, at LEP energies one can investigate rapidity correlations with large statistics.

---

[1] The rapidity of a particle is defined as $y = \frac{1}{2}\log(E + p_{||})/(E - p_{||})$, where E is the energy and $p_{||}$ is the momentum in the direction of the thrust axis.

In a recent publication [8], OPAL presented results on baryon correlations in jets based on the 1990 and 1991 data samples. We measured production rates of $\Lambda\overline{\Lambda}$, $\Xi^-\overline{\Lambda}$, and $\Xi^-\overline{\Xi}^+$ pairs, and short-range rapidity correlations between pairs of $\Lambda\overline{\Lambda}$. Results were compared to three Monte Carlo models of baryon production: JETSET, HERWIG, and the UCLA Monte Carlos. An indication of a long-range correlation between high momentum Λ's and $\overline{\Lambda}$'s in opposite hemispheres was observed but not conclusively proved. From model expectations, if high momentum baryons in opposite hemispheres contain the primary quarks of the Z^0 decays, or are decay daughters of such particles, there should be observed a long-range compensation of strangeness in opposite baryon number pairs.

Now with higher statistics available from the inclusion of the 1992 data in the analysis, it is possible to measure the pair rates (especially the $\Xi^-\overline{\Lambda}$, and $\Xi^-\overline{\Xi}^+$ production rates) with better accuracy and to improve the measurements of correlations between $\Lambda\overline{\Lambda}$ pairs.

5.1 Selection of Strange Baryon Pairs

For this search, we consider only multihadronic events whose thrust axis lies well inside the detector acceptance by making a cut of $|\cos\theta_{thrust}| < 0.8$. The thrust axis is a property of the event as a whole, and is defined as the vector $\vec{n}$ which maximizes the quantity

$$T = max\Big(\frac{\sum_i |\vec{p}_i \cdot \vec{n}|}{\sum_i |\vec{p}_i|}\Big) ,$$

where i is summed over all charged tracks and neutral electromagnetic clusters. This cut on the thrust axis minimizes systematic effects which arise when the baryon pair is produced near the edge of the acceptance.

We search for events with two or more $\Lambda(\overline{\Lambda})$ candidates. Tagging on one member of the pair (the baryon if the two have opposite baryon number), and requiring that its mass fall in the Λ mass range (± 10 MeV around the Λ mass of 1115.63 MeV for $x_p < 0.2$, and ± 15 MeV for higher momentum Λ's), we obtain the mass distribution of all other candidates of opposite and same baryon number pairs as plotted in figure 5.1.

As can be clearly seen in the figure, the combinatoric background outside the signal region is the same in both cases. Under the assumption that the production of same baryon number pairs is uncorrelated, the mass distribution for like pairs can be used to estimate the background due to both the combinatorial background and uncorrelated production in the opposite baryon number case. Aslo in figure 5.1 the difference of the two distributions is plotted. A total of 4674 ± 85 $\Lambda\overline{\Lambda}$ pairs are found in the Λ signal region, defined above, and a total of 1818 ± 62 same baryon number pairs. After background subtraction, we find a total of 2856 ± 105 *correlated* $\Lambda\overline{\Lambda}$ pairs.

The efficiency for finding Λ pairs has been studied, and no significant influence on the efficiency of finding the second Λ due to the tagging of the first has been found. The efficiency has been calculated with the same method as in the previous chapter, but using Monte Carlo events which have their reconstructed thrust axes within the acceptance of $|\cos\theta_{\text{thrust}}| < 0.8$. A plot

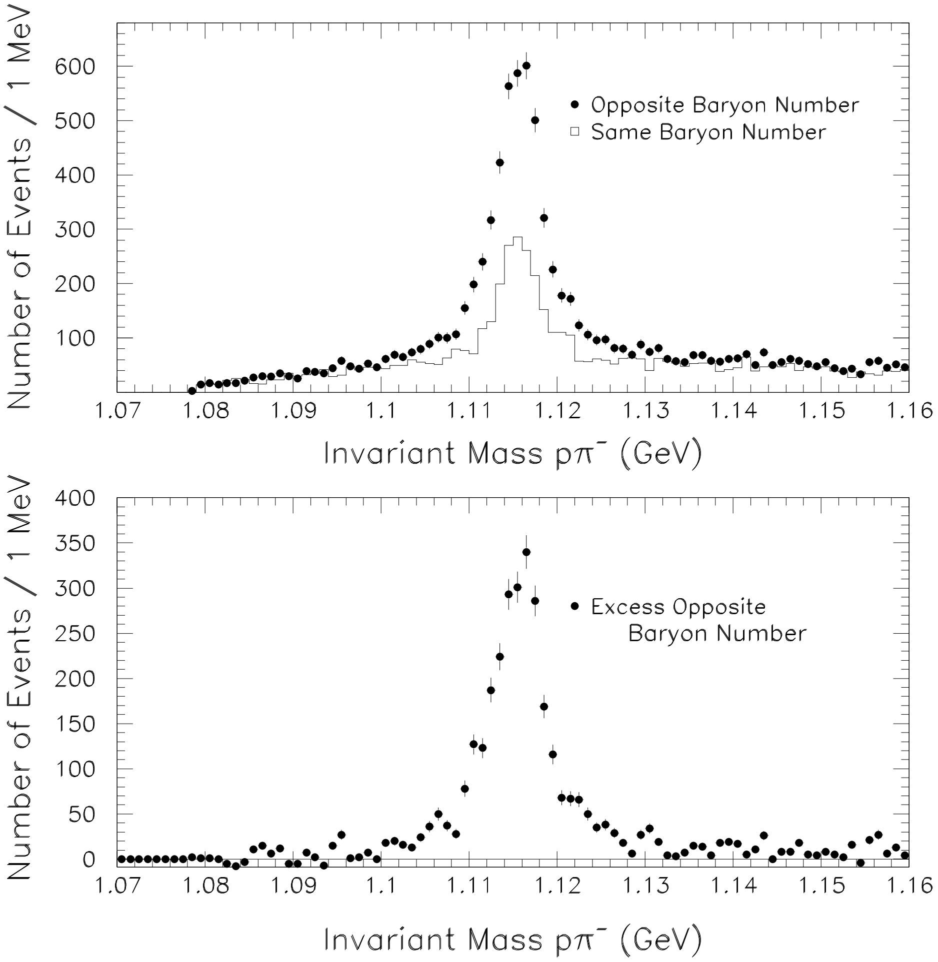

Figure 5.1: The invariant mass distribution $p\pi^-$ for in events which have a tagged $\Lambda(\overline{\Lambda})$. The cases for opposite sign baryon number pairs (in which the baryon is the tag) and like sign baryon number pairs (in which the tag is random) are plotted. Plotted below is the difference of the two distributions above.

of the efficiency for reconstructing $\Lambda \to p\pi^-$ in events which pass the thrust cut is shown in figure 5.2. This efficiency has the same general shape as the Λ finding efficiency in all multihadron events, rising sharply from zero to a maximum of 45% at $x_p = 0.08$, and then falling slowly as the momentum increases, to 23% at $x_p = 0.3$ and to 13% at $x_p = 0.5$. This efficiency is numerically higher than the efficiency from the total event sample because we base it on the sample of events which already pass the thrust cut.

Using the single Λ efficiency, one finds the overall rate of correlated $\Lambda\overline{\Lambda}$ pairs per hadronic Z^0 decay to be:

- $N_{\Lambda\overline{\Lambda}}/\mathrm{event} = 0.0613 \pm 0.0023$ (stat) ± 0.0064 (syst).

The systematic error for the single Λ measurement is taken to be the same as in the inclusive Λ case, 7.4%. The only difference is that in the calculation of the pair rate, the systematic errors from the efficiency calculation enter only once. Therefore, the total systematic error for the pair rate calculation is 10.4%. The correlated pair rate can be compared to the OPAL published value of 0.0621 ± 0.0034 (stat) ± 0.0084 (syst) [7].

The rate for same baryon number pair production can likewise be calculated. To subtract the background in the tagging sample, we assume that no correlated same baryon number pair production takes place. Therefore, the fraction of real Λ's in the tagged sample which have a background Λ as a tag depends on the signal to background ratio in the tagging sample. With this method, one can count the number of same baryon number pairs per hadronic event to be:

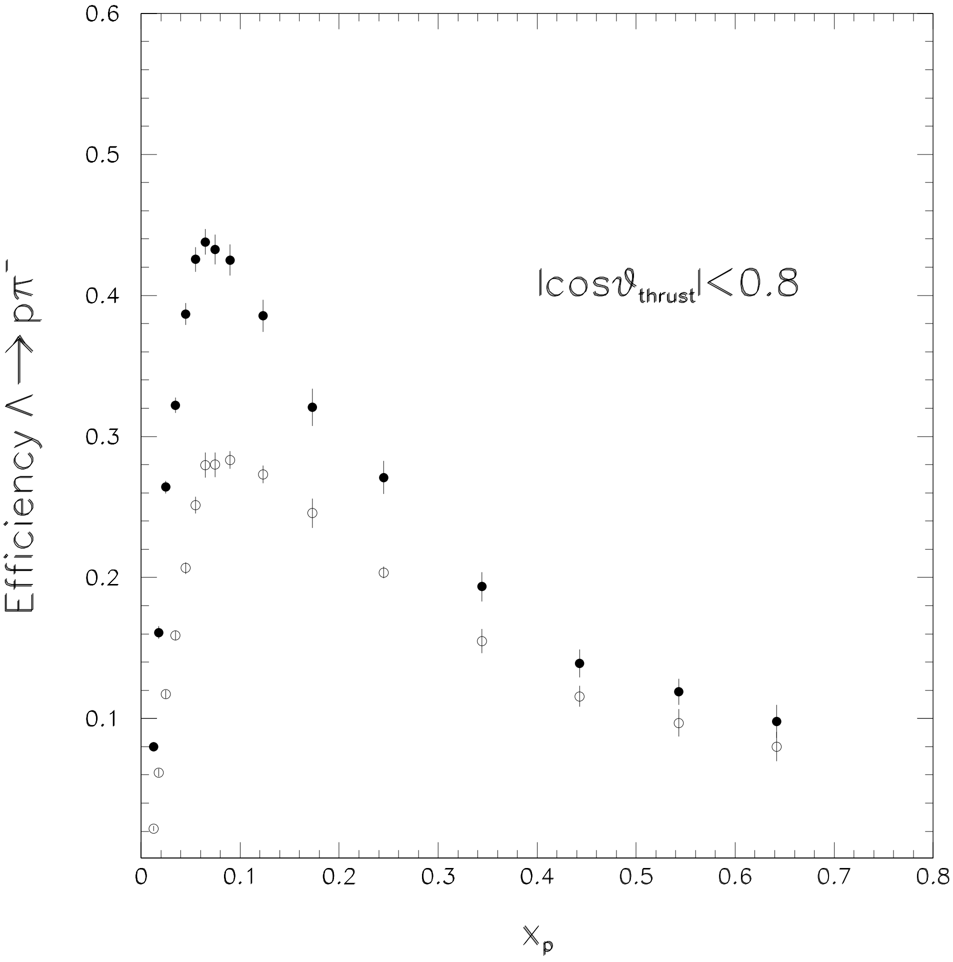

Figure 5.2: The efficiency for reconstructing $\Lambda \rightarrow p\pi^-$ in an event with at least one other Λ candidate in events which satisfy $|\cos\theta_{thrust}| < 0.8$. Shown are the efficiencies with no requirement on the number of z-chamber hits on the tracks (closed points), and with a requirement that there be 4 or more z-chamber hits on both tracks (open points).

- $N_{\Lambda\Lambda} + N_{\overline{\Lambda}\,\overline{\Lambda}}/\text{event} = 0.0236 \pm 0.0008$ (stat) ± 0.0025 (syst).

This can be compared with the previously published rate of 0.0205 ± 0.0039 (stat) ± 0.0028 (syst). The improvement in the statistical error is partly due to a change in the background determination. A fit which had a large statistical uncertainty was used in the publication.

One can also define the probability for a correlated $\overline{\Lambda}$ to follow a tagging Λ in the chain as:

$$P = 2 \times \frac{N_{\Lambda\overline{\Lambda}}}{N_{\Lambda(\overline{\Lambda})}}$$

where $N_{\Lambda\overline{\Lambda}}$ is the efficiency corrected number of pairs and $N_{\Lambda(\overline{\Lambda})}$ is the number of single tagging $\Lambda(\overline{\Lambda})$. The factor of two arises to take care of double counting in the tagging sample. The probabilities are found to be

- $P_{\Lambda\overline{\Lambda}} = 0.338 \pm 0.028$
- $P_{\Lambda\Lambda(\overline{\Lambda}\,\overline{\Lambda})} = 0.130 \pm 0.011$

where the errors are a combination of the statistical and systematic errors. The systematic errors from the Λ measurement enter the equation only once, so that the total systematic error on the probability is 7.6%. One can compare this with the values of 0.354 ± 0.034 and 0.117 ± 0.011 from the OPAL publication [8]. This probability measures how often baryon number and strangeness are compensated together.

In events with at least one reconstructed Ξ^-, one can perform a similar analysis. Tagging on a Ξ^-, such that the $\Lambda\pi^-$ reconstructed mass is within

±15 MeV of the nominal Ξ^- mass, we search for additional $p\pi^-$ combinations (see figure 5.3). In all we find 402 ± 25 $\Xi^-\overline{\Lambda}$ pairs and 125 ± 16 $\Xi^-\Lambda$ pairs. The uncorrelated background is again determined from the same baryon number pairs. The overall excess of correlated $\Xi^-\overline{\Lambda}$ pairs is 277 ± 23, which corresponds to an overall production rate of

- $N_{\Xi^-\overline{\Lambda}}$/event $= 0.0150 \pm 0.0012$ (stat) ± 0.0015 (syst)

As in the case of the $\Lambda\overline{\Lambda}$ pairs, we take the systematic errors from the inclusive Λ and Ξ^- rate determinations as the systematic errors. The rate can be compared with the value from the OPAL publication [8] of 0.0096 ± 0.0019 (stat) ± 0.0013 (syst) per event. The present value is about 1.7 standard deviations higher than the published value based on only the 1990 and 1991 data samples. One can note that the inclusive single Ξ^- rate is similarly higher than the previously published value.

Also in figure 5.3 the invariant mass spectrum for additional $\Lambda\pi^-$ combinations in events with one identified Ξ^- is shown. In this case, we find 15 opposite baryon number pairs and 2 same baryon number pairs, for a total excess of 13 ± 4.1 events. The overall production rate of $\Xi^-\overline{\Xi}^+$ pairs is found to be

- $N_{\Xi^-\overline{\Xi}^+}$/event $= 0.0016 \pm 0.0005$ (stat) ± 0.0002 (syst).

The previously published value from OPAL was 0.00038 ± 0.00067 (stat) ± 0.00007 (syst), which was consistent with zero [8]. The present result is about 1.4 standard deviations higher than the old rate, and also shows positive evidence for $\Xi^-\overline{\Xi}^+$ compensation. In addition, no resonances were found in either the $\Lambda\overline{\Lambda}$ or the $\Lambda\Lambda(\overline{\Lambda}\,\overline{\Lambda})$ mass spectrum (see figure 5.4).

Probabilities of a $\overline{\Lambda}$ or $\overline{\Xi}^+$ following a Ξ^- in the chain can be calculated, yielding the following results:

- $P_{\Xi^-\overline{\Lambda}} = 0.625 \pm 0.070$
- $P_{\Xi^-\overline{\Xi}^+} = 0.133 \pm 0.044$

These values are consistent with the previously published probabilities of 0.463 ± 0.099 and 0.037 ± 0.065, respectively [8], and agree to within 1.4 and 1.2 standard deviations of the published values, respectively. The errors are combinations of the statistical and systematic errors, where the systematic errors have been taken from the inclusive Λ and Ξ^- rate calculations. Again these probabilities have the advantage over pair rates that the systematic error of the tagging sample does not enter into the calculation.

5.2 Rapidity Correlations

The identified baryon pairs are used to measure the strength of rapidity correlations. In order to facilitate comparisons with Monte Carlo, the rapidity distributions are corrected for efficiency and are same baryon number pair background subtracted.

To measure rapidity correlations in opposite baryon number pairs, the Λ is taken as the tagging particle and its rapidity defined such that it is positive. In the case of same baryon number pairs, the tagging particle is

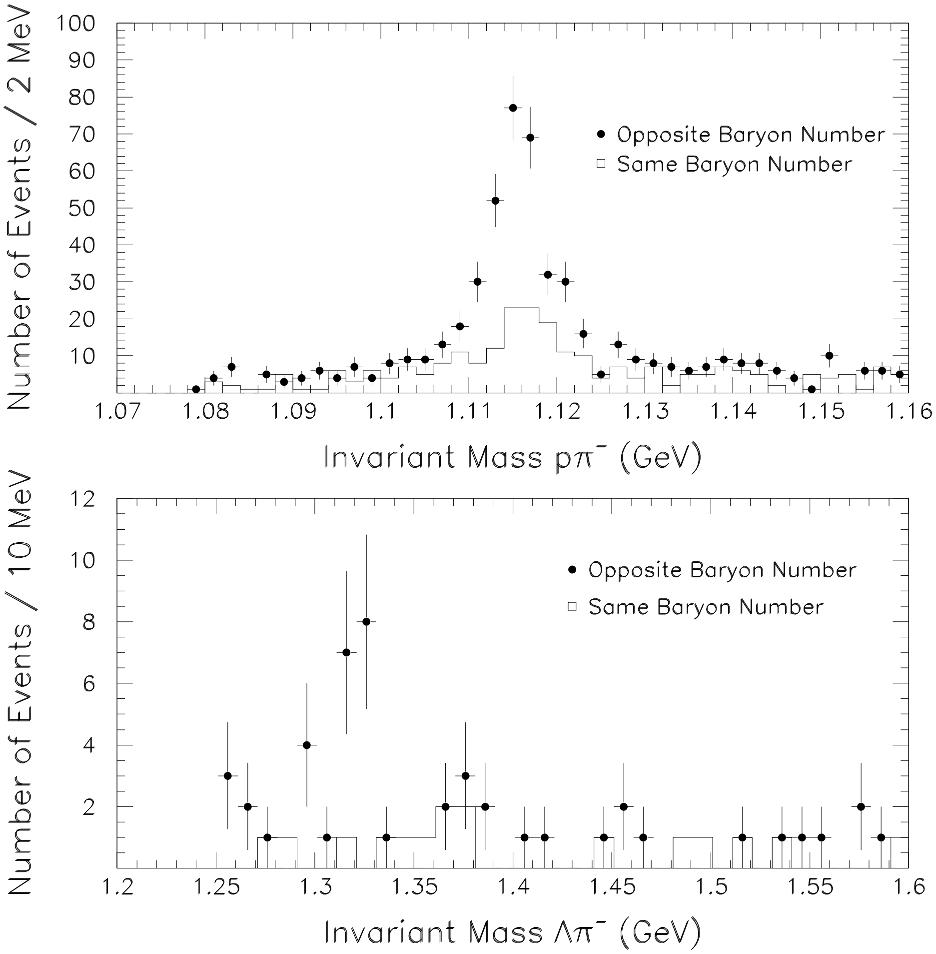

Figure 5.3: The invariant mass distributions $p\pi^-$ and $\Lambda\pi^-$ in events which have a tagged $\Xi(\overline{\Xi}^+)$. The cases for opposite baryon number pairs and same baryon number pairs are plotted.

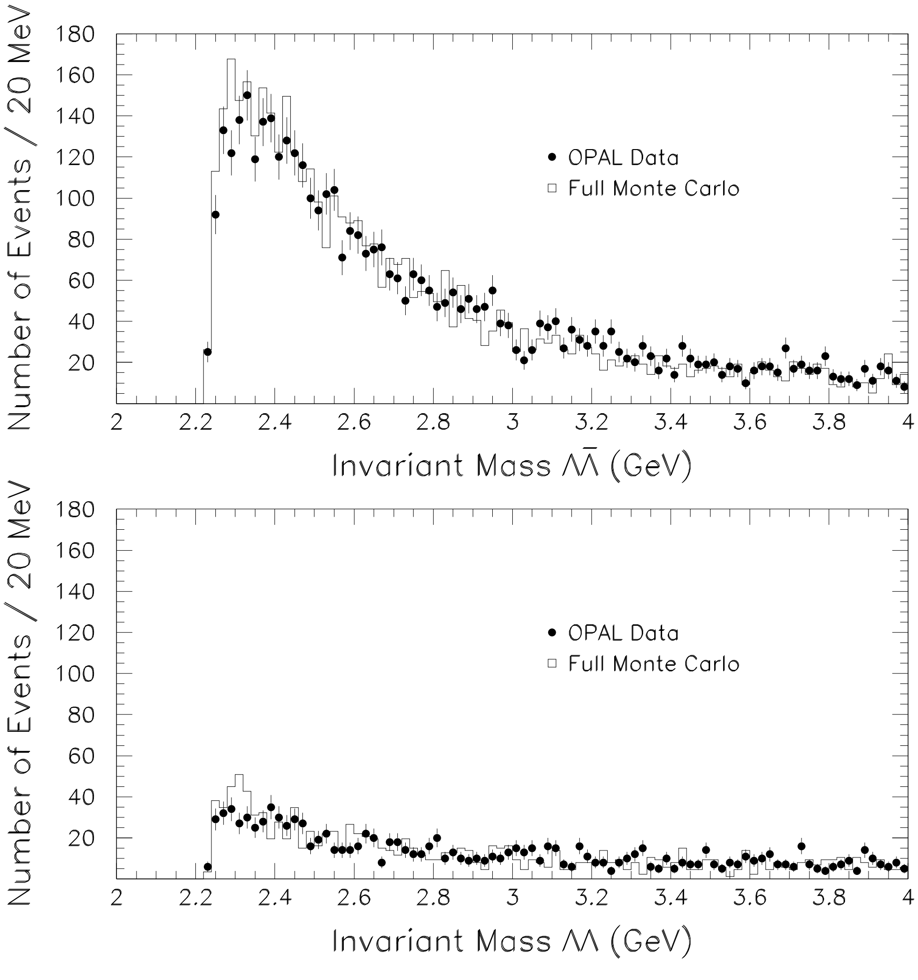

Figure 5.4: The invariant mass of $\Lambda\overline{\Lambda}$ pairs, and the invariant mass of $\Lambda\Lambda$ and $\overline{\Lambda}\,\overline{\Lambda}$ pairs.

chosen randomly. The tagging sample is divided into five subsamples with different rapidity tagging intervals over a range of $0.0 < y_\Lambda < 3.5$. The rapidities of the two baryons in the pair are then shifted such that the rapidity of the tagging particle is centered in the appropriate tagging interval, while the rapidity difference remains unchanged. For the case of opposite baryon number pairs, the same baryon number pair distributions are subtracted.

The efficiency correction is based on the efficiency plot in figure 5.2. Each Λ candidate is weighted according to the efficiency as a function of momentum. The momentum dependent efficiency can be used to correct the rapidity distributions of Λ's, as is shown in figure 5.5. Good agreement is found between the efficiency corrected distributions of the rapidity of all $\Lambda(\overline{\Lambda})$ and the rapidity of $\overline{\Lambda}$ in opposite baryon number pairs at the detector level in the Monte Carlo and the same distributions at the generator level.

The results are plotted in figure 5.6 for the data before correcting for the efficiency and in figure 5.7 after the efficiency weighting has been done. The distribution for same baryon number pairs, including background, are shown in figure 5.8, showing the essentially flat distribution expected from uncorrelated production.

An indication of long-range strangeness compensation is seen in the highest rapidity ranges in figure 5.7. Such compensation is expected if the Λ and $\overline{\Lambda}$ contain or are the daughters of particles which contained the primary quarks of the Z^0 decay.

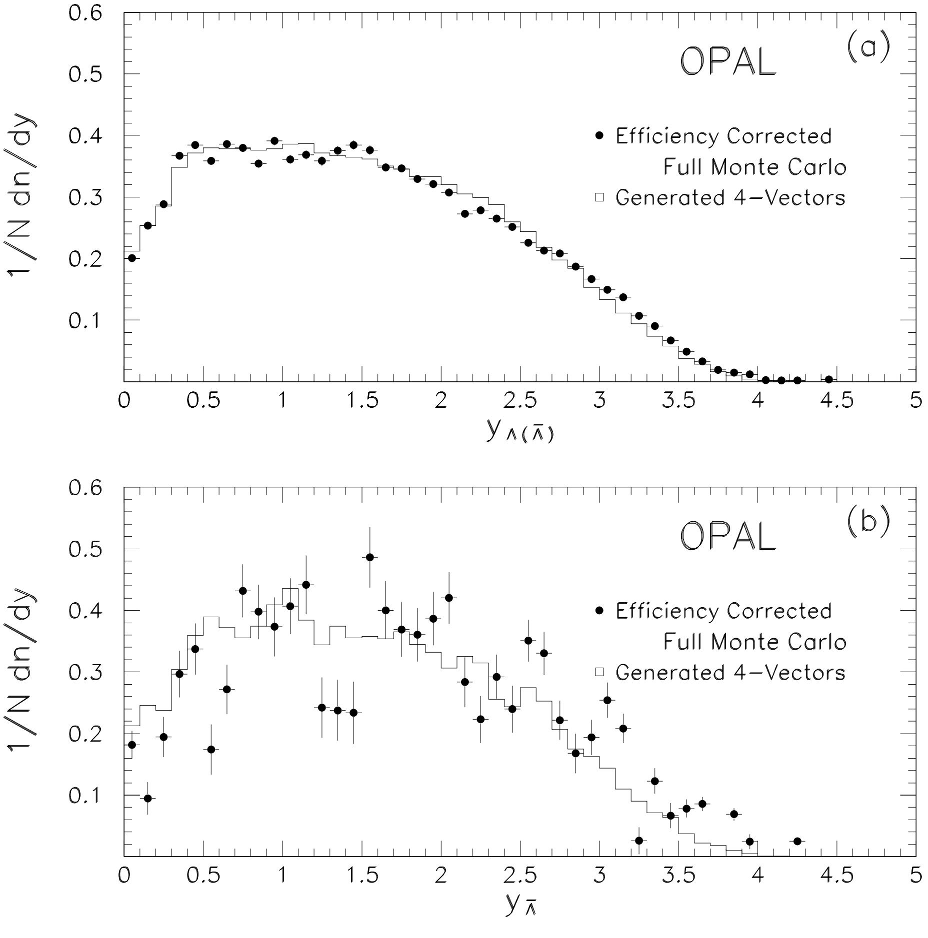

Figure 5.5: (a) Rapidity distribution of single $\Lambda(\overline{\Lambda})$, for efficiency weighted Monte Carlo reconstructed events compared to the rapidity distribution at the generator level. (b) Same distribution as above, but for $\overline{\Lambda}$'s in events which contain a tagging Λ.

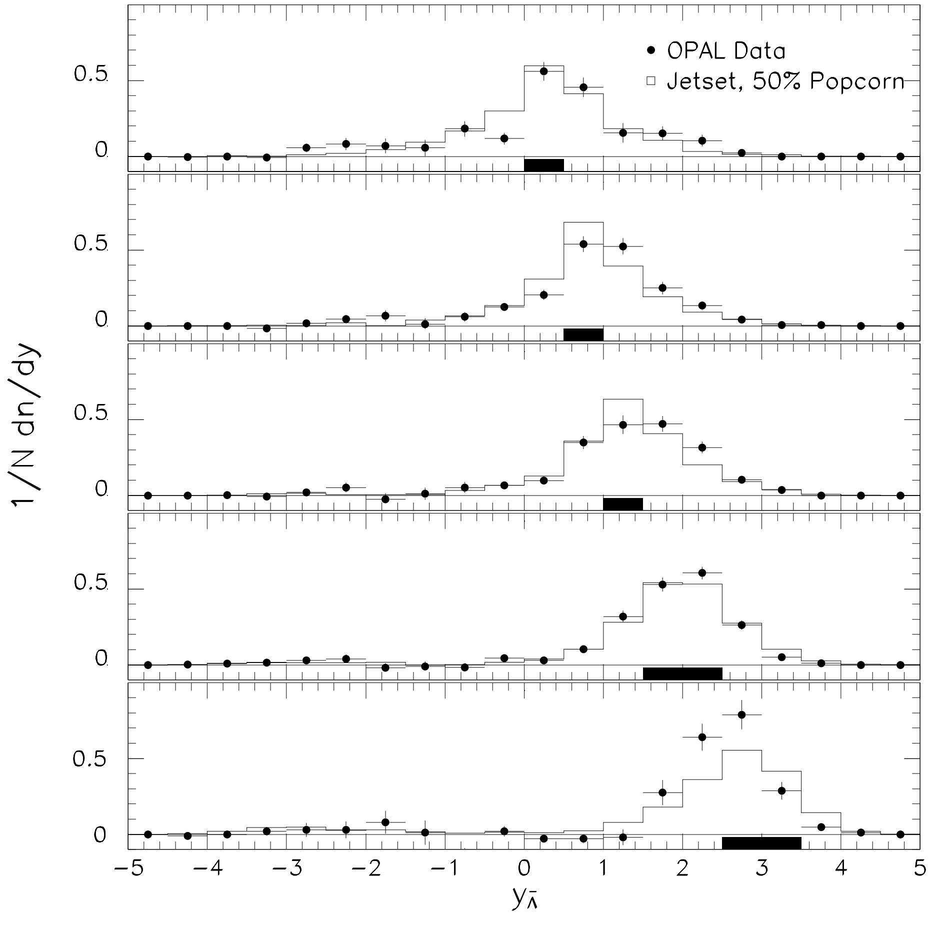

Figure 5.6: Rapidity of $\overline{\Lambda}$ for various tagging intervals of the Λ rapidity, shown as solid boxes, before weighting the data according to the efficiency.

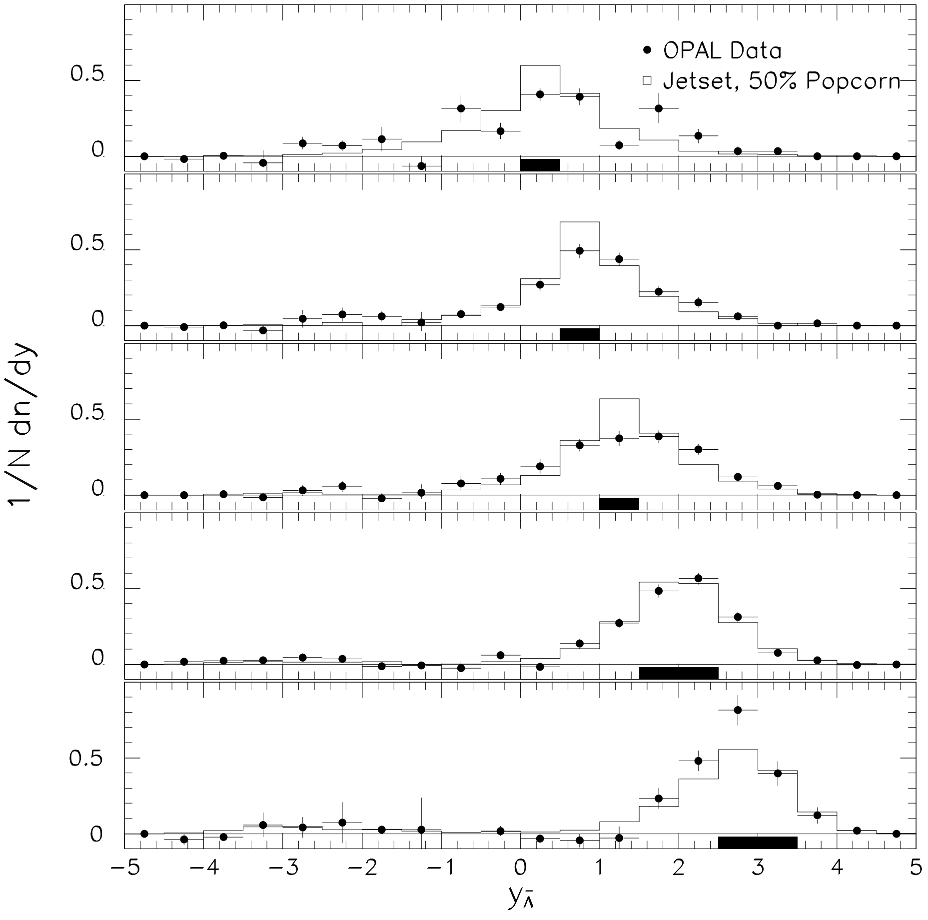

Figure 5.7: Rapidity of $\overline{\Lambda}$ for various tagging intervals of the Λ rapidity, shown as solid boxes, where the data have been weighted according to the efficiency.

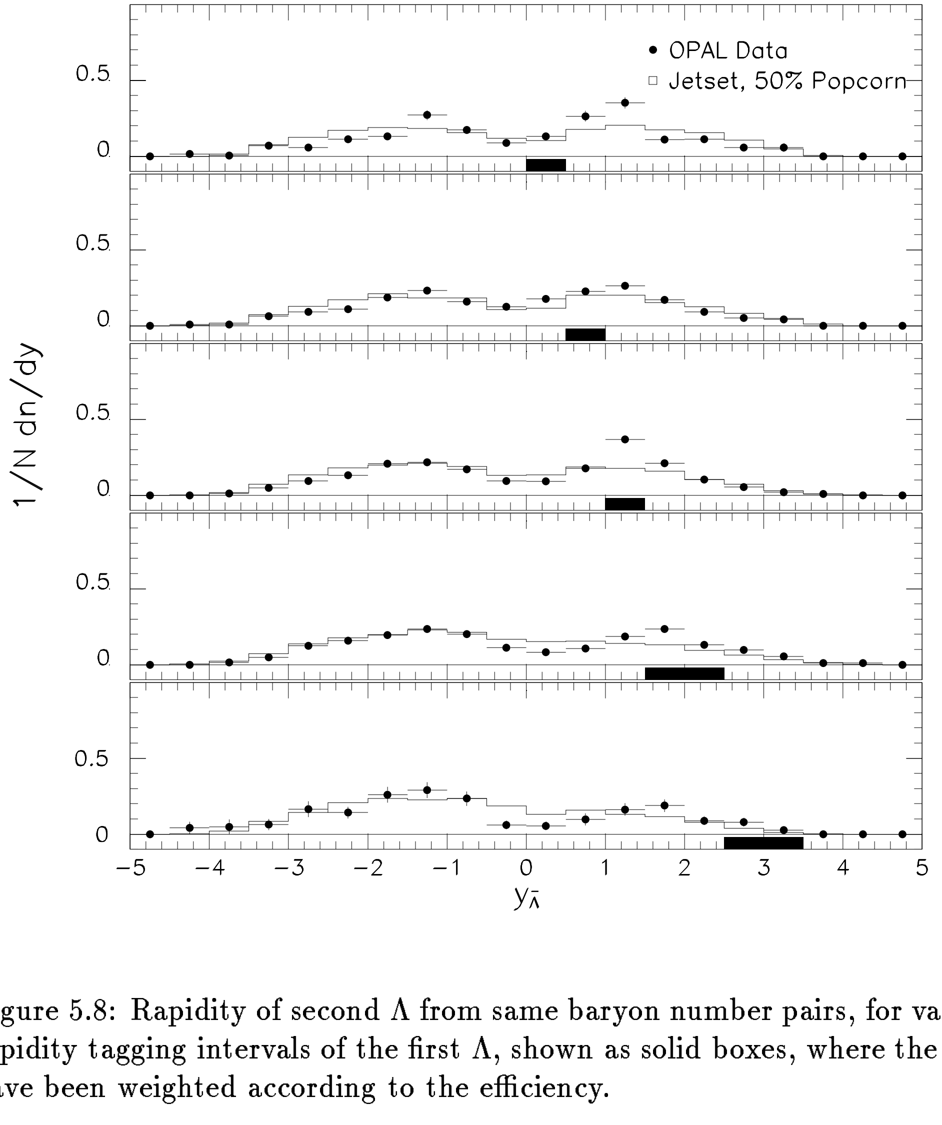

Figure 5.8: Rapidity of second Λ from same baryon number pairs, for various rapidity tagging intervals of the first Λ, shown as solid boxes, where the data have been weighted according to the efficiency.

5.3 Comparison with Monte Carlo Models

Rapidity correlations in baryon pairs can be compared with Monte Carlo models which implement different chains in the production process. In figure 5.9, the rapidity difference of $\Lambda\overline{\Lambda}$ pairs in the data is compared with three different Monte Carlo models. The highest curve is the prediction from HERWIG, in which baryon-antibaryon pairs are produced from the decay of a cluster. This Monte Carlo has too strong rapidity correlations between the Λ and the $\overline{\Lambda}$. The JETSET Monte Carlo with a production chain of baryon-antibaryon (the popcorn probability was set to zero) also shows rapidity correlations which are too strong. Also shown is the UCLA Monte Carlo, in which there are an average of 1.7 popcorn mesons in the chain.

With JETSET we have the possibility to change the popcorn probability. The shape of the rapidity difference distribution is sensitive only to changes in this parameter. As can be seen in figure 5.10, the best agreement with the data is found for popcorn probabilities greater than 80%.

On the other hand, the pair production rates are best described by low values of the popcorn probability (see table 5.1). We have tuned JETSET to the single baryon and meson rates listed in the table, for different values of the popcorn probability. The best overall agreement is found for the UCLA Monte Carlo, if the disagreement with the strength of the rapidity correlations is ignored. The pair rates and the strength of the rapidity correlations cannot be simultaneously described by any of the models.

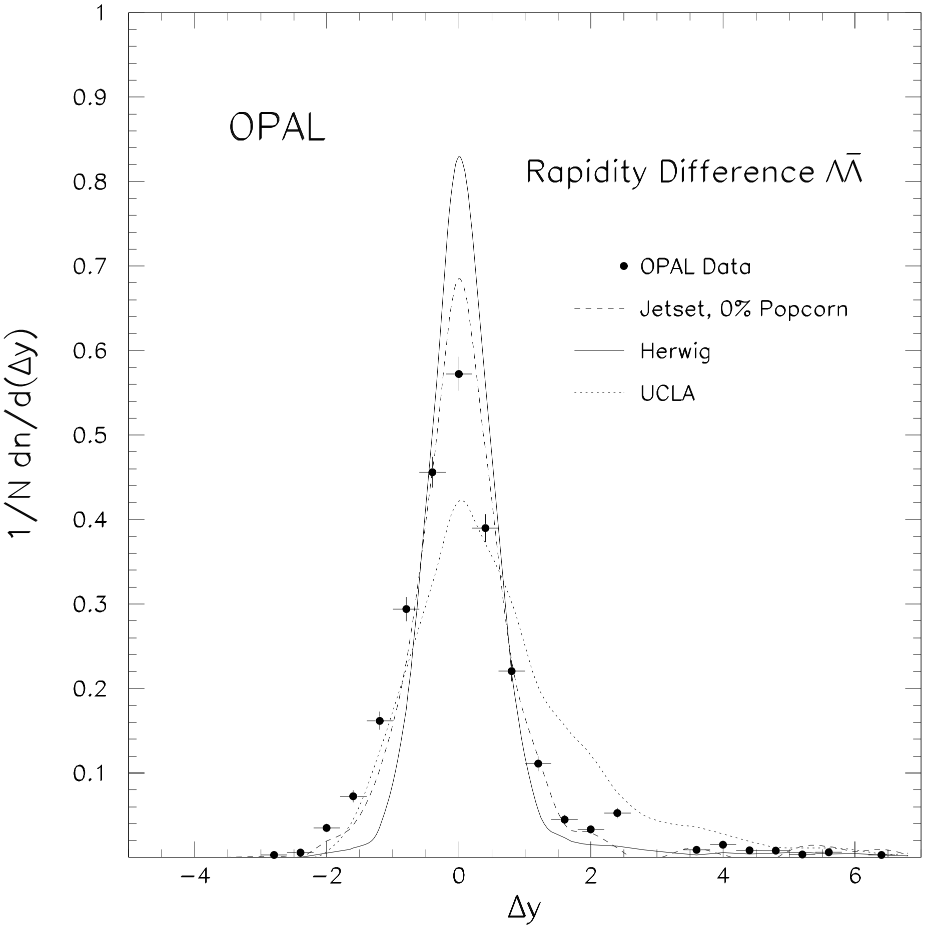

Figure 5.9: The rapidity difference of $\Lambda\bar{\Lambda}$ pairs (background subtracted) in the data (points) compared to several Monte Carlo Models.

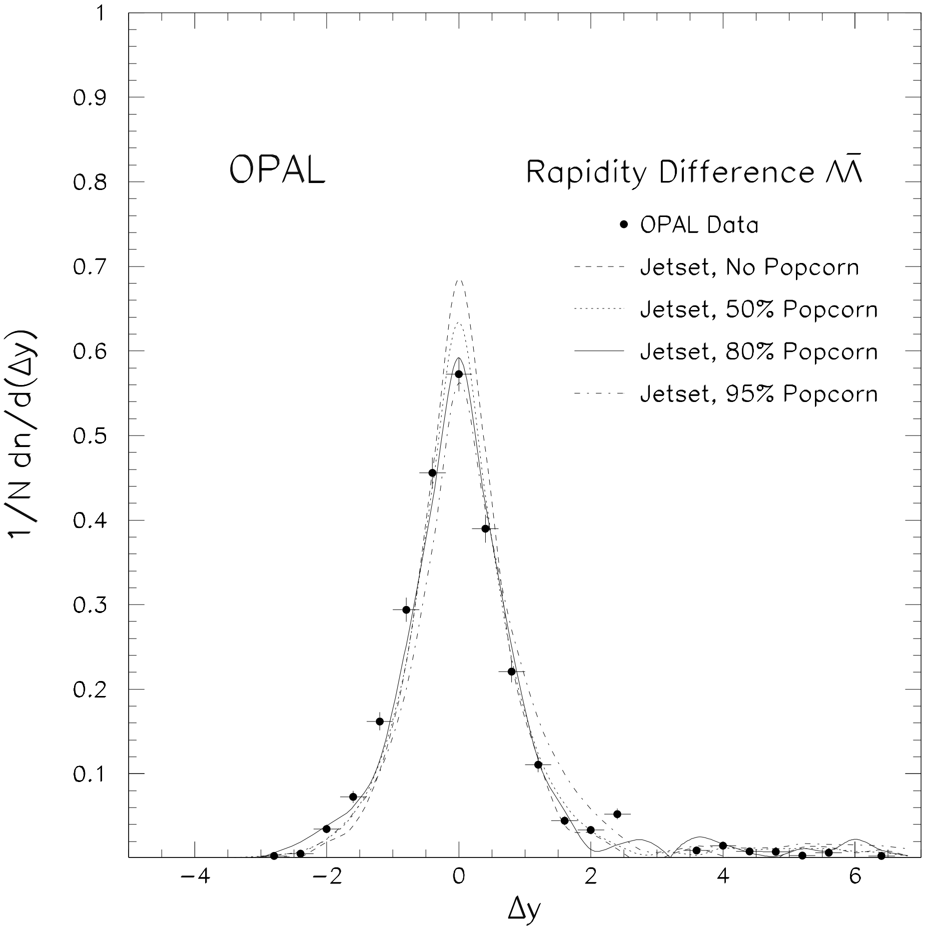

Figure 5.10: The rapidity difference of $\Lambda\overline{\Lambda}$ pairs (background subtracted) in the data (points) compared to several probabilities of popcorn production in JETSET.

		Probability				
Tagging Baryon	Tagged Baryon	OPAL data	JETSET 7.3 no popcorn	JETSET 7.3 95% popcorn	UCLA [55]	HERWIG 5.6 default
Λ	$\overline{\Lambda}$	0.338 ± 0.028	0.311	0.266	0.398	0.552
$\Xi^-(\overline{\Xi}^+)$	$\overline{\Lambda}(\Lambda)$	0.625 ± 0.070	0.618	0.426	0.580	0.701
Ξ^-	$\overline{\Xi}^+$	0.133 ± 0.044	0.204	0.091	0.082	0.152
$\Lambda(\overline{\Lambda})$	$\Lambda(\overline{\Lambda})$	0.130 ± 0.011	0.152	0.138	0.117	0.165
particle		N/event				
p		0.95 ± 0.10	1.08	1.10	1.03	0.83
Λ		0.363 ± 0.023	0.350	0.362	0.330	0.351
Ξ^-		0.0240 ± 0.0022	0.0243	0.0241	0.0229	0.037
$\Sigma(1385)^\pm$		0.0372 ± 0.0031	0.0366	0.0343	0.0756	0.120
$\Xi(1530)^0$		0.0072 ± 0.0014	0.0023	0.0027	0.0088	0.014
Ω^-		0.0033 ± 0.0012	0.0002	0.0003	0.0010	0.004
$\pi^\pm$		17.09 ± 0.44	16.9	17.0	16.7	16.8
K^0		2.10 ± 0.14	2.22	2.14	2.02	2.20
$K^*(892)^0$		0.76 ± 0.09	0.75	0.74	0.73	0.88
$\phi(1020)$		0.086 ± 0.018	0.145	0.137	0.125	0.135

Table 5.1: Probabilities to find an additional Λ or Ξ^- in events which already contain a Λ or a Ξ^-. The inclusive particle (and antiparticle) yields are also given. The errors are the combined statistical and systematic errors.

Chapter 6

A Measurement of the $\Lambda(\overline{\Lambda})$ Forward-Backward Asymmetry

Since the Standard Model [1] has both vector and axial vector electroweak couplings, there is an interference which produces an asymmetry in the differential cross section as a function of $\cos\theta$ of the interaction $e^+e^- \rightarrow Z^0 \rightarrow f\overline{f}$. In the Born approximation, the differential cross section is given by

$$\frac{dn}{d\cos\theta} \sim \left(1 + \cos^2\theta + \frac{8}{3}A_{FB}\cos\theta\right),$$

where θ is the angle between the incoming electron and the outgoing fermion [64].

The forward-backward asymmetry of the primary quarks in Z^0 decays is a function of the flavor of the quark, according to the Standard Model. For charge -1/3 quarks, the asymmetry is predicted to be about 9% at $\sqrt{s} = m_Z$. and for charge +2/3 quarks, the asymmetry is predicted to be about 6%.

As can be seen in figure 6.1, the number of Λ which contain the primary quarks or are decay products of hadrons which contained the primary quarks increases with rapidity (or alternatively the momentum). The number of primary strange quarks is the largest share, although significant heavy flavor contributions are present. One can try to see whether the assumption that the $\Lambda(\overline{\Lambda})$ will have the asymmetry of the primary quarks holds up in the data.

The asymmetry is measured by fitting the distribution of $\Lambda(\overline{\Lambda})$ candidates to a second order polynomial. The major sources of background are the decays $\mathrm{K}^0_\mathrm{S} \rightarrow \pi^+\pi^-$ and the random combinatorial background, both of which have been found in the Monte Carlo to be symmetric to within the Monte Carlo statistical error. We must therefore correct the asymmetry measured from the fit by a factor $(N_\Lambda + N_{\mathrm{backg.}})/N_\Lambda$.

We must also take into account any acceptance effects which bias the asymmetry measurement. The largest of these effects are

- loss of efficiency at the edge of the acceptance in $\cos\theta$, and
- the dependence of the maximum decay length on $\cos\theta$.

The first effect is important at all momentum ranges, and the second effect becomes important even at relatively low momentum $x_p > 0.2$. Since the maximum allowed radius for Λ decays is $R_{max} = 130$ cm, the maximum allowed decay length in the barrel will go as

$$l_{max} = \frac{R_{max}}{\sqrt{1-\cos^2\theta}}.$$

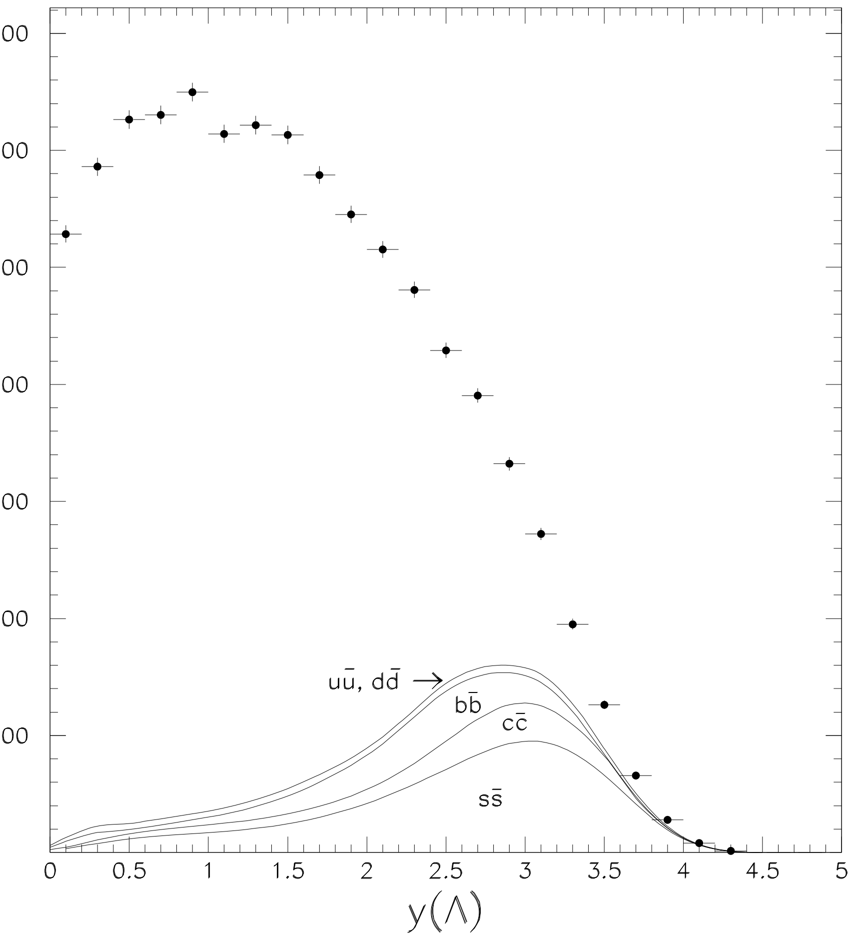

Figure 6.1: The number of Monte Carlo $\Lambda(\overline{\Lambda})$ which contain the primary quarks, as a function of the rapidity, from a sample of 250,000 JETSET events.

This θ dependence will introduce a detector bias when the decay lengths are typically long, in other words when $\gamma c\tau$ is on the order of R_{max}. Both of these effects were studied with full detector simulation JETSET events.

The fits to the $\cos\theta$ distributions of $\Lambda(\overline{\Lambda})$ are shown in figure 6.2. Reliable fits can be made up to $x_p = 0.5$. As can be seen in figure 6.3, the asymmetry for low momentum $\Lambda(\overline{\Lambda})$ is consistent with zero, since these mostly originate in the fragmentation. For higher momentum $\Lambda(\overline{\Lambda})$, however, the asymmetry is large and approaches the value one expects from the Standard Model, about 8%, for $\Lambda(\overline{\Lambda})$ which come mostly from strange quark events. These results are summarized in table 6.1 and figure 6.3. The dashed curve in the plot is the prediction from JETSET. A similar study in OPAL using a different method gets results which are consistent with these results [65].

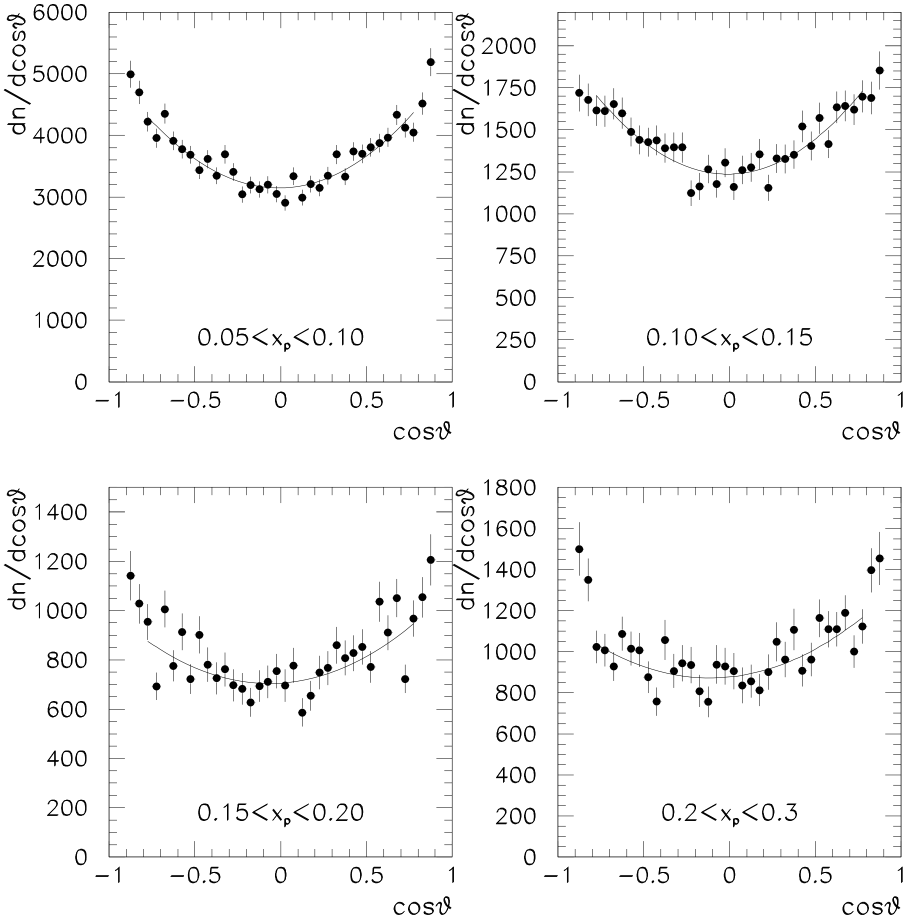

Figure 6.2: The distributions for $\cos\theta_\Lambda$ for various ranges of x_p, corrected for detector effects and efficiency.

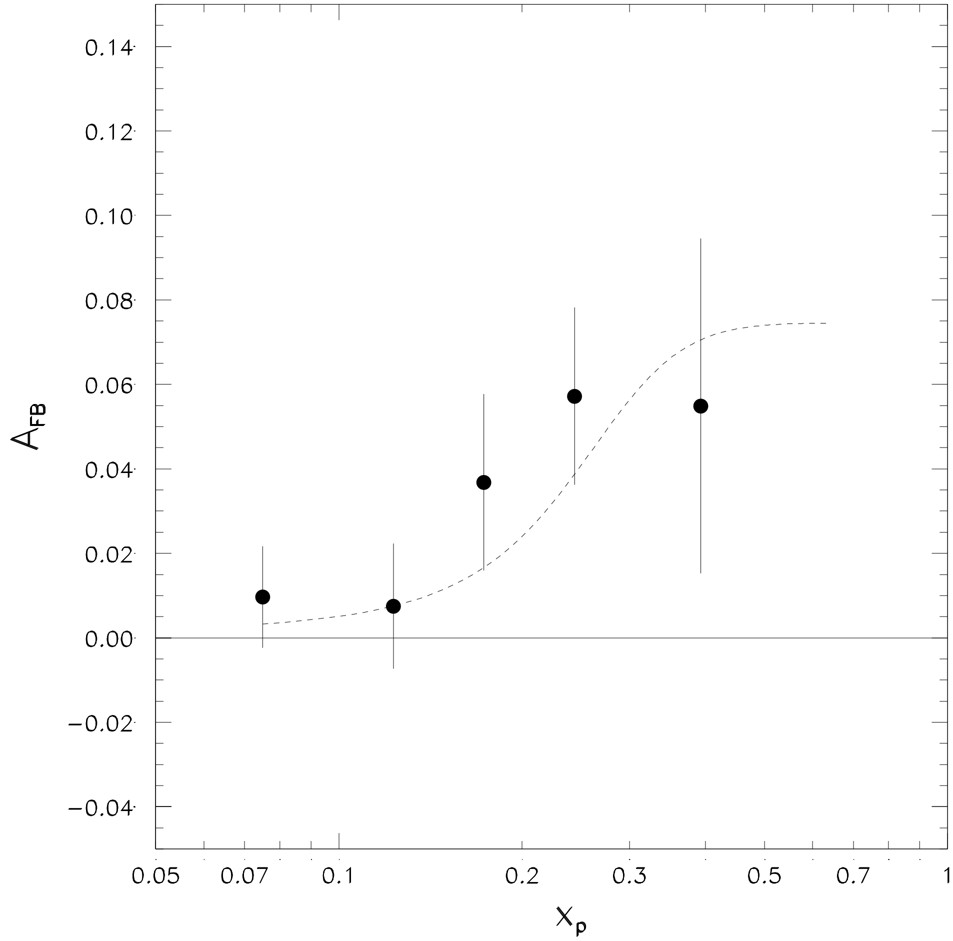

Figure 6.3: The measured forward-backward asymmetry A_{FB} as a function of momentum. The dashed curve is the prediction from the JETSET Monte Carlo.

x_p	N_Λ	$N_{backg.}$	A_{FB}
0.05-0.10	25503	13873	.0096 ± .0120
0.10-0.15	13453	3786	.0075 ± .0148
0.15-0.20	6515	2047	.0368 ± .0209
0.20-0.30	5399	1843	.0572 ± .0210
0.30-0.50	2415	973	.0549 ± .0397

Table 6.1: The measured forward-backward asymmetry A_{FB} as a function of momentum.

Chapter 7

Summary and Conclusions

In the beginning of this thesis, several questions were posed about the nature of baryon production and hadron production in general. Strong rapidity correlations have been found between baryon-antibaryon pairs, one of the consequences of chain-like particle creation with local conservation of quantum numbers. Simultaneous baryon number and strangeness compensation was also seen by measuring the rates of $\Lambda\overline{\Lambda}$, $\Xi^-\overline{\Lambda}$, and $\Xi^-\overline{\Xi}^+$ pairs.

An indication of long-range rapidity correlations was found, which is a consequence of the assumption that high momentum particles contain or are the daughters of particles which contained the primary quarks of a jet. Using the measurement of the forward backward asymmetry of $\Lambda(\overline{\Lambda})$ baryons, it may be possible in the future to determine the forward-backward asymmetry of the decay of the $Z^0 \rightarrow s\bar{s}$.

As for the determination of baryon flavor content and spin, comparisons with cluster fragmentation and diquark models show that there are still many inconsistencies with the measured strange baryon rates, especially in the baryon decuplet. Although JETSET is good at describing the inclusive octet baryon rates, only one of the decuplet rates could be described by a suitable tuning of the parameters. The measured cross sections for Λ and Ξ^- are found to be too hard in JETSET. A formula based on isospin invariance showed good agreement with most of the observed inclusive baryon production rates at $\sqrt{s} = 10$ GeV, $29 - 34$ GeV, and 91 GeV.

Bibliography

[1] S.L. Glashow, J. Iliopoulos, and L. Maiani, Phys. Rev. **D2** (1970) 1285;
S. Weinberg, Phys. Rev. Lett. **19** (1967) 1264;
A. Salam, *Elementary Particle Theory,* ed. N. Svartholm (Almquist and Wiksells, Stockholm, 1969) pp. 367.

[2] H. Fritzsch, M. Gell-Mann, and H. Leutwyler, Phys. Lett. **B47** (1973) 365.

[3] MARK I Collab., G. Hanson *et al.,* Phys. Rev. Lett. **35** (1977) 1609.

[4] D.H. Saxon *et al., Baryon Production in* e^+e^- *Annihilation,* RAL-88-102 (1988).

[5] P Mättig, Phys. Rep. **177** (1989) 141.

[6] See for example:
ARGUS Collab., H. Albrecht *et al.,* Z. Phys. **C9** (1988) 177.
CELLO Collab., H.-J. Behrend *et al.,* Z. Phys. **C46** (1990) 397.
CLEO Collab., S. Behrends *et al.,* Phys. Rev. **D31** (1985) 2161.
HRS Collab., M. Derrick *et al.,* Phys. Rev. **D35** (1987) 2639.
HRS Collab., T.L. Geld *et al.,* Phys. Rev. **D45** (1992) 3949.

JADE Collab., W. Bartel *et al.,* Phys. Lett. **B104** (1981) 325.

MARK II Collab., S.R. Klein *et al.,* Phys. Rev. Lett. **58** (1987) 644.

TASSO Collab., R. Brandelik *et al.,* Phys. Lett. **B103** (1981) 75.

TASSO Collab., M. Althoff *et al.,* Z. Phys. **C27** (1985) 27.

TASSO Collab., W. Braunschweig *et al.,* Z. Phys. **C45** (1989) 209.

TPC Collab., H. Aihara *et al.,* Phys. Rev. Lett. **54** (1985) 274.

[7] OPAL Collab., P.D. Acton *et. al.,* Phys. Lett. **B291** (1992) 503.

[8] OPAL Collab., P.D. Acton *et al.,* Phys. Lett. **B305** (1993) 415.

[9] DELPHI Collab., P. Abreu *et al.,* Phys. Lett. **B275** (1992) 231.

[10] CDF Collab., F. Abe *et al.,* Phys. Rev. Lett. **68** (1992) 367.

[11] The LEP Collabs., ALEPH, DELPHI, L3, and OPAL, Phys. Lett. **B276** (1992) 247.

[12] UA1 Collab., Arinson, G. *et al.,* Phys. Lett. **126B** 398.

UA2 Collab., Banner, M. *et al.,* Phys. Lett. **122B** 476.

[13] ALEPH Collab., D. Buskulic *et al.,* CERN-PPE/93-110 (5 July 1993), Sub. to Phys. Lett. B.

[14] See for example:

JADE Collab., W. Bartel *et al.,* Phys. Lett. **B91** (1980) 142.

MARK-J Collab., D.P. Barber *et al.,* Phys. Rev. Lett. **43** (1979) 830.

PLUTO Collab., C. Berger *et al.,* Phys. Lett. **B86** (1979) 418.

TASSO Collab., R. Brandelik *et al.,* Phys. Lett. **B86** (1979) 243.

[15] Particle Data Group, K. Hikasa *et al., Review of Particle Properties,* Phys. Rev. **D45** (1992).

[16] M. Gell-Mann, *Proceedings of the International Conference on High Energy Physics, Geneva, 1962,* (CERN Scientific Information Service, Geneva,1962), p. 805;
R. Behrends, J. Dreitlein, C. Fronsdal, and W. Lee, Rev. Mod. Phys. **34** (1962) 1;
S.L. Glashow and J.J. Sakurai, Nuovo Cimento **25** (1962) 337.

[17] V. Barnes *et al.,* Phys. Rev. Lett. **12** (1964) 204.

[18] M. Gell-Mann, Phys. Lett. **8** (1964) 214.

[19] G. Zweig CERN-TH.8419/412 (1964).

[20] See for example:
Particle Data Group, K. Hikasa *et al., Review of Particle Properties,* Phys. Rev. **D45** (1992), III.80.

[21] See for example:
T. Sjöstrand *et al.,* in: *Z Physics at LEP 1,* Vol. 3, CERN Report CERN/89-08, eds. G. Altarelli, R. Kleiss, and G. Verzegrassi (CERN, Geneva, 1989).

[22] B. Andersson *et al.,* Phys. Rep. **97** (1983)31;
T. Sjöstrand, Comp. Phys. Comm. **39** (1986) 347 and CERN-TH.6488/92;
T. Sjöstrand and M. Bengtsson, Comp. Phys. Comm. **43** (1987) 367.

[23] G. Marchesini *et al.,* Comp. Phys. Comm. **67** (1992) 465.

[24] R.D. Field and R.P. Feynman, Nucl. Phys. **B136** (1978) 1.

[25] B. Andersson, G. Gustafson, G. Ingleman, and T. Sjöstrand, Phys. Rep. **97** (1983) 33.

[26] JADE Collab., W. Bartell *et al.,* Phys. Lett. **B101** (1981) 129.

[27] B. Andersson, G. Gustafson, and T. Sjöstrand, Physica Scripta **32** (1985) 574.

[28] S.B. Chun and C.D. Buchanan, UCLA-HEP-92-008 (August 1992).

[29] S. Wolfram, in: Proc. 15th Rencontre de Modiond (March 1980), ed. J. Tran Thanh Van; Caltech preprint CALT-68-778 (April 1980).

[30] *LEP Design Report,* Vol. 2, CERN-LEP/TH/84-01 (June 1984).

[31] *LEP Design Report,* Vol. 1, CERN-LEP/TH/83-29 (June 1983).

[32] OPAL Collab., M. Ahmet *et al.,* Nucl. Instrum. and Meth. **A305** (1992) 275.

[33] O. Biebel *et al.,* Nucl. Instrum. and Meth. **A323** (1992) 169.

[34] OPAL Collab., M.Z. Akrawy *et al.,* Phys. Lett. **B240** (1990) 497.

[35] M. Arignon *et al.,* Nucl. Instr. and Meth. **A333** (1993) 330.

[36] M. Arignon *et al.,* Nucl. Instr. and Meth. **A313** (1992) 103.

[37] J.T.M. Bains *et al.,* Nucl. Instrum. and Meth. **A325** (1992) 271.

[38] D.G. Charlton *et al.,* Nucl. Instrum. and Meth. **A325** (1992) 129.

[39] J. Allison *et al.,* Nucl. Instrum. and Meth. **A317** (1992) 47.

[40] R. Brun, *et al., GEANT3 User's Guide,* CERN-DD/EE/84-1.

[41] OPAL Collab., G. Alexander *et al.,* Z. Phys. **C52** (1991) 175.

[42] N. Tesch, M. Hauschild, and R.-D. Heuer, *Measurement of the Production Rates of Charged Hadrons in* e^+e^- *Annihilation at the* Z^0, OPAL internal physics note # 110 (23 July 1993).

[43] OPAL Collab., P.D. Acton *et al.,* Zeit. Phys. **C53** (1992) 539.

[44] TASSO Collab., W. Braunschweig *et. al.,* Z. Phys. **C45** (1989) 209-222.
MARK II Collab., S.R. Klein *et. al.,* Phys. Rev. Lett. **58** (1987) 644.
HRS Collab., S. Abachi *et. al.,* Phys. Rev. Lett. **58** (1987) 2627.

[45] Torbjörn Sjöstrand, CERN-TH.6488/92 (May 1992, revised September 1992).

[46] OPAL Collab., G. Alexander *et. al.,* Phys. Lett. **B264** (1991) 219.

[47] J. Schwienning, Internal OPAL talk (September 1993).

[48] L3 Collab., B. Adeva et al., Phys. Lett. **B259** (1991) 199.

[49] See for example:
ARGUS Collab., H. Albrecht *et al.,* Phys. Lett. **B247** (1990) 121.
ACCMOR Collab., S. Barlag *et al.,* Phys. Lett. **B236** (1990) 495.

CLEO Collab., M.S. Alam *et al.,* Phys. Lett. **B226** (1989) 401.

CLEO Collab., P. Avery *et al.,* Phys. Rev. Lett. **62** (1989) 863.

[50] ACCMOR Collab., S. Barlag *et al.,* Phys. Lett. **B236** (1990) 495.

[51] OPAL Collab., P.D. Acton *et al.,* Phys. Lett. **B281** (1992) 394.

[52] OPAL Collab., P.D. Acton *et al.,* Phys. Lett. **B305** (1993) 407.

[53] OPAL Collab., M.Z. Akrawy *et al.,* Zeit. Phys. **C47** (1990) 505.

[54] OPAL Collab., G. Alexander *et al.,* Phys. Lett. B264 (1991) 467-475.

[55] S.B. Chun and C.D. Buchanan, UCLA-HEP-92-008 (August 1992). The results quoted here were obtained from the authors. They used the parameters η = 2.5, a = 1.9, and b = 1.10. Further details can be found in the above reference.

[56] R. Hagedorn, Nuovo Cim. **56** (1968) 1027.

[57] W. Ochs, Z. Phys. **C15** (1982) 227.

[58] ARGUS Collab., H. Albrecht *et al.,* Phys. Lett. **B230** (1989) 169.

[59] ARGUS Collab., H. Albrecht *et al.,* Z. Phys. **C39** (1988) 177.

[60] ALEPH Collab., D. Buskulic *et al.,* Phys. Lett. **B292** (1992) 210.

[61] DELPHI Collab., P. Abreu *et al.,* Phys. Lett. **B298** (1993) 236.

[62] G. Lafferty, Internal OPAL talk (September 1993).

[63] See for example:

JADE Collab., W. Bartel *et al.,* Phys. Lett. **B104** (1981) 325;

TASSO Collab., M. Althoff *et al.,* Z. Phys. **C17** (1983) 5;

TASSO Collab., M. Althoff *et al.,* Z. Phys. **C27** (1985) 27;

TASSO Collab., M. Althoff *et al.,* Phys. Lett. **B139** (1984) 126;

TPC Collab., H. Aihara *et al.,* Phys. Rev. Lett. **53** (1984) 2199;

TPC Collab., H. Aihara *et al.,* Phys. Rev. Lett. **54** (1985) 274;

TPC Collab., H. Aihara *et al.,* Phys. Rev. Lett. **55** (1985) 1047;

MARK2 Collab., C. de la Vaissiere *et al.,* Phys. Rev. Lett. **54** (1985) 2071;

HRS Collab., M. Derrick *et al.,* Phys. Rev. **D35** (1987) 2639.

[64] Z. Kunszt, P. Nason, *et al.,* in: *Z Physics at LEP 1,* Vol. 1, CERN Report CERN/89-08, eds. G. Altarelli, R. Kleiss, and G. Verzegrassi (CERN, Geneva, 1989).

[65] D. VanDenPlas and F. Lamarche, *A Measurement of the Forward-Backward Asymmetry and Longitudinal Polarization of High Momentum Lambdas in Z^0 Decays,* OPAL internal physics note # 112 (17 August 1993).